Doctoral Dissertation
Doctoral Program in Chemical Engineering (34^{th} cycle)

Advances in two and three-phase bubble columns modeling: large eddy simulation and population balance

Francesco Maniscalco

* * * * * *

Supervisors
Prof. Marco Vanni, Supervisor
Prof. Antonio Buffo, Co-supervisor

Doctoral Examination Committee:
Prof. Renzo Di Felice, Referee, Università di Genova
Prof. Cristian Marchioli, Referee, Università di Udine
Dr. Francesco Bertola, SABIC, Maastricht
Prof. Alberto Passalacqua, Iowa State University
Prof. Luigi Manna, Politecnico di Torino

Politecnico di Torino
April 2022

I hereby declare that, the contents and organization of this dissertation constitute my own original work and does not compromise in any way the rights of third parties, including those relating to the security of personal data.

Francesco Maniscalco
Turin, April, 2022

Summary

Bubble column reactors play a pivotal role in chemical engineering processes and plants, thanks to the well-known performance in mixing, heat and mass transfer and the simple operating mechanisms. However, despite this wide diffusion and well-established usage, the computational model of bubble columns is still challenging. The main reason is the complexity of the two- or, if solid particles are dispersed in the liquid medium, three-phase flows at industrial operating conditions, which are characterized by a deep reciprocal dependence of the phases behavior. In this perspective, several aspects, such as the accounting for phase inversion, the individual role of interfacial forces or the choice of the turbulence framework, are still nowadays among the most debated issues that require to be unambiguously addressed. Additionally, when the gaseous phase is injected at high velocity in the systems, the obtained bubbles dispersion is polydisperse with a wide distribution in the bubble size, affecting the main design parameters such as the gas hold up or the mass transfer coefficient. Moreover, the impact of solid particles in slurry bubble columns on these parameters is still ambiguous, and the corresponding computational model is even more difficult.
The latest research efforts have been focusing on tackling these issues but, however, every approach still strongly depends on the particular system which is considered, thus failing to extend the proposed solutions to a wider range of set-ups and conditions. This doctoral dissertation shares the efforts of the latest scientific production aiming to address the aforementioned issues but, on the other hand, aspires to individuate and develop one model with the widest applicability range. With this purpose, four different experimental set-ups were simulated, in order to strengthen the validity of the proposed model.
Firstly, it was urged the need for a fine modeling of phase interaction and phase inversion. This is fundamental to perform stable and fast simulations grounded on a physical phenomenon rather than on numerical artifices. To this purpose, the phase blending approach is described, including the tuning performed to identify the optimal parameters. It was then shown that, in the framework of a RANS description of the turbulence, which is, traditionally, the most popular for the modeling of bubble columns, this implementation leads to stabler and faster simulations without losses in results accuracy.

In parallel, the RANS turbulence description was also adopted to model a gas-liquid-solid bubble column with a square section. Slurry columns are particularly relevant in petrochemical processes since the solid particles in the liquid medium work as catalysts. The aim of this part of the work was the assessment of the role of the solid particles in hydrodynamics, phase interaction and bubbles coalescence and breakage. In this case, the inclusion of secondary interfacial forces was necessary to maintain the stability and accuracy of the simulations, probably due to the square geometry of the column. Under this basis, the model successfully predicted the behavior of the flow following the addition of solid particles, which resulted in a lower gas hold-up and a larger mean bubble size due to the promoted coalescence induced by the solid particles, in line with experimental observations.
Secondarily, the phase blending model was implemented together with a LES turbulence description. This was a novelty compared to the latest scientific research, that, in the context of the modeling of bubble columns, mainly applied LES to simplified geometries and operating conditions. In this work, different systems at high gas velocity were simulated and, in particular, the condition of asymmetrical gas injection was investigated in detail. An analysis of the various models for the calculation of the subgrid turbulent eddy viscosity was then performed, suggesting that the classical Smagorinsky model, coupled with the inclusion of the bubble induced turbulence effects, could be the most reliable model for describing bubbly flows at these conditions. Afterwards, the impact of the lift force was assessed. Results showed that its inclusion in the set of interfacial forces does not contribute to an improvement of the results, and, in the asymmetrical injection conditions, it even produces significant miscalculation in the prediction of the flow.
A population balance modeling is then implemented in the LES turbulence framework to estimate the bubble size distribution: to the best of our knowledge, coupled LES-PBM models have not been applied so far to the simulation of bubble columns. Results confirm once more the considerable potential of the LES approach for the modeling of bubble columns: the estimated bubble size distribution matches thoroughly the experimental measurements. Coupled LES-PBM simulations were performed to compute the oxygen mass transfer coefficient in a square bubble column where pure and contaminated water was used as liquid phases: in particular, the latter consists in water - Sodium Dodecyl Sulfate solutions with different concentrations of the contaminants. Once more, the model successfully predicted both the flow patterns and the mass transfer coefficient in all the tested conditions, confirming the experimental measurements and, specifically, it was reported an increase in the mass transfer coefficient with the addition of the contaminant to the liquid phase. Additionally, the adoption of the LES turbulence framework allowed to solve the issues originated from the square geometry and reported in the RANS simulations of the slurry column without any additional modeling assumptions.

Contents

List of Tables

List of Figures

Chapter 1

Introduction

It would not be an overstatement to claim that, nowadays, most part of the chemical and process industry rests on multiphase flows.
Bubble column reactors are widely used in the industrial chemical engineering landscape, ranging in a broad variety of applications where they may be considered as the main core of the whole process such as waste treatment [1, 2], biological processes [3], production of fuels (i.e. Fischer-Tropsch) [4], synthesis of methanol [5], alkylation, hydroformylation and other organic processes .
The reason of this well-established diffusion is the optimal performance of bubble columns in the mass, heat and momentum exchange without the presence of moving mechanical parts: it is promoted by the bubbles themselves in their rise through the liquid.

1.1 Hydrodynamics of bubble columns

The gas is usually injected from the bottom of the column through a sparger that facilitates the formation of the bubbles inside the liquid phase and, eventually, leaves the equipment from the top. The liquid phase could either flow co- or countercurrently with respect to the gas phase or be batched in the system. The sparger design is fundamental for the performance of the whole reactor: its features, like orifice size and shape, are crucial for the formation of bubbles, and they have considerable impact on the fluid dynamics of the systems, especially in the lower part, close to the gas injection [6].
As the bubbles flow up, the volume of the gas-liquid system increases with respect to the volume initially occupied by the pure liquid due to the presence of the gas itself. This change of volume is called global gas hold-up:

$$\Phi = 1 - \frac{H_0}{H_f}, \tag{1.1}$$

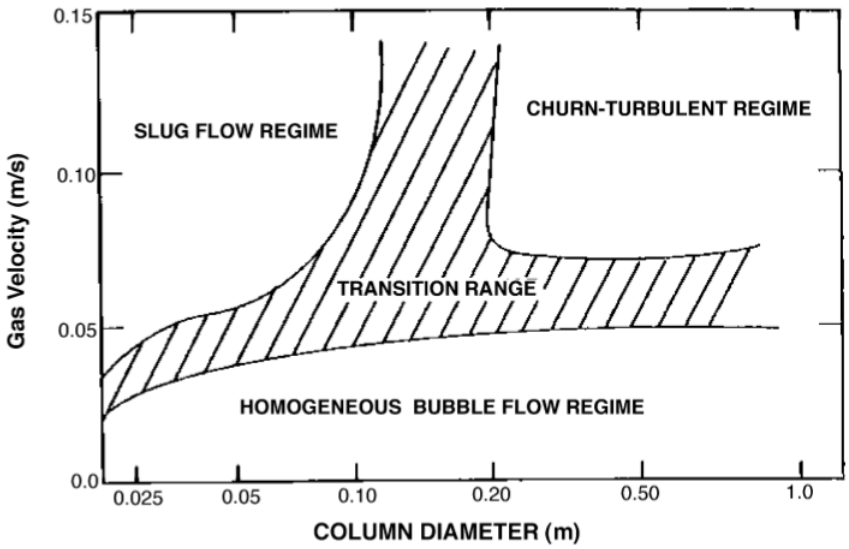

Figure 1.1: Hydrodynamical regimes map, extracted from [3].

where H_0 is the initial liquid height and H_f the height reached by the gas liquid dispersion after the initial transient behavior.
The global gas hold-up has historically been the key feature for the industrial design of the bubble column, being simple to measure experimentally and proportional to the interfacial area of the dispersion. However, the actual conditions may differ locally, since the presence of gas may be higher or lower in certain areas of the column. Therefore, the usage of the global gas-hold up has become insufficient to describe the behavior and performance of a bubble column. This is true especially when the gas is injected at high velocity: on this regard, a first distinction of the hydrodynamical regimes occurring in the system can be made according to the gas superficial velocity [7], which is the velocity of the gas phase as if it occupies the whole cross section. Two main regimes can be identified (Fig. 1.1) and they are sketched in Fig. 1.2:

- *homogeneous regime.* It is characterized by bubbles monodispersity and low mixing; the liquid recirculation patterns are negligible;
- *heterogeneous regime.* It occurs when the gas velocity is high and, therefore, the bubbles size is strongly dependent on the position. The gradients of volume fraction and velocity in a radial section are sharp, with a peak at the center of the column. In this case the liquid recirculation is remarkable since it goes upward at the center of the column and downward at the wall, providing the best condition for mixing and heat transfer.

These two regimes are divided by an often called *transitional regime*, with mixed features. Moreover, the relation between the gas hold-up and the gas velocity is

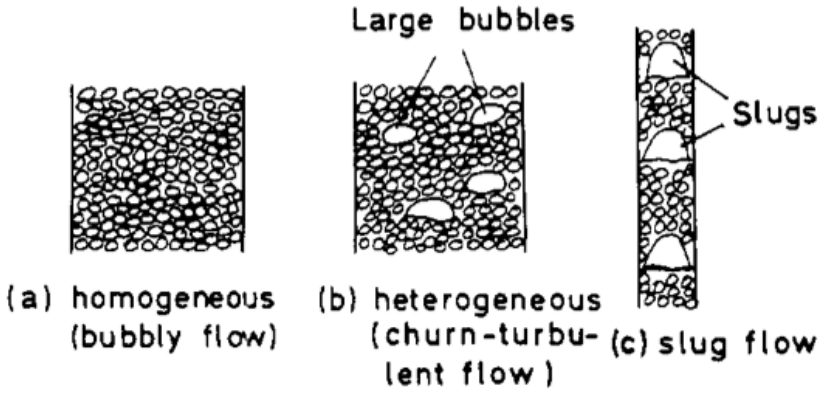

Figure 1.2: Hydrodynamical regimes in bubble columns, extracted from [7].

approximately linear, with different slope in the homo- and heterogeneous regimes; the transitional regime is then identified as the velocity (or the velocities range) where the slope of this linear relations changes.
However this distinction is not strict: if the column diameter is small and the gas velocity is high, the formation of large bubbles occupying the whole cross section is observed (Fig. 1.2), which hinder the rise of small bubbles; this regime goes by the name of slug flow regime. Some authors have identified other regimes which are subjected to particular features: Besagni et al. [8], for instance, distinguished the *pseudo-homogeneous regime*: it occurs at low gas superficial velocity but, unlike the pure homogeneity, it is characterized by a wide bubble size distribution due to characteristics of the sparger.
Moreover, in most of the industrial applications and, in particular, in organic processes, the chemical reactions involved in the bubble columns need to be catalyzed. In this case, the liquid phase contains a dispersion of solid catalytic particles and the whole systems is referred to as slurry bubble column [3, 4, 9]. The impact of the solid particles on the overall fluid dynamics is considerable and it has not been fully understood yet, since it depends on their physicochemical properties and size distribution. Nevertheless, it is commonly recognized that the solid particles promote bubble coalescence, eventually leading to a lower gas hold-up and interfacial area.
On this basis, the modeling of bubble columns and slurry bubble columns has been always challenging given the complexity of the fluid dynamics and the interaction between the two or three phases. The purpose of this doctoral thesis is to improve and facilitate the computational description and simulation of bubble columns on several fronts and to achieve a model with the widest range of applicability. In particular, a special focus is given on the simulations of systems operating at realistic

industrial conditions, which may often differ from the laboratory scale conditions.

1.2 State of the art

In the latest years the scientific community has been focusing on several aspects of the modeling of bubble columns: in the following, a brief survey of the most relevant works is provided. In particular, this section principally describes the most recent trends on Eulerian-Eulerian modeling (Section 2.2), being the framework within this study is developed.
As thoroughly discussed in Section 2.2.3, one of the greatest concerns in the computational modeling of bubble columns is the relative importance of each interfacial force in the interphase momentum exchange term (Eq. (2.4)) [10, 11]. The drag force is universally recognized as the predominant term among the interfacial forces and it is always accounted for. The majority of the models used for the description of cylindrical bubble columns only considers the drag force as interfacial momentum exchange mechanism, thus excluding lift, virtual mass, wall lubrication and turbulence dispersion forces [12–15]. In particular, this is the case for systems with uniform gas injection, where the transverse forces are less significant compared to the drag force. If the gas velocity is high enough to overcome the homogeneous regime, the drag coefficient may be corrected by the so-called swarm factor [16], with the aim of taking into account the relative proximity of the gas bubbles, whose boundary layers interact each other.
Nevertheless, there is a significant number of studies that combine the drag force with one or more additional interfacial forces simultaneously. The inclusion of the lift force is perhaps the most debated point in this field: some studies suggest that it should be evaluated, especially in those systems where the gas is not injected uniformly [17–19]; significant results were obtained with uniform gas feed as well, even if at extremely low gas velocity [20]. However, even when included, largely shared consensus on the value of lift coefficient is yet to be achieved. Most of the studies including the lift force adopts a fixed coefficient [19, 21–24] even though it was largely shown that the lift coefficient varies locally in the bubble column [25], being a function of the bubble size. In this light, several correlations were developed to estimate the dependency of the lift coefficient on the bubbles dimensions and shapes, and they are often coupled to a population balance approach to properly capture the bubble size distribution and, therefore, correctly estimate the lift force [26, 27].
Fewer studies included the turbulent dispersion force [27–30]; however, the value of the turbulent dispersion coefficient varies widely from 0.1 to 0.6, and a rigorous method for its choice that goes beyond the fitting to experimental data has not been proposed yet. The same consideration may be applied to the virtual mass force, whose coefficient is often arbitrarily set to 0.5 [10]. Furthermore, it was reported

that its incorporation does not lead to a noteworthy improvement of the quality of the results and slows down the convergence of the simulation [11, 31, 32]. Finally, the wall lubrication force is rarely considered given the negligible impact on the flow pattern, especially in large bubble columns [33, 34].
Therefore, it can be stated that a general agreement on the validity of the interfacial forces has not been reached yet, and the recent literature lacks of an universal approach with a broad applicability.
Turbulence modeling is another crucial aspect in the computational description and it is scrupulously examined in Section 2.4. Traditionally, the Reynolds Averaged Navier Stokes (RANS) approach is the most popular for the simulation of bubble columns and, in general, two-equations models have been preferred thanks to the positive compromise between results quality and computational demand [13–16, 24, 29, 35–41]; among these, the RNG k-ϵ model showed the best performances [15, 16]. On the other hand, a continuously growing interest has aroused on the Large Eddy Simulation (LES) approach for the modeling of bubble columns [18, 23, 28, 30, 42], thanks to the enhanced prediction ability of the flow patterns. However, this method has been mainly applied to simplified systems, highlighting the lack in the scientific production of the application of LES to configurations of industrial interest.
One more aspect at the center of the scientific interest is the contribution to the turbulence of the liquid phase generated by the motion of the bubbles, namely the Bubble Induced Turbulence (BIT) (Section 2.4.3). Once more, the effective inclusion of the BIT effects in the computational model depends on the choice of the authors [43, 44] and a precise and clear criterion to evaluate its suitability to the simulated system is still missing.
Moreover, it should be noted that the simulation of bubbly flows at high concentration of gas is complex regardless of the turbulence modeling, since the gas-in-liquid dispersion is on the edge of phase inversion. To the best of our knowledge, in the literature this issue has not been tackled as it would have deserved, also given its huge impact on the quality of the results and the stability of the simulation [45].
One of the major drawbacks of the Eulerian-Eulerian modeling consists in the determination of the bubble size, which must be fixed to a constant value. Although the hypothesis of a constant bubble diameter might be suitable at low gas velocity, when the system is monodisperse, it does not correspond to the reality at high gas velocity, when the hydrodynamics falls into the heterogeneous regime and the bubble size changes largely as function of the position following bubbles coalescence and breakage. A popular solution to this issue is the coupling of the CFD simulation to a Population Balance Model (PBM) to track and estimate the evolution of the bubble size distribution [46], as discussed in Section 2.5. Hence, coupled CFD-PBM simulations have become progressively a common strategy to simulate bubble columns. However, in the prevalent strategy PBM equations are usually coupled to RANS models of the turbulence for dilute bubbly flows [13, 14, 47–52], when,

indeed, their contribute is not of great relevance given the monodispersity of the flow; only very recently CFD-PBM models have been applied in the heterogeneous regime [41].
On the other hand, there are very few studies that combine LES turbulence description to PBM equations in turbulent dispersed flows, and they are mainly related to the simulations of the behavior of droplets in turbulent jet flows [53, 54]. To the best of our knowledge, a combined LES-PBM approach for the simulation of bubble columns has not been proposed yet, neither at low nor high gas velocity.
As aforementioned, the liquid phase is often characterized by the presence of solid particles that, in the chemical processes, serve as catalysts for the reactions occurring in the systems. The modeling of such cases becomes even more problematic, since the addition of a third phase further complicates the phase interactions [9]: a more detailed overview of the modeling of slurry bubble columns is provided in Section 3.2. Moreover, it has still not been completely clarified the impact of the solid particles on gas hold-up and bubble coalescence, since the behavior may change according to the particles hydrophilicity [4]. The majority of the studies showed a decrease of the gas hold-up which is likely caused by the enhancement of the coalescence promoted by solid microparticles [55–57]. Contrarily, it was reported that larger solid particles boost the bubbles collision and breakage, leading to smaller bubbles and larger gas hold-up [58]. Therefore, it should be pointed out that the results obtained in the recent studies are not universally valid and they may be different according to the particles' surface characteristics, size and volume fraction [9].
If PBM equations are applied to the modeling of slurry bubble columns, the role of the solid particles in bubbles interactions must be accounted for to correctly estimate the bubbles size distribution. The scientific literature lacks of an universal approach to address this point and the technique to include the effect of solid particles in PBM equations varies according to the specific modeling strategy of the solid phase: the presence of solid particles may be taken into account by a new combination of coalescence and breakage kernels [59], modifying the drag force [60] or introducing solid-dependent corrections in the PBM kernels [56].
To conclude, this work should be put along the lines of the latest scientific research and aims to develop a broad and comprehensive approach for the modeling of bubble columns, overcoming the aforementioned issues.

1.3 Structure of the work

After this introductory chapter, a detailed description of the basis of the two-fluid modeling framework is provided in in Chapter 2, with a special focus on the implementation of the interfacial forces, the blending models, the turbulence description and the population balance model. The interfacial forces are crucial in modeling

bubble columns and, despite the huge research efforts on their investigation, a wide agreement of their individual relevance has not been reached yet. Following, phase blending models are analyzed, which are frequently overlooked in the modeling of bubble columns but they are pivotal in this study. The analysis of turbulence models focuses on Reynolds-Averaged Navier-Stokes and Large Eddy Simulation models, despite the latter has been applied only in systems which are quite different from the industrial conditions. Finally, the population balance approach is presented as a powerful tool for the estimation of the bubble size distribution, which pure two-fluid models cannot perform.
Chapter 3 briefly describes additional insights on the modeling of bubbles columns, i.e. the slurry bubble columns, extremely common in the industrial organic chemistry, and the modeling of the mass transfer, whose knowledge is essential to estimate the performance of the reactor, especially when it was specifically designed to perform physical or chemical absorption, stripping or a catalyzed reaction.
Chapter 4 reviews the experimental and computational set-ups used for the model validation.
Chapter 5 describes the advantages of the blending approach in simulating two-phase flows at high gas velocity using the classical RANS turbulence models. The implementation of this approach allows to halve the computational time, reduce the experimental-based parameters without affecting the quality of the results.
Chapter 6 details the simulation of a slurry bubble column through the pseudo-homogeneous slurry phase models, thus proving its validity to describe systems where the solid particles are finely dispersed in the liquid phase. The population balance modeling is then coupled to the simulations, in order to estimate the bubble size distribution.
Chapter 7 applies the LES turbulence models, together with the blending approach, to two different experimental set-ups operating at high gas velocity. In particular, it describes the capability of the LES approach, that has been used so far only at low gas velocity, to well describe the heterogeneous regime as well. Moreover, a population balance model is applied to the LES simulation of a bubble column, with excellent results in term of mean diameter prediction.
Chapter 8 further confirms the good performance of LES-PBM coupling by the simulation of partially contaminated systems and the prediction the mass transfer coefficient.
Finally, Chapter 9 draws the main conclusions of this study collecting the specific outcomes of the previous chapters and incorporating them in the light of the principal aim of this doctoral dissertation: the overcoming of the well-known issues resulting from *ad hoc* modeling and the development of a widely applicable model. In this perspective, few suggestions for the future scientific research are pointed out as well.

Chapter 2

Fundamental modeling

In this chapter the fundamental bases of theoretical modeling of dispersed bubbly flows are analyzed, with particular emphasis on the models that will be later adopted in this work.
In particular, after a brief introduction, Section 2.2 goes through the main framework of the models of dispersed systems, which basically differ in the description of the dispersed fluid particles; a special focus is given to the two-fluid Eulerian framework, where the gas phase is treated as a continuous medium, as for the liquid phase. A short analysis of the forces exchanged by the bubbles and the liquid is then provided.
In Section 2.3 the blending models are discussed, which are functional to the local individuation of the continuous and dispersed phase and to account for the phase inversion phenomenon.
Section 2.4 analyzes the main choices for modeling turbulence in bubble columns, focusing on Reynolds Averaged Navier-Stokes (RANS) and Large Eddy Simulation (LES) models.
Finally in section 2.5 the fundamentals of the population balance modeling (PBM) are described, which is an helpful tool to overcome the strongest limitation of the Eulerian models, the setting of a constant bubble diameter. The PBM allows to estimate the bubble size distribution accounting for bubbles breakage and coalescence phenomena, whose rate expressions are briefly discussed, together with the solving algorithm.

2.1 Introduction

In the framework of chemical engineering, process modeling has always been a crucial point. The first and basic approach in modeling an industrial chemical piece of equipment may be twofold:

- assuming that in the system the mixing operation is performed perfectly and,

consequentially, all the process variables such as concentration or temperature are constant throughout the reactor. This is the fundamental hypothesis of Continuously Stirred Tank Reactors (or CSTR) and it is often used as first approach to the modeling of sizable systems where the mixing is well-performed through impellers;

- if the system extends mainly through one coordinate, such as pipes, it can be assumed that the process variables vary only through this coordinate through a plug flow condition. These systems are referred to as Plug Flow Reactors (PFR).

However, these simplifications are frequently too optimistic for modeling actual industrial operations. Therefore they may be improved considering, for instance, bypass portion in CSTR and radial or axial dispersion phenomena in PFR. While being an improvement, those adjustments are still not satisfactory when approaching the modeling of complex systems such as multiphase flows and, among those, bubble columns. In such cases, the system is too complex to be described with the aforementioned techniques and, in order to obtain a reliable model of the system, it is necessary to solve the fundamental conservation equations throughout the domain to assess the fluid dynamics [61].

2.2 Modeling framework

The modeling of disperse multiphase systems has traditionally followed two main paths, according to the treatment of the dispersed phase: Eulerian-Lagragian and Eulerian-Eulerian.

2.2.1 Eulerian-Lagrangian method

In this approach, the continuous medium is modeled as a single continuous phase, hence solving the mass, momentum and (if relevant) energy transport equations, while the dispersed fluid particles are treated in a Lagrangian framework: a Newton equation of motion is solved for each particle and its motion is then tracked. Clearly, this approach requires the knowledge of the forces acting on the fluid particles which, as explained in the following sections, it is still subject of debate. Given the huge computational demand involved in tracking large numbers of bubbles and the difficulties arising from bubbles crowding, typical at high gas velocity , this approach is more common in smaller systems working with low gas hold-up [62–65]. To circumvent the problem, the tracked entities are sometimes considered as parcels of particles. This approach, however, runs into difficulties when the system is polydisperse. Therefore, this method cannot be applied for the purpose of this study.

2.2.2 Eulerian-Eulerian method

The Eulerian-Eulerian framework is the most used and common model to describe bubble columns, from low [66] to medium-high [16,67] gas hold-up. As a general approach, the continuous and dispersed phases are both modeled as interpenetrating continuous media.
As a matter of fact, three different approaches in the framework of the Eulerian-Eulerian model have been developed for describing bubble columns: the mixture model, the Volume of Fluid (VOF) model and the multi-fluid model. In the mixture model the gas and liquid phases are described as a single pseudo-phase, called the mixture phase, with intermediate properties of the two phases and thus solving only one transport equation for the momentum [68–70]. VOF is an interface tracking method and it is mainly used when the knowledge of the specific behavior at the bubbles interface is desired [55, 71–73].
On the other hand, the multi-fluid, or, if only two phases are present, two-fluid model is undeniably the most used approach for the modeling of bubble columns [61]: under the assumption that the pressure is shared by the phases, the continuity and Navier-Stokes equations are solved for each phase, considering the amount of occupied space quantified by the volume fraction α_i. Considering N phases:

$$\alpha_i = \frac{V_i}{\sum_j^N V_j}, \tag{2.1}$$

therefore

$$\sum_i^N \alpha_i = 1. \tag{2.2}$$

For the i-th phase we have the following mass and momentum balances:

$$\frac{\partial}{\partial t}\left(\alpha_i \rho_i\right) + \nabla\left(\alpha_i \rho_i \boldsymbol{u}_i\right) = \sum_{j\neq i}^{N}\left(\dot{m}_{ij} - \dot{m}_{ji}\right) \tag{2.3}$$

$$\frac{\partial}{\partial t}\left(\rho_i \alpha_i \boldsymbol{u}_i\right) + \nabla\cdot\left(\rho_i \alpha_i \boldsymbol{u}_i \boldsymbol{u}_i\right) = -\alpha_i \nabla p + \rho_i \alpha_i \boldsymbol{g} + \nabla\cdot\left(\alpha_i \boldsymbol{\sigma}_i\right) + \sum_{j\neq i}^{N} \dot{m}_{ij}\boldsymbol{u}_{ij} + \sum_{j\neq i}^{N} \boldsymbol{F}_{ij}, \tag{2.4}$$

where $\dot{m}_{ij}$ and $\boldsymbol{F}_{ij}$ are respectively the net mass and momentum flux per unit volume from phase j to phase i, while $\boldsymbol{u}_{ij} = \boldsymbol{u}_i$ if $\dot{m}_{ij} > 0$ and, hence, the mass transfers from phase i to j; on the contrary, $\boldsymbol{u}_{ij} = \boldsymbol{u}_j$ if $\dot{m}_{ij} < 0$. The term $\boldsymbol{\sigma}_i$ is the stress tensor for the phase i:

$$\boldsymbol{\sigma}_i = \mu_i\left(\nabla \boldsymbol{u}_i + \left(\nabla \boldsymbol{u}_i\right)^T - \left(\frac{2}{3}\nabla\cdot\boldsymbol{u}_i\right)\boldsymbol{I}\right). \tag{2.5}$$

A common assumption in the fluid dynamics modeling of bubbly flows is to neglect the interphase mass transfer mechanisms therefore $\dot{m}_{ij} = 0$. Moreover, if only

the gas and the liquid phases are present, $N = 2$ and the phase indicator i and j can be substituted by g and l, denoting respectively the gas and liquid phase. Furthermore, as aforementioned, slurry bubble columns are extremely common in chemical engineering industrial applications and, in this case, the presence of the solid particles must be accounted for as well. For this purpose, refer to Section 3.2 for a detailed description of the modeling of slurry bubble columns.
The term $\boldsymbol{F}_{ij}$ (for the sake of simplicity, in the following it will be denoted simply as $\boldsymbol{F}$, being the phases only two) represents the summation of all the interphase forces per unit volume acting between the gas and the liquid phases which are described in the following section.

2.2.3 Interfacial forces

One of the most debated issues in the modeling of bubble columns following the two-fluid framework is the identification of the interfacial forces exerted to the gas bubbles by the surrounding liquid and *viceversa*. Despite there exists an universal agreement about the identification of these forces, the same can not be stated for their actual relevance under real industrial conditions [10, 74].

Drag force

The drag force originates from the relative motion of the bubble with respect to the surrounding liquid (Fig. 2.1). On the average, it has opposite direction compared to the buoyancy force and therefore, opposing to the latter, it has a significant impact on the hold-up of the gas. The drag force arises from two different contributions: one due to the shape of the fluid particle (form drag) related to its cross sectional area and the other to the friction generated at the bubble-liquid interface (viscous drag), related to the bubble relative velocity [75]. Assuming that the bubbles have spherical shape and hence the projected cross sectional area is equal to the circular area with diameter d_b, the drag force per unit volume $\boldsymbol{F}_D$ can be expressed as:

$$\boldsymbol{F}_{\mathrm{D}} = \frac{3}{4} C_{\mathrm{D}} \frac{\alpha_g \rho_l}{d_b} (\boldsymbol{u}_l - \boldsymbol{u}_g) |\boldsymbol{u}_l - \boldsymbol{u}_g|. \tag{2.6}$$

where d_b is the bubble diameter and C_D is the drag coefficient. The latter depends on both the liquid and gaseous properties and, in particular, on the bubble Reynolds number:

$$Re_b = \frac{d_b \rho_l |\boldsymbol{u}_l - \boldsymbol{u}_g|}{\mu_l}. \tag{2.7}$$

As as example, in Stokesian flow ($Re_b << 1$) the relation between the drag coefficient for an isolated solid particle, C_D^{∞} and Re_b was proven to be linear:

$$C_D^{\infty} = \frac{24}{Re_b}. \tag{2.8}$$

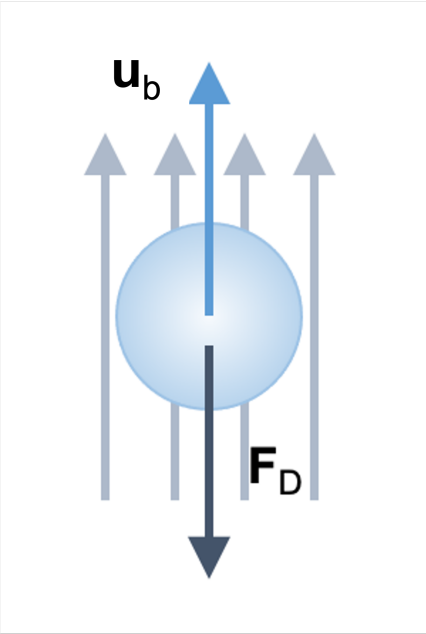

Figure 2.1: Representation of the drag force $\boldsymbol{F}_D$ for a bubble with velocity $\boldsymbol{u}_b$ in an rising liquid flow.

However, in bubble columns the gas velocity is usually much larger than the Stokesian limit and Eq. (2.8) cannot be applied. Consequentially, several empirical and semi-empirical correlations have been developed for the calculation of C_D^∞ for bubbly dispersed flows.
The first one was proposed by Schiller and Naumann [76] for rigid spherical particles in liquid media and has been also applied for gas bubbles as well:

$$C_D^\infty = \begin{cases} \frac{24}{Re_b}\left(1 + 0.15 Re_b^{0.687}\right) & Re_b \leq 10^3 \\ 0.44 & Re_b > 10^3 \end{cases} \tag{2.9}$$

Grace [77], Clift [78] and Ishii and Zuber [79] first proposed correlations for C_D^∞ valid for deformable bubbles in liquid media; in particular the drag coefficient proposed by Ishii and Zuber is still of common use nowadays: it is assumed that, for small Reynolds numbers, the bubbles have spherical shape, hence the relative drag coefficient, $C_{D,\mathrm{sph}}^\infty$ is calculated as in Eq. (2.9), but using a mixture Reynolds number, Re_m, calculated as in Eq. (2.7) replacing the liquid viscosity μ_k with the mixture viscosity μ_m:

$$\mu_m = \mu_l \left(1 - \alpha_g\right)^{-2.5\mu^*} \tag{2.10}$$

where

$$\mu^* = \frac{\mu_g + 0.4\mu_l}{\mu_l + \mu_g}. \tag{2.11}$$

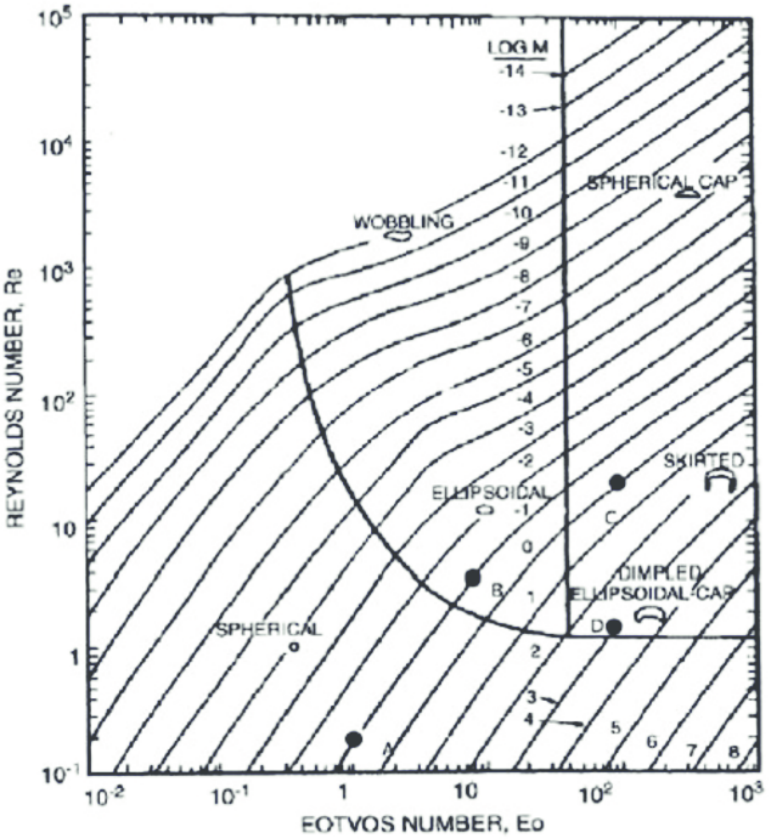

Figure 2.2: Bubble shapes regime diagram (extracted from [78]).

At higher Reynolds number the bubbles change their shape due to the intense viscous stress at their surface, entering into the ellipsoidal or cap regime (Fig. 2.2). In such case, in the calculation of the drag coefficient a new parameter becomes relevant, which is the bubble Eötvös number, Eo_b, expressing the ratio between gravitational and interface tension forces and thus quantifying the bubble deformation:

$$Eo_b = \frac{(\rho_l - \rho_g) g d_b^2}{\gamma}, \tag{2.12}$$

where γ is the surface tension.
The drag coefficient for an isolated ellipsoidal bubble is then calculated as:

$$C_{D,\text{ell}}^{\infty} = \frac{2}{3} E_\alpha \sqrt{Eo_b} \tag{2.13}$$

being

$$E_\alpha = \left(\frac{1 + 17.67 f^{6/7}}{18.67 f} \right)^2 \tag{2.14}$$

and

$$f = \frac{\mu_l}{\mu_m}\sqrt{1-\alpha_g}. \tag{2.15}$$

In the cap regime, the drag coefficient is considered independent from both Reynolds and Eötvös:

$$C^{\infty}_{D,\text{cap}} = \frac{8}{3}\sqrt{1-\alpha_g}. \tag{2.16}$$

Finally, the drag coefficient for deformable isolated bubbles according to Ishii and Zuber [79] may be written as:

$$C^{\infty}_{D} = \begin{cases} C^{\infty}_{D,\text{sph}} & \text{if} C^{\infty}_{D,\text{sph}} \geq C^{\infty}_{D,\text{ell}} \\ \min[C^{\infty}_{D,\text{cap}}, C^{\infty}_{D,\text{ell}}] & \text{if} C^{\infty}_{D,\text{sph}} < C^{\infty}_{D,\text{ell}} \end{cases} \tag{2.17}$$

To conclude, Tomiyama recently proposed three different correlations for C^{∞}_{D} [80] for deformable bubbles in air-water systems, according to the degree of contamination of the liquid phase.
If ultra-pure water is used as continuous phase:

$$C^{\infty}_{D} = \max\left[\min\left[\frac{16}{Re_b}\left(1+0.15Re_b^{0.687}\right), \frac{48}{Re_b}\right]\frac{8}{3}\frac{Eo_b}{Eo_b+4}\right] \tag{2.18}$$

when the water is partially contaminated:

$$C^{\infty}_{D} = \max\left[\min\left[\frac{24}{Re_b}\left(1+0.15Re_b^{0.687}\right), \frac{72}{Re_b}\right]\frac{8}{3}\frac{Eo_b}{Eo_b+4}\right] \tag{2.19}$$

and, finally, when the water is fully contaminated:

$$C^{\infty}_{D} = \max\left[\frac{24}{Re_b}\left(1+0.15Re_b^{0.687}\right)\frac{8}{3}\frac{Eo_b}{Eo_b+4}\right] \tag{2.20}$$

At low Re_b it was shown that the drag coefficient correlations described above are broadly equivalent [81] in the homogeneous regime, given the spherical shape of the bubbles; however, when the gas velocity increases and the bubbles start changing their shape, Eq. (2.9) significantly underestimates C^{∞}_{D}, confirming that the bubbles deformation plays a predominant role in the calculation of the drag force.

Swarm factor

The correlations discussed in the previous paragraph were all developed for isolated bubbles. In bubble columns, this assumption corresponds to reality only at extremely low gas velocity, when the few bubbles are spherical and far enough each other to be approximated as isolated. In the overwhelming majority of cases, bubbles are close to each other and arrange themselves in structure called swarms [82]. As a consequence, the drag force experienced by one bubble in a cluster is different

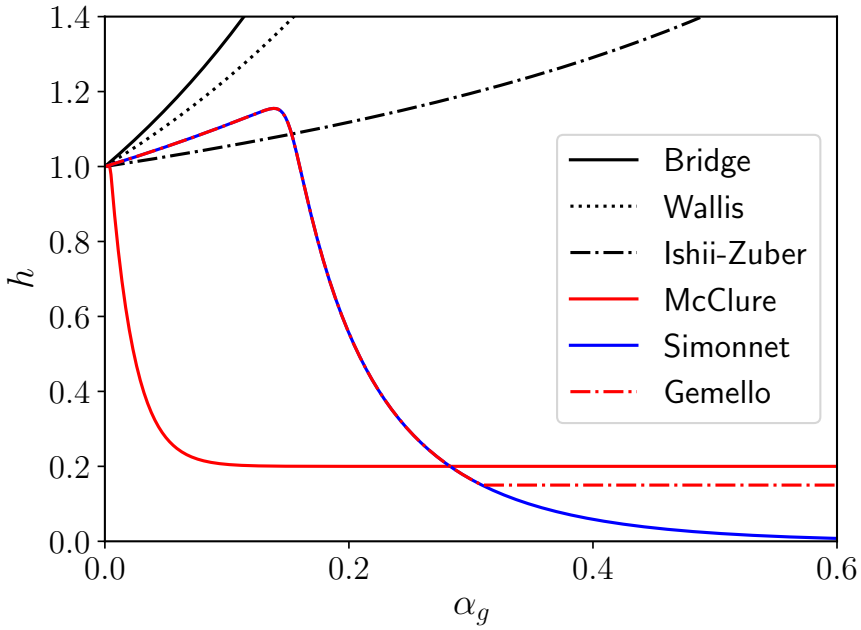

Figure 2.3: Swarm factors as function of the local gas fraction according to correlations available in the literature: Bridge et al. [83], Wallis et al. [84], Ishii and Zuber [82], McClure et al. [29], Simonnet et al. [85], Gemello et al. [16].

and the drag coefficient must be adjusted in order to take into account the so-called swarm effect:

$$h = \frac{C_D}{C_D^{\infty}} \tag{2.21}$$

In the past decades, several correlations were developed for assessing the swarm effect and the relative coefficient h as a function of the local gas fraction α_g and the most relevant are plotted in Fig. 2.3.
The first expressions proposed shared the same general formulation

$$h = (1 - \alpha_g)^{-2n} \tag{2.22}$$

with n varying from 1.39 [83], 1 [84] or 0.25 [79].
Rhogair et al. [86] developed a correlation valid for gas hold up to 0.5, medium to high Reynolds number and $1 \leq Eo_b \leq 5$:

$$h = \left(1 + \frac{18\alpha_g}{Eo_b}\right)(1 - \alpha_g)\,. \tag{2.23}$$

The characteristic of Eq. (2.22) and (2.23) is that h has a monotonic increasing behavior and thus enhances the drag force, hinders the bubble rise and contributes to the increase of the gas hold up even at high gas velocity. As a consequence, at

high gas velocity the predicted crowding of bubbles is excessive and may generate nonphysical results and convergence issues. For this purpose, Simonnet et al. [85] first proposed a statistical-empirical correlation for h, valid for α_g up to 0.3 and with two different trends: h increases until α_g reaches the critical value of 0.15 and then it slowly decays to 0:

$$h = (1-\alpha_g)\left((1-\alpha_g)^{25} + \left(4.8\frac{\alpha_g}{1-\alpha_g}\right)^{-\frac{2}{25}}\right). \tag{2.24}$$

McClure et al. [87] proposed another empirical correlation valid for the same range of gas hold up:

$$h = \min\left[(1-\alpha_g)^{50} + b, 1\right] \tag{2.25}$$

where b is a fitting parameter depending on the sparger properties.
The swarm factor proposed by Simonnet in Eq. (2.24) was then modified by McClure et al. [88] neglecting the hindering effect and thus limiting h to 1:

$$h = \min\left[h_{\text{Sim}}, 1\right] \tag{2.26}$$

where h_{Sim} denotes the swarm factor ad calculated in Eq. (2.24). This modification was further adjusted [29] reducing h_{Sim} to $0.8h_{\text{Sim}}$ when h_{Sim} is lower than 1.
Gemello et al. [16] claimed that the swarm factor proposed by Simonnet caused convergence issues and nonphysical bubble clustering at high gas velocity, therefore they have limited it with a minimum value h_0, ranging from 0.08 to 0.25 according to the gas velocity and operating conditions:

$$h = \max\left[h_{\text{Sim}}, h_0\right]. \tag{2.27}$$

Lift force

The lift force arises from a local shear rate in the flow field of the liquid phase that induces a lateral motion of the bubbles (Fig. 2.4), which could be either toward the walls or the center of the column:

$$\boldsymbol{F}_L = C_L \alpha_g \rho_l \left(\boldsymbol{u}_g - \boldsymbol{u}_l\right) \times \nabla \times \boldsymbol{u}_l. \tag{2.28}$$

C_L is the lift coefficient and it can be either set to a constant value or calculated through a correlation. In the first case, the most popular assumption is to set it equal to 0.5 [17,21,22,89]. Tabib et al. [10] tested more values of C_L and concluded that it should be set according to the bubble size. In this light, Tomiyama developed a correlation for C_L as a function of the bubble size [90] for viscous systems:

$$C_L = \begin{cases} \min\left[0.288\tanh\left(0.121Re_b\right), f(Eo'_b)\right] & Eo'_b < 4 \\ f(Eo'_b) & 4 \leq Eo'_b \leq 10.7 \\ -0.288 & Eo'_b > 10.7 \end{cases} \tag{2.29}$$

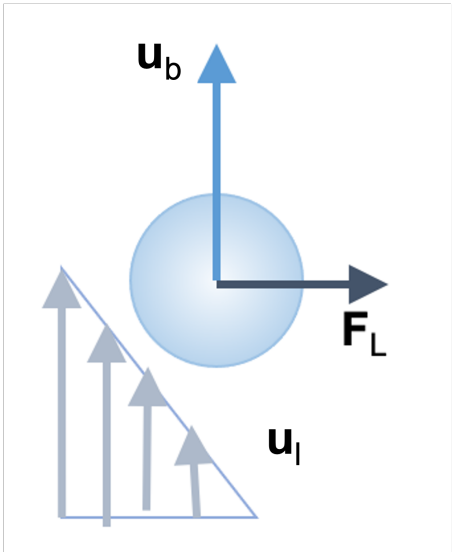

Figure 2.4: Representation of the lift force acting on a bubble with velocity $\boldsymbol{u}_b$ in a liquid with velocity $\boldsymbol{u}_l$.

with

$$f(Eo'_b) = 0.0010422Eo'^3_b - 0.0159Eo'^2_b - 0.0204Eo'_b + 0.474, \tag{2.30}$$

$$Eo'_b = \frac{g(\rho_l - \rho_g)d_H^2}{\gamma} \tag{2.31}$$

and d_H being the maximum horizontal dimension of the bubbles. It could be set equal to d_b, assuming a spherical shape of bubbles, or estimated through the correlation of Wellek et al. [91]:

$$d_H = d_b \left(1 + 0.163Eo^{0.757}\right)^{1/3}. \tag{2.32}$$

Correlations that had been originally developed for solid particles were then used for gas bubbles or liquid drops as well, such as the one proposed by Moraga [92]:

$$C_L = \begin{cases} 0.0767 & \varphi \leq 6 \cdot 10^3 \\ -(0.12 - 0.2\exp\left[-\frac{\varphi}{3.6} \cdot 10^{-5}\right]\exp\left[\frac{\varphi}{3} \cdot 10^{-7}\right] & 6 \cdot 10^3 < \varphi < 5 \cdot 10^7 \\ -0.6353 & \varphi \geq 5 \cdot 10^7 \end{cases} \tag{2.33}$$

with $\varphi = Re_b Re_\omega$. In particular, Re_ω is the vorticity Reynolds number defined as:

$$Re_\omega = \frac{\rho_l d_b^2 |\nabla \times \boldsymbol{u}_l|}{\mu_l} \tag{2.34}$$

Another correlation proposed by Legendre and Magnaudet [93] for solid particles was also used for bubbles, but its validity is limited to a maximum $Re_b = 500$:

$$C_L = \sqrt{\left(\frac{6}{\pi^2}\frac{2.255}{\sqrt{SrRe_b}\left(1+0.2Re_b/Sr\right)^{3/2}}\right)^2 + \left(\frac{1}{2}\frac{Re_b+16}{Re_b+29}\right)^2}, \tag{2.35}$$

with Sr being the ratio of the Reynolds vorticity number and the bubble Reynolds number:

$$Sr = \frac{Re_\omega}{Re_b} = \frac{d_b\left|\nabla\times\boldsymbol{u}_l\right|}{\left|\boldsymbol{u}_g-\boldsymbol{u}_l\right|}. \tag{2.36}$$

Eq. (2.29) provides positive lift coefficient for small bubbles, thus migrating toward the wall, and negative for big bubbles, which move toward the center of the column: the Reynolds number at which the sign inversion of C_L occurs is know as critical Reynolds number. Despite Eq. (2.29) was specifically developed for glycerol-water systems, it has been widely used in the literature for the estimation of C_L [18, 20, 23, 27, 28, 62, 94]. However, notwithstanding the recent efforts to extend the validity of Eq. (2.29) to low-viscosity systems or to identify the correct Reynolds critical number [95, 96], a complete and deep knowledge of mechanism of the lift is still missing. For this reason, coupled with a non-predominant effect compared to the drag force [74], the lift force is often neglected in simulating circular bubble columns, especially if the gas supply is uniform [16, 88, 97] and its activation does not actively contribute to improve the quality of the results.

Turbulent dispersion force

The turbulent dispersion force arises from the presence of turbulent liquid eddies and their interaction with bubbles (Fig. 2.5). The most popular expression for the description of the turbulent dispersion force in bubble columns was proposed by Lopez de Bertodano [98] assuming an analogy with the molecular motion of diffusion:

$$\boldsymbol{F}_{TD} = -C_{TD}\rho_l k_l \nabla\alpha_g \tag{2.37}$$

where k_l is the liquid turbulent kinetic energy and C_{TD} the turbulent dissipation coefficient. As for C_L, several values were tested for C_{TD} during the last decades; the majority of those fall in the range between 0 and 0.6 [10, 27, 30, 99], however, the impact of the variation of this coefficient in the above range was proved to be negligible [11], especially in the homogeneous regime.
Burns et al. [100] derived an alternative expression of the turbulent dispersion force performing a Favre average on the drag term:

$$\boldsymbol{F}_{TD} = \frac{3}{4}C_D Re_b \rho_l \frac{\nu_l\nu_{l,t}}{\sigma_{TD}d_b^2}\alpha_g\left(\frac{1}{\alpha_g}+\frac{1}{\alpha_l}\right) \tag{2.38}$$

with σ_{TD} usually set to 0.9.

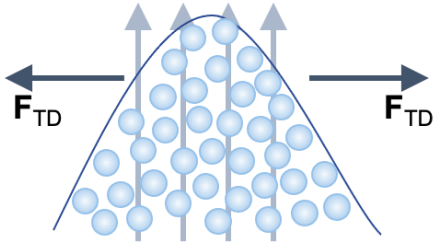

Figure 2.5: Action of the turbulent dispersion force on a localized group of bubbles moving in a liquid.

Wall lubrication force

The presence of the walls produces an extra force on the bubble that pushes it away (2.6) toward the center of the column, representing a sort of limit of the possible lateral motion of the bubbles. This effect is described by the wall lubrication force, $\boldsymbol{F}_{VM}$, which is sometimes seen as a fictitious limitation to an excessive lateral motion of the bubbles, since its formulation does not originate from a rigorous force balance on the bubble:

$$\boldsymbol{F}_{WL} = C_{WL}\rho_l\alpha_g|(\boldsymbol{u}_l - \boldsymbol{u}_g)_t|^2\boldsymbol{i}_w \tag{2.39}$$

where the subscript t denotes the tangential component and $\boldsymbol{i}_w$ is the versor perpendicular to the wall and pointing to the center of the column.
C_{WL} is the wall lubrication coefficient and it is mainly calculated as proposed by Tomiyama [80],who adjusted the relation proposed by Antal et al. [101]. Similar correlations were then developed by Frank et al. [102] and Hosokawa et al. [103]. According to Tomiyama:

$$C_{WL} = C_w\frac{d_b}{2}\left(\frac{1}{y_w^2} - \frac{1}{(D-y_w)^2}\right) \tag{2.40}$$

where y_w is the distance from the closest wall and C_w is evaluated as

$$C_w = \begin{cases} 0.47 & Eo_b < 1 \\ \exp\left[-0.933Eo_b + 0.179\right] & 1 \leq Eo_b < 5 \\ 0.00599Eo_b - 0.0187 & 5 \leq Eo_b < 33 \\ 0.179 & Eo_b \geq 33 \end{cases}. \tag{2.41}$$

Given its nature, the wall lubrication force is relevant only in small pipes or in the region immediately close to the walls, and therefore it is often neglected when

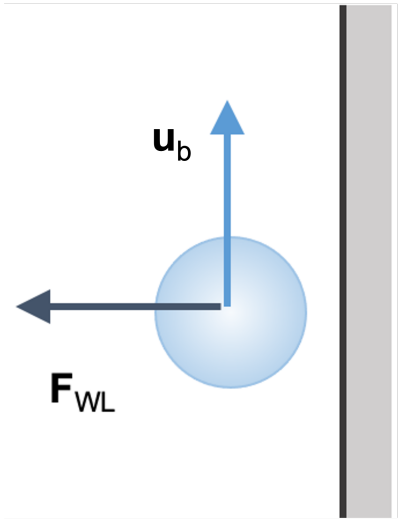

Figure 2.6: Representation of the wall lubrication force for a bubble with rising velocity $\boldsymbol{u}_b$ in the proximity of a wall.

simulating circular bubble columns. It was noted that it may help reducing computational issues at the corner in rectangular bubble columns [104].

Virtual mass force

To conclude, the virtual mass force, also referred to as added mass force, originates from the inertia of the liquid surrounding accelerating bubbles (Fig. 2.7):

$$\boldsymbol{F}_{VM} = C_{VM}\rho_l\alpha_g\left(\frac{\partial \boldsymbol{u}_l}{\partial t} + \boldsymbol{u}_l \cdot \nabla \boldsymbol{u}_l + \frac{\partial \boldsymbol{u}_g}{\partial t} + \boldsymbol{u}_g \cdot \nabla \boldsymbol{u}_g\right) \tag{2.42}$$

with C_{VM} being the virtual mass coefficient, usually set to 0.5 [17, 21, 89, 105]. Nevertheless, the majority of the studies reported that the activation of the virtual mass force has extremely little effect on the global fluid dynamics, especially when considering time-averaged properties [10, 74], therefore it is usually neglected to reduce the computational demand.

2.3 Blending modeling

In Section 2.2 'continuous' and 'dispersed' phase were extensively mentioned, presuming that, at least in the bubbly flows investigated in this work, the former is invariably the liquid and the latter is the gas. However in bubble columns this is not always the case: in the top space, i.e. the space above the free surface of the liquid, the situation is the opposite, since there is a fine dispersion of liquid droplets in the air, which becomes here the continuous phase. Therefore, phase inversion occurs

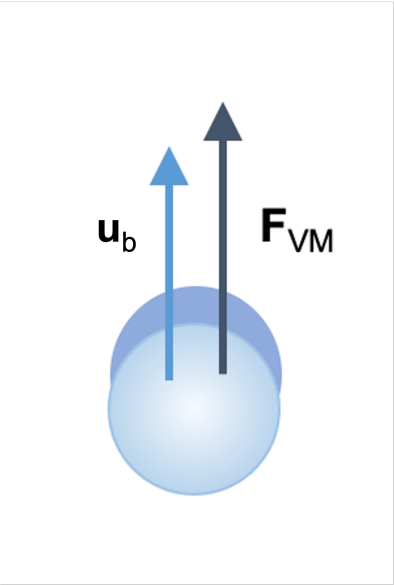

Figure 2.7: Representation of the virtual mass force on a bubble with rising velocity $\boldsymbol{u}_b$.

and an accurate modeling of the system should account for this phenomenon. This is achieved with blending models, which usually modify the interphase forces term in Eq. (2.4) to take somehow into consideration the phase inversion.

2.3.1 Symmetric blending

The symmetric blending is the simplest and most immediate approach and it is common among commercial CFD solvers [106], which often present a huge drawback: the dispersed and continuous phase must be specified *a priori* and can not change in the domain. In such case, phase inversion is not contemplated. Nevertheless, as aforementioned, in bubble columns it actually occurs above the liquid surface and, therefore, an adjustment is necessary to maintain numerical stability. The symmetric blending model overcomes this issues by multiplying the entire multiphase force term by the volume fraction of the continuous phase, which, in bubble columns, is the liquid phase:

$$\tilde{\boldsymbol{F}} = \alpha_l \boldsymbol{F}. \tag{2.43}$$

where the tilde denotes the blended term.
In most cases the volumetric force $\boldsymbol{F}$ is proportional to α_g and, consequentially, the blended force term is proportional to $\alpha_l \alpha_g$. Fig. 2.8 depicts the behavior of the unblended and blended force term with the gas fraction α_g (equal to $1 - \alpha_l$, being only two phases present). The blended term, which has a symmetrical shape

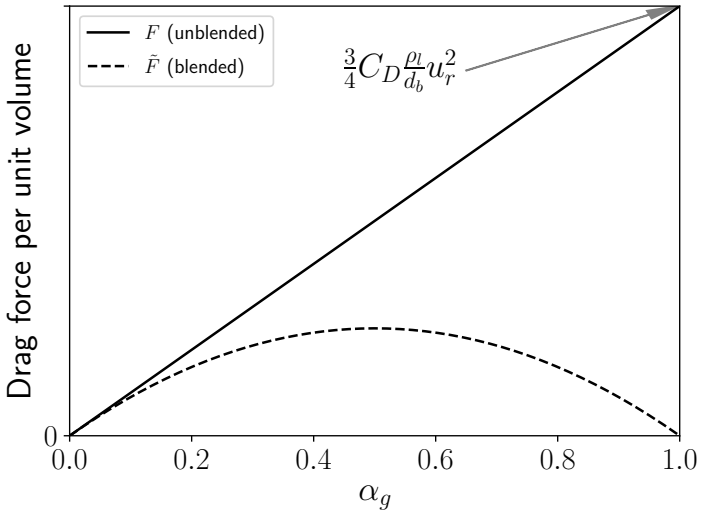

Figure 2.8: Schematic representation of the symmetric blending model as a function of the volume gas fraction: unblended (solid line) and blended (dashed line) forces term.

giving its name, corresponds to the original force term only at low gas velocity and it is then reduced due to the multiplication of the liquid volume fraction α_l. At medium-high values of gas fraction the reduction due to the blending is significant and, as the gas fraction approaches to zero and the liquid phase becomes dispersed, $\tilde{\boldsymbol{F}}$ reaches zero as well.
The advantage of this approach is the numerical stability achieved at high gas fraction, where the phase inversion is approached and gas becomes the continuous phase: in this scenario, the use of the unblended term would inevitably lead the simulation to divergence, because, in this range of α_g, there are not anymore dispersed bubbles on which calculate drag, lift and other forces.
On the other hand, the reduction imposed by this blending mechanism seems too simplistic and arbitrary: according to Fig. 2.8 the phase inversion occurs at $\alpha_g = 0.5$ due to the intrinsic symmetry of the model, while experimental measurements suggest a value between 0.7 and 0.8 [107].

2.3.2 OpenFOAM blending

The open source CFD software `OpenFOAM` includes a finer description of the blending mechanism, which is tunable by the user through the specification of some input parameters. Moreover, unlike the symmetric model, dispersed and continuous phase must not be set in advance and they can vary locally in the domain according to the defined blending parameters. Phase inversion is thus actually accounted for and each phase can be either dispersed or continuous in different zones of the domain.

Under this basis, it is possible to specify different laws for the force coefficient according to the dispersion type: i.e. it could be selected the Tomiyama drag coefficient (Eq. (2.19)) for the air-in-water dispersion and the Schiller-Naumann coefficient (Eq. (2.9)) for the water-in-air dispersion, as well as for the lift force or the remaining interfacial forces.
The blending mechanism implemented in OpenFOAM can be summarized as follows:

$$\tilde{\boldsymbol{F}} = (1 - f_1)\boldsymbol{F}^{a/w} + f_2\boldsymbol{F}^{w/a} \tag{2.44}$$

where f_1 and f_2 denote the blending coefficients respectively calculated for the gas and liquid phase and $\boldsymbol{F}^{a/w}$ and $\boldsymbol{F}^{w/a}$ are the interfacial force terms relative to the air-in-water and water-in air dispersions: the former is related the dispersion of air bubbles in the aqueous medium and the latter to the dispersion of water droplets in air.
f_1 and f_2 are function of the local volume fraction and they range from 0 to 1. The type of function used denotes the blending mechanism and it can either be linear or hyperbolic.

Linear blending

In the linear approach, f_1 and f_2 are piece-wise linear functions calculated from two parameters for each phase:

- the maximum value of the volume fraction of the phase for which it can be considered as fully dispersed, $\alpha_{i,FD}$. Default value is 0.3;
- the maximum value of the volume fraction of the phase for which it can be considered as partially dispersed, $\alpha_{i,PD}$. Default value is 0.5.

f_1, the blending coefficient for the gas phase, is then calculated as:

$$f_1(\alpha_g) = \min\left[\max\left[\frac{\alpha_g - \alpha_{g,FD}}{\alpha_{g,PD} - \alpha_{g,FD}}, 0\right], 1\right] \tag{2.45}$$

likewise, f_2 reads as:

$$f_2(\alpha_l) = \min\left[\max\left[\frac{\alpha_{l,PD} - \alpha_l}{\alpha_{l,PD} - \alpha_{l,FD}}, 0\right], 1\right] \tag{2.46}$$

The behavior of f_1 is sketched in Fig. 2.9 as function of α_g. The water blending coefficient f_2 acts equally.
Three main ranges are clearly distinguishable:

- $0 \leq \alpha_g < \alpha_{g,FD}$, corresponding to a full air-in-water dispersion, where the corresponding forces term, $\boldsymbol{F}^{a/w}$ is not reduced;

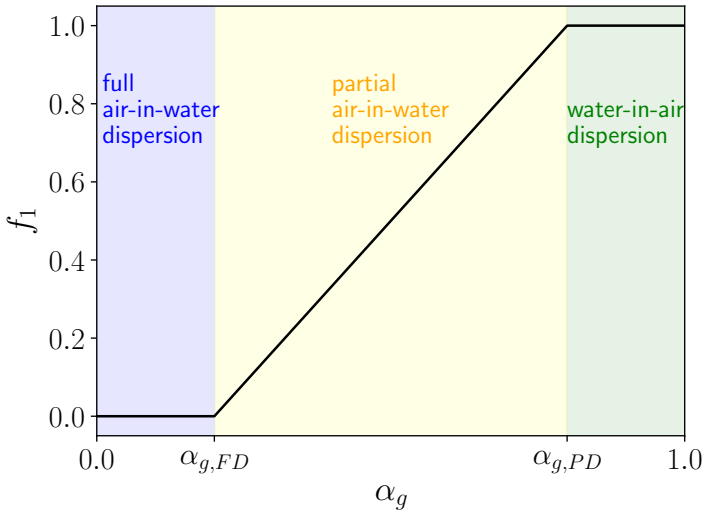

Figure 2.9: Blending coefficient f_1 as function of α_g in the linear model: the full dispersion, partial dispersion and the phase inversion ranges are clearly distinguishable.

- $\alpha_{g,FD} \leq \alpha_g < \alpha_{g,PD}$: corresponding to transition regime as phase inversion is approached. $\boldsymbol{F}^{a/w}$ is progressively reduced, and, as α_g reaches $\alpha_{g,PD}$, it decreases to zero;
- $\alpha_g \geq \alpha_{g,PD}$: air becomes the continuous phase and, therefore, the force term $\boldsymbol{F}^{a/w}$ is nullified since the system is modeled as water-in-air dispersion.

Hyperbolic blending

Analogous considerations apply for the hyperbolic model as well, where f_1 and f_2 are calculated using an exponential function, allowing a smoother transition between the three ranges. Unlikely the linear modeling, the input parameters to be provided are:

- for each phase, the maximum value of the volume fraction for the phase to be considered as dispersed $\alpha_{i,MD}$. Default value is 0.5;
- the extension of the transition range, α_{tr}. Default value is 0.3.

Hence, in the hyperbolic model, f_1 and f_2 are calculated as:

$$f_1(\alpha_g) = \frac{1 + \tanh\left[\frac{4}{\alpha_{tr}}(\alpha_g - \alpha_{g,MD})\right]}{2}, \tag{2.47}$$

$$f_2(\alpha_l) = \frac{1 + \tanh\left[\frac{4}{\alpha_{tr}}(\alpha_{l,MD} - \alpha_l)\right]}{2}, \tag{2.48}$$

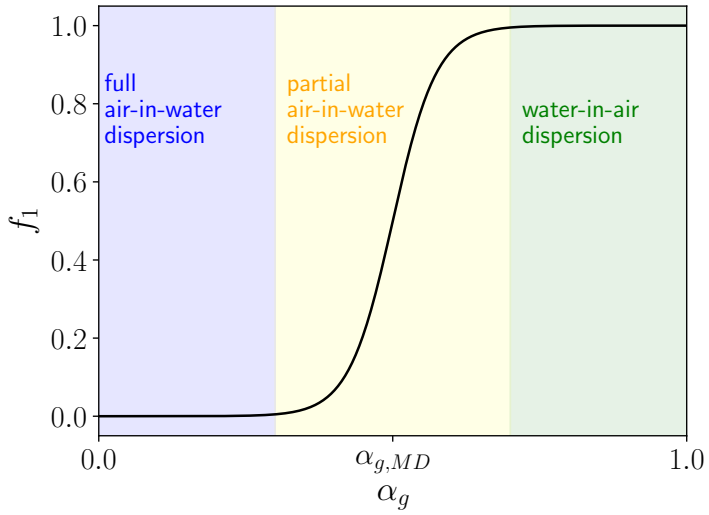

Figure 2.10: Blending coefficient f_1 as function of α_g in the hyperbolic model: the full dispersion, partial dispersion and the phase inversion ranges are clearly distinguishable.

Once more, reporting f_1 in function of the gas fraction (Fig. 2.10), the three different dispersion ranges are definitely detectable.

2.4 Turbulence modeling

Turbulence is fundamental for the correct operation of bubble columns since it enhances mass and momentum transfer, provides mixing and plays a crucial role in bubble coalescence and break-up.
However, the general phenomenon of turbulence is not entirely known yet and a thorough understanding of the first principles generating turbulence is still missing. For this reason, Richard Feynman, laureate of the Nobel Prize in Physics in 1965, was said to refer to turbulence as 'the most important unsolved problem of classical physics'.
Briefly, turbulence may be defined as a phenomenon occurring at sufficiently high Reynolds numbers, when the local velocity starts fluctuating intensely promoting the birth of turbulent eddies of different size [108]. According to the pioneering Kolmogorov theory [109] which assumes turbulence isotropy and homogeneity, the size of the turbulent eddies ranges from the largest scale of the main flow to a minimum size, called Kolmogorov length:

$$\eta = \left(\frac{\nu^3}{\epsilon}\right)^{1/4}. \tag{2.49}$$

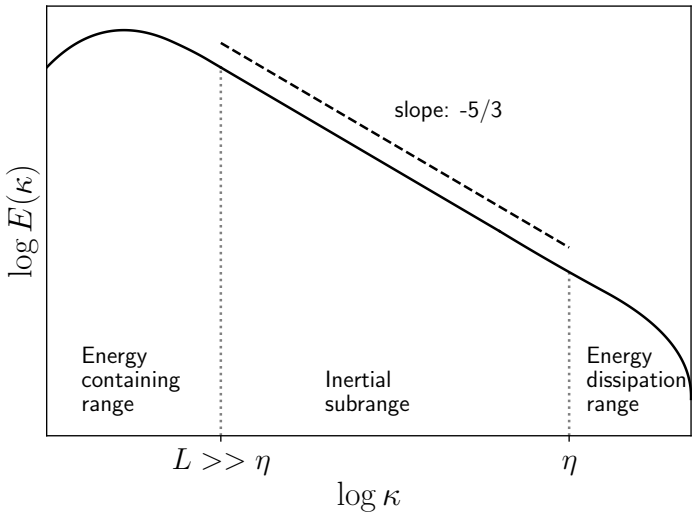

Figure 2.11: Kolmogorov turbulence spectrum.

Moreover, Kolmogorov hypothesized the so-called turbulence energy cascade, assuming that the turbulent kinetic energy is extracted from the mean flow by the larger eddies, progressively transferred to smaller eddies and eventually dissipated through viscous stresses at the Kolmogorov length scale. Those three ranges (production, inertial and dissipative) are clearly distinguishable in the Kolmogorov turbulence spectrum, depicted in Fig. 2.11. In the spectrum, $E(\kappa)d\kappa$ denotes the energy associated to the eddies with wave number between κ and $\kappa + d\kappa$ (the wave number κ is inversely proportional to the eddy length). Therefore, the kinetic energy associated to a range of eddies of given size may be calculated as:

$$k = \int E(\kappa)d\kappa. \tag{2.50}$$

Because of the intense and local velocity fluctuations, the solution of the Navier-Stokes equations becomes extremely difficult and the problem is further worsened by the non-linearity of the advective term. Therefore, turbulence must be modeled in some way. Nowadays, there are three different approaches to model turbulence:

- Reynolds Averaged Navier-Stokes (RANS) models. Turbulence is modeled at every scale of motion through the estimation of a turbulent eddy viscosity, μ_t, assuming an analogy with Newton equation for molecular viscosity on the grounds of the Boussinesq approximation [75]. A detailed description is provided in Section 2.4.1;
- Large Eddy Simulation (LES) models. Unlikely RANS models, the larger scales of motion are fully resolved, while only the scales smaller than a certain

cut-off length are modeled with the calculation of a sub-grid-scale (SGS) turbulent viscosity, μ_{SGS}. A detailed description is provided in Section 2.4.2;

- Direct Numerical Simulations (DNS). The flows is entirely computed and any modeling of the turbulence is absent. Clearly, this kind of simulations requires a computational effort tremendously larger than the previous two and it cannot be adopted for large-scale simulations. However, DNS simulation of simpler systems has been successfully used for the investigation of particular phenomena, such as bubbles deformation [110, 111] or bubble induced turbulence [112].

The peculiarity of dispersed systems is the simultaneous presence of two (or more) phases, for each one of which the turbulence must be modeled. In the peculiar case of dispersed gas-liquid flows, there are three different options [113]:

- Per-phase turbulence approach. Both liquid and gas phases are modeled as turbulent and, therefore, a turbulent viscosity should be calculated for each of them, regardless of the used models. It is rarely used in the simulation of bubble columns since the gas turbulence may often be neglected, thus saving computational resources;

- Mixture turbulence approach. Used in dispersed flows only when the phases have comparable density, it models only mixture turbulence based on the mixture properties and variables;

- Dispersed turbulence approach. Only the liquid phase is assumed to be turbulent while the turbulence of the gas phase is neglected. Given the density difference between the liquid and the gas phase, this approach is the most used for bubbly flows and is the one adopted in this thesis.

2.4.1 RANS models

The key feature of the RANS models is the application of the Reynolds decomposition to the flow variables ϕ, which are split in a mean ($\bar{\phi}$) and fluctuating (ϕ') part:

$$\phi = \bar{\phi} + \phi'. \tag{2.51}$$

Applying the Reynolds decomposition to the continuity (Eq. (2.3)) and Navier-Stokes (Eq. (2.4)), assuming again negligible mass transfer, they may be written as:

$$\frac{\partial}{\partial t}\left(\alpha_i \rho_i\right) + \nabla\left(\alpha_i \rho_i \bar{\boldsymbol{u}}_i\right) = 0, \tag{2.52}$$

$$\frac{\partial}{\partial t}\left(\rho_i \alpha_i \bar{\boldsymbol{u}}_i\right) + \nabla\cdot\left(\rho_i \alpha_i \bar{\boldsymbol{u}}_i \bar{\boldsymbol{u}}_i\right) = -\alpha_i \nabla \bar{p} + \rho_i \alpha_i \boldsymbol{g} + \alpha_i \mu_i \nabla^2 \bar{\boldsymbol{u}}_i + \nabla\cdot\left(\alpha_i \rho_i \overline{\boldsymbol{u}_i' \boldsymbol{u}_i'}\right) + \boldsymbol{F}. \tag{2.53}$$

The usage of the Reynolds decomposition on the Navier-Stokes equations generated a new unknown term in Eq. (2.53) called Reynolds stress tensor, $\boldsymbol{\tau}_i$:

$$\boldsymbol{\tau}_i = \rho_i \overline{\boldsymbol{u}_i' \boldsymbol{u}_i'} \tag{2.54}$$

The estimation of the unknown quantity $\boldsymbol{\tau}_i$ generates a closure problem: additional transport equations for the six independent components of $\boldsymbol{\tau}_i$ would generate more unknown quantities (each one being a component of a third-order tensor) and so on. The solution of this issue is based on the Boussinesq approximation [75], which proposes an analogy of the Reynolds stress tensor with the viscous stress tensor $\boldsymbol{\sigma}_i$ (Eq. (2.5)), assuming that it is dependent on the mean velocity gradient:

$$\boldsymbol{\tau}_i = \mu_{i,t} \left(\nabla \bar{\boldsymbol{u}}_i + (\nabla \bar{\boldsymbol{u}}_i)^T \right) - \frac{2}{3} \left(\rho_i k_i + \mu_{i,t} \nabla \cdot \bar{\boldsymbol{u}}_i \right) \boldsymbol{I} \tag{2.55}$$

$\mu_{i,t}$ is the turbulent viscosity of phase i and its calculation is the core of the RANS models. In bubble columns modeling, the two equation models are the most popular choice [114], which calculate $\mu_{i,t}$ from two additional turbulent quantities. Those quantities are the turbulent kinetic energy and the turbulent dissipation rate (k-ϵ models) or the specific dissipation rate (k-ω models) and they are computed with additional transport equations.

k-ϵ models

In k-ϵ models additional transport equations for the turbulent kinetic energy and dissipation rate are solved. The first k-ϵ model proposed is also known as standard k-ϵ [115] and it was developed on the assumption of fully turbulent flows. Considering the liquid phase:

$$\begin{aligned} &\frac{\partial}{\partial t} \left(\alpha_l \rho_l k_l \right) + \nabla \cdot \left(\alpha_l \rho_l k_l \bar{\boldsymbol{u}}_l \right) = \\ &\qquad = \nabla \cdot \left(\alpha_l \left(\mu_l + \frac{\mu_{l,t}}{\sigma_k} \right) \nabla k_l \right) + \alpha_l \left(G_{k,l} + G_{b,l} - \rho_l \epsilon_l \right) + \alpha_l \rho_l S_{k,l} \end{aligned} \tag{2.56}$$

$$\begin{aligned} &\frac{\partial}{\partial t} \left(\alpha_l \rho_l \epsilon_l \right) + \nabla \cdot \left(\alpha_l \rho_l \epsilon_l \bar{\boldsymbol{u}}_l \right) = \\ &= \nabla \cdot \left(\alpha_l \left(\mu_l + \frac{\mu_{l,t}}{\sigma_\epsilon} \right) \nabla \epsilon_l \right) + \alpha_l \frac{\epsilon_l}{k_l} \left(C_{1,\epsilon} G_{k,l} + C_{1,\epsilon} C_{3,\epsilon} G_{b,l} - C_{2,\epsilon} \rho_l \epsilon_l \right) + \alpha_l \rho_l S_{\epsilon,l} \end{aligned} \tag{2.57}$$

where

- σ_k and σ_ϵ are the Prandtl turbulent numbers;

- $G_{k,l}$ and $G_{k,l}$ are production terms expressing the generation of turbulent kinetic energy due respectively to the mean gradients of the flows and buoyancy effects;
- $S_{k,l}$ and $S_{\epsilon,l}$ take into account other possible source terms;
- $C_{1,\epsilon}, C_{2,\epsilon}, C_{3,\epsilon}$ are model constants.

The liquid turbulent viscosity is therefore calculated as

$$\mu_{l,t} = C_\mu \rho_l \frac{k_l^2}{\epsilon_l} \tag{2.58}$$

with $C_\mu = 0.09$.
The standard k-ϵ model proved excellent performance in modeling turbulent isotropic flows at high Reynolds number, but showed shortcomings in describing swirling flows, curvature flows and flows at low and medium Reynolds number. For this reason several variants were proposed, among which the RNG k-ϵ and the realizable k-ϵ models stand out. The former is obtained by applying the renormalization group theory to the Navier Stokes equations [116] and adds an extra production term in the turbulent dissipation rate transport equation, providing better results for medium-low Reynolds number. The realizable k-ϵ model, on the other hand, calculates ϵ_l using a transport equation based on the the mean square vorticity fluctuation [117]. This approach is particular successful in modeling swirling flows and flows near curvatures.
All these three models have been extensively used for simulating bubble columns [21, 23, 24, 39, 105, 118, 119], even though it was recently shown the better performance of the RNG k-ϵ, especially for high gas velocity [15, 16].

k-ω models

k-ω models estimate the turbulent viscosity through the kinetic turbulent energy and the specific turbulent dissipation rate ω, which, similarly to the k-ϵ models, are computed solving two additional transport equations [120]. Those models were proven to be more effective for boundary-bounded turbulent flows (wall functions are not required) and flows at low Reynolds number. In the case of the liquid phase, the specific turbulent dissipation rate is defined as:

$$\omega_l = \frac{\epsilon_l}{k_l} \tag{2.59}$$

In the standard formulations, the transport equations for k_l and ω_l are:

$$\frac{\partial}{\partial t}\left(\alpha_l \rho_l k_l\right) + \nabla \cdot \left(\alpha_l \rho_l k_l \bar{\boldsymbol{u}}_l\right) = \nabla \cdot \left(\alpha_l \left(\mu_l + \frac{\mu_{l,t}}{\sigma_k}\right) \nabla k_l\right) + \alpha_l G_{k,l} + \alpha_l \rho_l S_{k,l} \tag{2.60}$$

$$\frac{\partial}{\partial t}\left(\alpha_l \rho_l \omega_l\right) + \nabla \cdot \left(\alpha_l \rho_l \omega_l \bar{\boldsymbol{u}}_l\right) = \nabla \cdot \left(\alpha_l \left(\mu_l + \frac{\mu_{l,t}}{\sigma_\omega}\right) \nabla \omega_l\right) + \alpha_l G_{\omega,l} + \alpha_l \rho_l S_{\omega,l} \quad (2.61)$$

with σ_k σ_ω being the Prandtl turbulent numbers, $G_{k,l}$ and $G_{\omega,l}$ the production terms and $S_{k,l}$ and $S_{\omega,l}$ additional source terms eventually specified by the user.
A popular variation is the shear stress transport (SST) k-ω model, [121] which adopts the k-ω formulations in the viscous sub-layer close to the walls and k-ϵ in the free-stream zones, overcoming the excessive dependence of the k-ω model on the boundary conditions in free-stream condition.
k-ω turbulence models are less popular than k-ϵ in the description of bubble columns [16, 119, 122] even though the quality of the results is comparable.

2.4.2 LES models

The large eddy simulation models rely on a filtering rather than an averaging procedure of the flow variables. In this case, the filtered part of the variable, $\bar{\phi}(\boldsymbol{x}, t)$ is obtained through the application of a filter function $G(\boldsymbol{x}, t)$ to the unfiltered variable $\phi(\boldsymbol{x}, t)$:

$$\bar{\phi}(\boldsymbol{x}, t) = \int_{-\infty}^{+\infty} \int_{-\infty}^{+\infty} \phi(\boldsymbol{\xi}, \tau) G(\boldsymbol{x} - \boldsymbol{\xi}, t - \tau) d\tau d\boldsymbol{\xi} \quad (2.62)$$

with the unfiltered part, related to the small scales of motion, or subgrid-scales (SGS):

$$\phi' = \phi - \bar{\phi} \quad (2.63)$$

The filter equation $G(\boldsymbol{x}, t)$ may be of different kinds and shapes and a detailed list may be found in the study by Sagaut [123]. However, the most straightforward choice is the top hat filter, which, neglecting the time-based filtering, may be written as:

$$G(\boldsymbol{x} - \boldsymbol{\xi}) = \begin{cases} \frac{1}{\Delta} & |\boldsymbol{x} - \boldsymbol{\xi}| \leq \frac{\Delta}{2} \\ 0 & \text{elsewhere} \end{cases} . \quad (2.64)$$

and it is represented in Fig. 2.12.
In brief, when the top hat filter is applied, the motion related to the scales larger than Δ are filtered out and hence completed resolved, while the subgrid-scale, smaller than Δ, must be modeled in some way.
The application of the filtering process to the momentum transfer equation yields (considering, in the sake of simplicity, a single-phase flow):

$$\frac{\partial \bar{\boldsymbol{u}}}{\partial t} + \nabla \cdot \left(\overline{\boldsymbol{u}\boldsymbol{u}}\right) = \nu \nabla^2 \bar{\boldsymbol{u}} - \frac{1}{\rho} \nabla \bar{p} \quad (2.65)$$

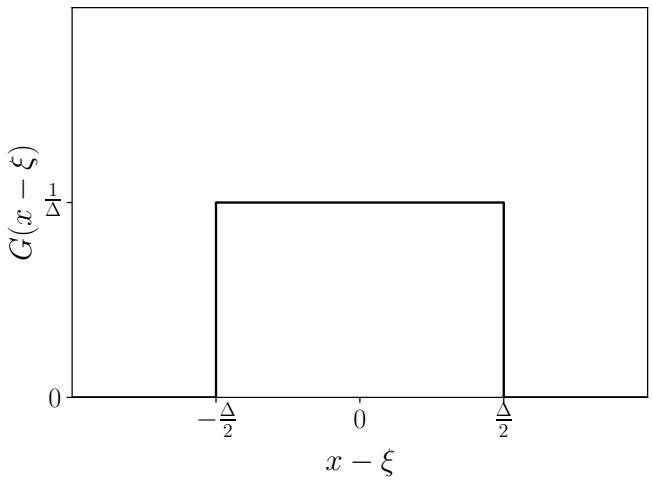

Figure 2.12: 1-dimension top hat filter.

the advective term $\overline{\boldsymbol{u}\boldsymbol{u}}$ is not known and, after some math, it can be split in several terms:

$$\overline{\boldsymbol{u}\boldsymbol{u}} = \bar{\boldsymbol{u}}\bar{\boldsymbol{u}} + \boldsymbol{C} + \boldsymbol{L} + \boldsymbol{R}: \tag{2.66}$$

- $\boldsymbol{C} = \overline{\bar{\boldsymbol{u}}\boldsymbol{u}'}$ is the cross-term stress representing the interactions between the solved and modeled scales and cannot be computed exactly, it is usually ignored at high Reynolds number [124];
- $\boldsymbol{L} = \overline{\bar{\boldsymbol{u}}\bar{\boldsymbol{u}}} - \bar{\boldsymbol{u}}\bar{\boldsymbol{u}}$ is the Leonard stress and describes the interactions between the large scales [125]: it can be directly calculated [126], approximated or neglected [120];
- $\boldsymbol{R} = \overline{\boldsymbol{u}'\boldsymbol{u}'}$ is the Reynolds sub-grid stress tensor and express the interactions at smaller (i.e. modeled) scales [124].

The summation of $\boldsymbol{C}$, $\boldsymbol{L}$ and $\boldsymbol{R}$ is denoted as subgrid tensor $\boldsymbol{\tau}$:

$$\boldsymbol{\tau} = \boldsymbol{C} + \boldsymbol{L} + \boldsymbol{R}. \tag{2.67}$$

Eq. (2.67) is the core of the LES framework and the choice of the models describing the subgrid scale is of crucial matter. If the cross-term and the Leonard stresses are assumed to be negligible, then the whole modeling of the LES approach comes down to the modeling of the subgrid scale.
Assuming, once more, the validity of the Boussinesq approximation which, in the LES case, relies on the similarity of the energy transfer from the larger to the smaller scale and the molecular diffusion, the deviatoric part of $\boldsymbol{\tau}$, $\boldsymbol{\tau}^d$ may be written as:

$$\boldsymbol{\tau}^d = -\nu_{SGS}\left(\nabla\bar{\boldsymbol{u}} + (\nabla\bar{\boldsymbol{u}})^T\right) \tag{2.68}$$

where ν_{SGS} is the subgrid viscosity.
Since the LES formulation was first developed, numerous methods for the calculation of ν_{SGS} have been proposed. Two main approaches may be distinguished [123, 127]: the functional and structural approach. In the former, the modeling effort is focused on the evaluation of the impact of the subgrid tensor $\boldsymbol{\tau}$ on the resolved scale rather than on the tensor itself; therefore, in these models, the analysis of the energy cascade is crucial. On the other hand, the structural models aim to provide an approximation of the subgrid tensor.
In the functional approach, Sagaut identified three main groups of subgrid viscosity models [123], respectively based on:

- the resolved scales. Following this approach, ν_{SGS} is calculated from the global quantities, such as the velocity or the strain rate field, at the resolved scale. Despite these models are the simplest to implement, they rely on strong assumptions, such as the the actual existence of a subgrid scale (i.e. the flow must not be entirely described by the resolved part) and the local equilibrium hypothesis, under which there is not accumulation of energy along the spectrum;

- the energy at the cut-off length Δ. These models estimate the subgrid viscosity from the energy of the resolved scale with highest frequency. Yet being based on the resolved scale as well, this kind of models only uses the local information of the flow at the cut-off scale, and not of the entire resolved scale like the previous models;

- the subgrid scale itself. These models are more complex than the previous two groups and they are based on additional information and assumptions regarding the subgrid scale.

Among the structural models, the simplest are known as similarity models because they are grounded on the hypothesis that the larger unresolved scales behave like the smallest resolved scales [128].
Nevertheless, a detailed analysis of the subgrid scale viscosity models falls outside the aim of this work: in the following a brief description of the most common applications for the calculation of μ_{SGS} in multiphase dispersed flows is provided (more details on two-phase turbulence in Section 2.4.3).

Smagorinsky model

The first pioneering work on the modeling of SGS scale was performed by Smagorinsky [129] and it has been one of the most used for both single and multiphase flows. This model is based on the resolved scale since it estimates ν_{SGS} from variables and properties of the larger scales of the flow:

$$\mu_{SGS} = \rho_l \left(C_s \Delta\right) \sqrt{2 \left|\bar{\boldsymbol{S}}\right|^2} \tag{2.69}$$

where $\bar{\boldsymbol{S}}$ is the resolved strain rate tensor

$$\bar{\boldsymbol{S}} = \frac{1}{2}\left(\nabla\bar{\boldsymbol{u}} + (\nabla\bar{\boldsymbol{u}})^T\right), \tag{2.70}$$

and C_s is a model constant. It is usually set equal to 0.1, but other values are often used up to 0.3 [124, 130–132].
Despite being over-dissipative and the several attempts in the development of more advanced formulations of the SGS eddy viscosity, the Smagorinsky model still performs remarkably well and it remains among the most popular choices for the description of the SGS scales thanks to its computational straightforwardness. A further improvement was achieved by the so-called dynamic Smagorinsky model [133], according to which the Smagorinsky constant C_s is not fixed a *a priori* but it is a function of the local resolved flow fields and it is calculated through a second filtering operation. Although the more rigorous formulation, it requires a larger computational effort and it may cause instability due to large fluctuations of the calculated C_s.

Smagorinsky-Zhang model

This model is an extension of the Smagorinsky model, specifically developed by Zhang for dispersed bubbly flows [23]. It adds to Eq. (2.69) an extra turbulent viscosity for the liquid phase accounting for the bubble induced turbulence effect (a detailed analysis is provided in Section 2.4.3) based on the original model proposed by Sato and Sekoguchi [134]:

$$\mu_{l,\text{eff}} = \mu_{l,SGS} + \mu_{l,BIT} \tag{2.71}$$

where

$$\mu_{l,BIT} = C_{\mu,BIT}\rho_l\alpha_g\left|\bar{\boldsymbol{u}}_g - \bar{\boldsymbol{u}}_l\right| \tag{2.72}$$

and $C_{\mu,BIT} = 0.6$.

Niceno model

The Smagorinsky-based models discussed above are algebraic models, since they directly calculate the SGS eddy viscosity without using additional transport equations. This approach is computationally simple because it does not provide information on the the unresolved turbulent kinetic energy: it does not account for any backscatter of turbulent energy from the small to the large scales, hence its dissipative behavior. This issue is partially overcome by the approach proposed by Niceno et al. [135], which relies on one additional transport equation for the subgrid turbulent kinetic energy, k_{SGS}

$$\frac{\partial k_{SGS}}{\partial t} + \bar{\boldsymbol{u}}\cdot\nabla k_{SGS} = \nabla\left(\left(\mu + \mu_{SGS}\right)\nabla k_{SGS}\right) + \mu_{SGS}|\bar{\boldsymbol{S}}| - C_\epsilon\frac{k_{SGS}^{3/2}}{\Delta} \tag{2.73}$$

with $C_\epsilon = 1.05$ and

$$\mu_{l,SGS} = \rho_l \rho C_k \Delta \sqrt{k_{SGS}}, \tag{2.74}$$

being $C_k = 0.094$.
The models above described were successfully used in LES simulation of bubble columns with various operating conditions [17,28,30,38,89,114,136], with different outcomes in the identification of the best SGS eddy viscosity model. However, the operating conditions in these studies, such as one dimensional flow or extremely low velocity of the gas at the injection, were quite far from industrial applications. On the contrary, in the present thesis the Smagorinsky, Smagorinsky-Zhang and Niceno models were applied to the heterogeneous regime, which is the most relevant for industrial applications, and, as discussed in Chapter 7, the Smagorinsky-Zhang model was able to best predict the local flow patterns [97].
Another specific problem of the turbulence of two-phase systems and, in particular of the LES models, is the choice of the filter length Δ, which needs to be set not only seeking that a good percentage of the overall flow must be fully resolved, but also considering the relationship with the size of the dispersed phase. As a general thumb rule, valid thus also for single phase flows, at least the 80% of the turbulent kinetic energy should be fully resolved to obtain a reliable LES simulation [137] (Fig. 2.13). Therefore, the filter length Δ should be set accordingly. However, in dispersed bubbly systems, there may be the risk that Δ is set to a value too close or too far from the bubble diameter d_b. A Δ/d_b excessively high may cause some loss of information on the mesoscale, while a low value could lead to instability since the bubble behavior may fall partially in the resolved scale and partially in the subgrid scale. Milleli et al. found that Δ/d_b should be between 1.2 and 1.5 to get optimal results [138].

2.4.3 Bubble Induced Turbulence

A peculiar and discussed phenomenon of bubbly flows is the so called bubble induced turbulence (BIT) effect. According to the BIT description, the gas bubbles transfer some energy to the liquid phase, where is then converted into turbulence and eventually dissipated. The recent literature has put a great effort into the investigation of the BIT phenomena [44] and, to this purpose, DNS simulations have shred some lights on the relevance of BIT effects [112].
The first approach for the implementations of the BIT effects is grounded on the introduction of a BIT viscosity that is summed up to the eddy viscosity calculated by the turbulence model (Eq. (2.71)). Within this perspective, the most popular and successful correlation was developed by Sato et al. [134, 139] and it was already shown in Section 2.4.2 (Eq. (2.72)). The linear combinability of the shear-induced and bubble induced turbulence has been already experimentally confirmed for systems with low gas fraction [140], while its suitability for less dilute systems

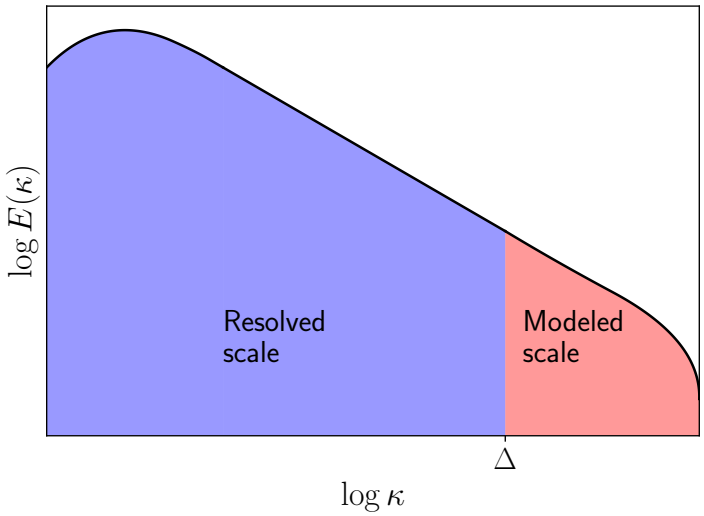

Figure 2.13: Choice of Δ in LES simulation: at least 80% of turbulent kinetic energy field should be resolved.

is still matter of discussion. Moreover, the Sato model neglects non-linear effects such as the stretching of vortices and the related deformation of the close bubbles, which may have an impact on the interfacial momentum mass terms like the drag force [44]. Nevertheless, this method is still widely used in Euler-Euler modeling of bubble columns, although its relevance depends on the specific simulated case [10]. A more refined approach relies on the inclusion of the BIT effects as source terms the turbulence transport equations, in particular for k and ϵ for the liquid phase in RANS simulations. Accordingly, one- [141] and two-equations [43, 142] models were proposed to include the extra terms related to the BIT effects. The principal assumption of these models is that the major contribute to the generation of interfacial turbulent energy is due to the momentum exchange involved by the drag force. Therefore, the source term for the turbulent kinetic energy is written as

$$S_{k,l}^{BIT} = \boldsymbol{F}_D \cdot |\boldsymbol{u}_g - \boldsymbol{u}_l| \,. \tag{2.75}$$

In two-equations models, the source term for the liquid turbulence dissipation rate is often calculated from $S_{k,l}^{BIT}$ as

$$S_{\epsilon,l}^{BIT} = C_{\epsilon,BIT} \frac{S_{k,l}^{BIT}}{\tau}, \tag{2.76}$$

with $C_{\epsilon,BIT}$ and τ being respectively a fitting constant and a time scale whose choice may be different according to the authors [43, 143–145]. However, as aforementioned, these models are mostly suited for RANS simulations, where the k-ϵ is the most direct approach; in LES simulations BIT effects are usually accounted for

using Eq. (2.72). In this regard, recent studies [44] highlighted that the impact of BIT effects in the simulations might sensibly improve with the inclusion of bubbles polydispersity and an accurate near wall modeling.

2.5 Population balance modeling

The Eulerian formulations have one serious lack: the size of the dispersed phase, i.e. the bubble diameter, must be fixed constantly throughout the simulation. Although this approximation could be still valid in the homogeneous regime, surely it does not correspond to the reality in the heterogeneous regime, where the bubble size distribution is wider due to higher gas velocity. Therefore, the interfacial area, mass transfer coefficient and gas hold-up predicted by the simulations might be considerably different from the experimental measurements. An estimation of the bubble diameter distribution, especially at high gas velocity, thus seems essential to properly model the flow.
A common way to overcome this limitation of the Eulerian descriptions is to solve one or more population balance equations coupled with the fluid dynamics equations, for the estimation of the bubble size distribution [146, 147]. For this purpose, the population balance models (PBM) rely on the solution of the transport equation for the bubbles number density function (NDF), $n(\boldsymbol{x}, \boldsymbol{\xi})$. The NDF is a function of the external coordinates $\boldsymbol{x} = (x, y, z, t)$, i.e. the physical space coordinates, and the internal coordinates $\boldsymbol{\xi} = (\xi_1, \ldots, \xi_N)$, which are related to specific properties of the dispersed phase such as the size or the temperature [147]. The population balance is monovariate if there is only one internal coordinate, usually corresponding to the bubble diameter ($\boldsymbol{\xi} \equiv L$)[1] or multivariate if $\boldsymbol{\xi}$ is a vector of two or more components, such as the specific bubble velocity, the temperature or the chemical composition, in addition to the diameter. The density function is defined in such a way that $n(\boldsymbol{x}, \boldsymbol{\xi}) d\boldsymbol{x} d\boldsymbol{\xi}$ is the number of particles located in volume $d\boldsymbol{x}$ and with internal coordinates inside the range $d\boldsymbol{\xi}$.
The equation for $n(\boldsymbol{x}, \boldsymbol{\xi})$ takes into account the variation of the number of bubbles in the control volume due to both continuous and discrete events, the former corresponding to the bubbles carried by the net fluid flow in the control volume and the latter to coalescence or breakage phenomena:

[1] In this chapter bubble diameter and bubble size are used as synonyms and denoted with L in the sake of simplicity.

$$\frac{\partial}{\partial t}\left(\int_{V_x} d\boldsymbol{x}\int_{V_\xi} d\boldsymbol{\xi} n\right)+\int_{V_\xi} d\boldsymbol{\xi}\int_{V_x}(n\boldsymbol{u})\cdot d\boldsymbol{A}_x+\int_{V_x} d\boldsymbol{x}\int_{V_\xi}(n\dot{\boldsymbol{\xi}})\cdot d\boldsymbol{A}_\xi = \\ =\int_{V_x} d\boldsymbol{x}\int_{V_\xi} d\boldsymbol{\xi} S_\xi \quad (2.77)$$

where V_x and V_ξ are respectively the volume control of the external and internal coordinates, $\boldsymbol{A}_x$ and $\boldsymbol{A}_\xi$ are the relative surface vectors, $\boldsymbol{u}$ and $\dot{\boldsymbol{\xi}}$ are the rate of change of the external (i.e. velocity) and internal coordinates, and, finally S_ξ is the source term that accounts the discontinuous events involving bubbles depending on the internal coordinates $\boldsymbol{\xi}$.
Applying the Reynolds-Gauss theorem to Eq. (2.77) and assuming that it must be valid for any chosen control volume:

$$\frac{\partial n}{\partial t}+\nabla_x\cdot(\boldsymbol{u}n)+\nabla_\xi\cdot\left(\dot{\boldsymbol{\xi}}n\right)=S_\xi \quad (2.78)$$

In flows where the temperature is uniform and the gas bubbles have constant chemical composition, the dependence of the NDF on these internal coordinates may be neglected. If the bubbles have their own velocity distribution, $\boldsymbol{\xi}$ contains, in addition to the bubble size L, the corresponding velocity as well, and Eq. (2.78) is known as General Population Balance Equation (GPBE). However, under the assumption that bubble velocity does not depend on its size and it is hence equal to the velocity calculated through the Navier-Stokes equations, the NDF solely depends on the bubble size and the Population Balance Equation (PBE) is obtained:

$$\frac{\partial}{\partial t}n(L)+\nabla\cdot(\boldsymbol{u}_g n(L))+\frac{\partial}{\partial L}\left(\dot{L}n(L)\right)=S(L) \quad (2.79)$$

with $\dot{L}$ being the rate of change of the bubble size due to the mass transfer, which is neglected in this work.
The source term $S(L)$ accounts for the discontinuous events affecting the bubbles size. These events may be mainly categorized in three groups, according to their order [147]:

- zero-order events. They depend solely on the continuous phase flow properties, such as the nucleation of bubbles in boiling or cavitation. They are not considered in this study;
- first-order events. They involve only one bubble and originate from its interaction with the liquid phase. Breakage is a first-order event;
- second-order events. In these events two bubbles and their interaction with the surrounding liquid are involved. Coalescence is a second-order event.

Moreover, $S(L)$ may be split in four terms [148], accounting for the birth and death, due to both coalescence and breakage, of bubbles of size L:

$$S(L) = B^C(L) - D^C(L) + B^B(L) - D^B(L) \tag{2.80}$$

- $B^C(L)$ and $D^C(L)$ are the terms modeling the birth and death due to the coalescence:

$$B^C(L) = \frac{L^2}{2} \int_0^\infty h\left(\left(L^3 - \lambda^3\right)^{1/3}, \lambda\right) n\left(\left(L^3 - \lambda^3\right)^{1/3}\right) n(\lambda) d\lambda, \tag{2.81}$$

$$D^C(L) = \int_0^\infty h(L, \lambda) n(L) n(\lambda) d\lambda, \tag{2.82}$$

  where $h(L, \lambda)$ is the kernel modeling the coalescence of two bubbles of size L and λ;

- $B^B(L)$ and $D^B(L)$ are the terms modeling the birth and death due to the breakage:

$$B^B(L) \int_L^\infty \beta(L, \lambda) g(\lambda) n(\lambda) d\lambda, \tag{2.83}$$

$$D^B(L) = g(L) n(L), \tag{2.84}$$

  with $g(L)$ denoting the break-up frequency of a bubble of size L and $\beta(L, \lambda)$ is the daughter size distribution originated from the breakage of one mother bubble of size λ.

2.5.1 Breakage kernels

As aforementioned, the breakage event of a bubble depends on the characteristics of the flow of the liquid in the close neighborhood, which causes the bubble deformation and, eventually, if the external stress overcomes the bubble resistance, the break-up. In particular, bubble breakage can mainly occur as a consequence of four possible mechanisms [149, 150]:

- turbulence fluctuations. It is the most frequent breakage mechanism in industrial bubble columns. The liquid velocity fluctuations around the bubble cause bubble deformation and elongation until break-up takes place. In particular, it is assumed that only the eddies belonging to the inertial subrange contribute to the phenomenon, since the larger eddies only participate with convective motion and smaller eddies do not have enough energy;

- macroscopic shear stress. It is mainly related to large bubbles. It is caused by a local steep velocity gradient in the liquid flow that deforms and breaks the bubble in daughters of similar size;

- turbulent shear stress. It is relevant when the size of the bubbles is comparable with the Kolmogorov length scale. In this mechanism, the bubble is sheared-off by local microscopic velocity gradients in the turbulent eddies;
- interfacial instabilities. Caused by Rayleigh-Taylor and Kelvin–Helmholtz instabilities.

Given its industrial relevance, only the turbulence fluctuations breakage mechanism is considered in this work.
Under the assumptions of homogeneous and isotropic turbulence and of bubble size belonging to the inertial subrange, four main criteria to activate break-up have been individuated in the literature, as detailed below.

a) Turbulent kinetic energy of the bubble larger than a critical value

The first pioneering model for break-up was proposed by Coulaloglou and Tavlarides for liquid-liquid dispersions [151]. They assumed that break-up occurs if the kinetic energy transmitted to the bubble by hitting eddies is larger than its surface energy, with the additional hypothesis of a normal distribution of the kinetic energy. The break-up rate is:

$$g(L) = C_1 L^{-2/3} \epsilon^{1/3} \exp\left[-\frac{C_2 \gamma}{\rho_d \epsilon^{2/3} L^{5/3}}\right], \tag{2.85}$$

where ρ_d is density of the dispersed phase and γ the interfacial tension.
The authors also proposed a correction for the damping effects on the turbulent intensity at high gas fraction

$$g(L) = C_3 L^{-2/3} \frac{\epsilon^{1/3}}{1+\alpha_d} \exp\left[-\frac{C_4 \gamma (1+\alpha_d)^2}{\rho_d \epsilon^{2/3} L^{5/3}}\right]. \tag{2.86}$$

Lasheras et al. [152] adapted this model to gas-liquid dispersion replacing the dispersed phase density with the continuous phase density, since Eq. (2.85) and Eq. (2.86) considerably underpredict the breakage rate if applied to such systems:

$$g(L) = C_1 L^{-2/3} \epsilon^{1/3} \exp\left[-\frac{C_2 \gamma}{\rho_l \epsilon^{2/3} L^{5/3}}\right]. \tag{2.87}$$

$$g(L) = C_3 L^{-2/3} \frac{\epsilon^{1/3}}{1+\alpha_d} \exp\left[-\frac{C_4 \gamma (1+\alpha_d)^2}{\rho_l \epsilon^{2/3} L^{5/3}}\right]. \tag{2.88}$$

b) Velocity fluctuations around the bubble larger than a critical value

Narsimhan et al. [153] proposed a stochastic formulation of the breakage frequency for liquid droplets in liquid media, assuming that it is caused by the collisions of eddies of different scales, that can be described as a Poisson process.

Alopaeus et al. [154] adjusted this model including the dependency of the eddy-droplet collision frequency on the turbulent dissipation rate and the effect of the fluid particle viscous stresses:

$$g(L) = C_7 \epsilon^{1/3} \text{erfc} \sqrt{C_8 \frac{\gamma}{\rho_l \epsilon^{2/3} L^{5/3}} + C_9 \frac{\mu_g}{\sqrt{\rho_l \rho_g} \epsilon^{1/3} L^{4/3}}} \tag{2.89}$$

Lakkonnen et al. [155], pointed out that for gas-liquid dispersions the viscous stresses in the fluid particles are negligible and applied Eq. (2.89) to bubbly flows substituting μ_g with μ_l:

$$g(L) = C_7 \epsilon^{1/3} \text{erfc} \sqrt{C_8 \frac{\gamma}{\rho_l \epsilon^{2/3} L^{5/3}} + C_9 \frac{\mu_l}{\sqrt{\rho_l \rho_g} \epsilon^{1/3} L^{4/3}}} \tag{2.90}$$

c) Turbulent kinetic energy of the hitting eddy larger than a critical value

One of the most popular model belonging to this criterion was proposed by Prince and Blanch [156], who proposed an analogy of the interaction eddy-bubble with collisions in ideal gases. As in the collision kernels (Section 2.5.3), they suggested to calculate the breakage frequency as the product of the frequency $h_e(L, L_e)$ and efficiency $\eta_e(L, L_e)$ of the collision between a bubble of size L and a turbulent eddy of size L_e:

$$g(L) = \int_0^\infty h_e(L, L_e) \eta_e(L, L_e) dL_e. \tag{2.91}$$

They assumed $h_e(L, L_e)$ proportional to the relative velocity between eddies and bubbles and $\eta_e(L, L_e)$ equal to the probability that the hitting eddy has enough energy to break the bubble. The minimum energy is deduced from the critical Weber number We_{cr}, estimated equal to 2.3. The final expression for $g(L)$ is:

$$g(L) = \int_{\kappa_{\min}}^{\kappa_{\max}} \frac{0.14\pi}{0.16} \left(L + \frac{2}{\kappa}\right)^2 \left(L^{2/3} + \left(\frac{2}{\kappa}\right)^{2/3}\right)^{1/2} \epsilon^{1/3} \exp\left[-\frac{1.18}{2^{2/3}} \frac{\gamma \kappa^{2/3}}{\rho_l L \epsilon^{2/3}}\right] \kappa^2 d\kappa \tag{2.92}$$

with $\kappa = 2/L_e$.

Luo and Svendsen presented a similar model [157] based on the kinetic gas theory, including also the daughter size distribution in the breakage frequency. This breakage kernel assumes that the minimum energy corresponds to the increase in the surface energy during the disruption, $E_b(L)$. Moreover, it does not require any additional or empirical constant:

$$g(L) = \int_0^{0.5} g(L, \lambda) d(L/\lambda), \tag{2.93}$$

$$h_e(L, \lambda) = 0.93(1 - \alpha_d) \left(\frac{\epsilon}{L^2}\right)^{1/3} \int_{\xi_{\min}}^1 \frac{(1+\xi)^2}{\xi^{11/3}} \exp\left[-\frac{E_b(L)}{E(L_e)}\right] d\xi, \tag{2.94}$$

where $E(L_e)$ is the energy of the hitting eddy, $\xi_{\min} = L_{e,\min}/L$ and $L_{e,\min}$ is the minimum size of the eddies that can contribute to the break-up .

d) Inertial force of the hitting eddy greater than the interfacial force of the smallest daughter particle

In this category, the most relevant model was proposed by Lehr et al. [158] who followed a similar approach to Luo and Svendsen. The expression of the breakage frequency relies on the balance of the interfacial forces between the hitting eddy and the smaller daughter value and its final formulation is:

$$g(L) = 0.5\frac{L^{5/3}\epsilon^{19/15}\rho_l^{7/5}}{\gamma^{7/5}}\exp\left[-\frac{\sqrt{2}\gamma^{9/5}}{L^3\rho_l^{9/5}\epsilon^{6/5}}\right] \tag{2.95}$$

2.5.2 Daughter size distribution

The distribution of the size of the two or more bubbles generated by the breakage of one mother bubble is called daughter size distribution (DSD). The DSD may be either empirical, phenomenological or statistical [150]. Empirical DSD are valid only for the specific operating conditions for which they were developed and therefore they cannot be used in other cases. Phenomenological models rely on the Kolmogorov description of turbulence and they are usually classified according to shape of the DSD function, which can be bell-shaped [159], U-shaped [160] or M-shaped. The DSD derived by Lehr et al. [158] belongs to the latter category and presupposes binary breakage:

$$\beta(L,\lambda) = \frac{9L^2}{\sqrt{\pi}\lambda^3}\frac{\exp\left[\frac{9}{4}\left[\log\left[\frac{2^{2/5}L\rho_l^{3/5}\epsilon^{2/5}}{\gamma^{3/5}}\right]\right]^2\right]}{1+\operatorname{erfc}\left[\frac{3}{2}\log\left[\frac{2^{15}\lambda\rho_l^{3/5}\epsilon^{2/5}}{\gamma^{3/5}}\right]\right]}, \tag{2.96}$$

where λ denotes the size of the mother bubble and L of the larger among the two daughter bubbles.
Among the statistical models, the most popular was proposed by Laakkonen et al. [155, 161] using a beta function:

$$\beta(L,\lambda) = \frac{1}{2}(C+1)(C+2)(C+3)(C+4)\left(\frac{L^2}{\lambda^3}\right)\left(\frac{L^3}{\lambda^3}\right)^2\left(1-\frac{L^3}{\lambda^3}\right)^C \tag{2.97}$$

if only binary breakage is considered, $C = 2$ and Eq. (2.97) becomes:

$$\beta(L,\lambda) = 180\left(\frac{L^2}{\lambda^3}\right)\left(\frac{L^3}{\lambda^3}\right)^2\left(1-\frac{L^3}{\lambda^3}\right)^2 \tag{2.98}$$

2.5.3 Coalescence kernels

In contrast to breakage, coalescence is a more complex phenomenon since it involves the mutual interactions between two bubbles and the surrounding fluid [162]. In this perspective, a coalescence event can be decomposed in two parts, each one due to a different interaction:

- bubbles collision. It is the first step in the coalescence process and it occurs due to the interaction between the bubbles and the surrounding liquid, whose flow field leads, through different mechanisms, to the bubbles encounter. It is modeled through the collision frequency function, $h_0(L_1, L_2)$;
- bubbles interaction. Not every collision leads to coalescence, since the bubbles, after colliding, may bounce and leave apart: thus, a collision efficiency is introduced $\eta(L_1, L_2)$.

The final coalescence kernel is the product between the collision frequency and efficiency:

$$h(L_1, L_2) = h_0(L_1, L_2)\eta(L_1, L_2). \tag{2.99}$$

Collision frequency

a) Collisions due to turbulent fluctuations The most frequent mechanism of collision is due to the turbulent fluctuations, where the chaotic motion of the turbulent eddies of the inertial subrange leads two bubble to collision. In this scenario, bubbles are modeled as gas molecules in the gas kinetic theory [150]. As for the breakage frequency due to turbulent fluctuations, the collision frequency may be seen as proportional to the volume swept by the bubbles in the time unit and, therefore, it may be expressed as the product of the collision-sectional area $S(L_1, L_2)$ and the bubbles relative velocity $u_{\text{rel}}(L_1, L_2)$:

$$h_0(L_1, L_2) = S(L_1, L_2)u_{\text{rel}}(L_1, L_2). \tag{2.100}$$

Assuming that the bubbles have spherical shape, the collision cross section is

$$S(L_1, L_2) = \frac{\pi}{4}(L_1 + L_2)^2 \tag{2.101}$$

The relative velocity may be estimated considering that the bubbles have the velocity of turbulent eddies of the same size and belonging to the inertial subrange [151, 156]:

$$u_{\text{rel}}(L_1, L_2) = \sqrt{u_{e,1}^2 + u_{e,2}^2}. \tag{2.102}$$

If the turbulence is isotropic and homogeneous and therefore the Komolgorov description can be applied [109], the eddy velocity u_e can be calculated as

$$u_e^2 = 2\epsilon^{2/3}L_e^{2/3}, \tag{2.103}$$

Eq. (2.102) thus becomes:

$$u_{\text{rel}}(L_1, L_2) = \sqrt{2}\epsilon^{1/3}\sqrt{L_1^{2/3} + L_2^{2/3}}. \tag{2.104}$$

Therefore the collision frequency (Eq. (2.100)) may be eventually written as:

$$h_0(L_1, L_2) = \frac{\sqrt{2}\pi}{4}(L_1 + L_2)^2\epsilon^{1/3}\sqrt{L_1^{2/3} + L_2^{2/3}}. \tag{2.105}$$

Prince and Blanch [156] substituted $\frac{\sqrt{2}\pi}{4}$ with a constant C_1 ranging from 0.28 to 1.11 according to the investigated system:

$$h_0(L_1, L_2) = C_1(L_1 + L_2)^2\epsilon^{1/3}\sqrt{L_1^{2/3} + L_2^{2/3}}. \tag{2.106}$$

Eq. (2.106) was later adjusted by introducing two new parameters, Θ and Λ, taking into account respectively the possible presence of other bubbles in the colliding path and the ratio between the mean distance between two bubbles and their effective turbulent path [150]. Several expressions have been proposed for Θ:

- Wu et al. [163]:

$$\Theta = \frac{1}{\alpha_{g,\max}^{1/3}\left(\alpha_{g,\max}^{1/3} - \alpha_g^{1/3}\right)}, \tag{2.107}$$

  with $\alpha_{g,\max}$ corresponding to the maximum gas volume fraction for bubbles dispersed in water, set equal to 0.8;

- Wang et al. [164, 165]:

$$\Theta = \frac{\alpha_{g,\max}}{\alpha_{g,\max} - \alpha_g}, \tag{2.108}$$

- Lehr et al. [158]:

$$\Theta = \exp\left[-\left(\frac{\alpha_{g,\max}^{1/3} - \alpha_g^{1/3}}{\alpha_g}\right)^2\right], \tag{2.109}$$

  with $\alpha_{g,\max}$ =0.6.

Similarly, many correlations for Λ are available in the literature, the most relevant were developed by Wu et al. [163] and Wang et al. [164, 165]. The former is:

$$\Lambda = 1 - \exp\left[-C_\Lambda\frac{L_e}{H_{12}}\right] \approx 1 - \exp\left[-C_\Lambda\frac{\alpha_{g,\max}^{1/3}\alpha_g^{1/3}}{\alpha_{g,\max}^{1/3} - \alpha_g^{1/3}}\right], \tag{2.110}$$

where H_{12} is the mean distance between the two bubbles and C_λ a constant set equal to 3. The model proposed by Wang is similar:

$$\Lambda = \left(\exp\left[-\frac{H_{12}}{l_{12}}\right]\right), \tag{2.111}$$

where l_{12} is the mean turbulent path for the bubbles collision.
The conclusive expression for the collision frequency due to turbulent fluctuations according to Wang et al. [165] is then:

$$h_0(L_1, L_2) = C_2'\Theta\Lambda(L_1 + L_2)^2\epsilon^{1/3}\sqrt{L_1^{2/3} + L_2^{2/3}}. \tag{2.112}$$

b) Collisions due to other mechanisms However, bubbles can collide due to other mechanisms involving eddy capture, macroscopic velocity gradient, buoyancy and wake entrainment [162] and, therefore, appropriate collision frequency functions have been developed for describing them [166, 167].
Wang et al. [165] modeled the global coalescence kernel due to the wake entrainment as follows:

$$h(L_1, L_2) = 15.4\Xi L_1^2 u_{\text{slip},1} \exp\left[-0.46\rho_l^{1/2}\epsilon^{1/3}\gamma^{-1/2}\left(\frac{L_1 L_2}{L_1 + L_2}\right)^{5/6}\right] \tag{2.113}$$

with

$$u_{\text{slip},1} = 0.71\sqrt{gL_1}, \tag{2.114}$$

$$\Xi = \begin{cases} \frac{\left(\frac{L_2 - L_c}{2}\right)^6}{\left[\left(\frac{L_2 - L_c}{2}\right)^6 + \left(\frac{L_c}{2}\right)^6\right]} & L_2 \geq L_c/2 \\ 0 & \text{otherwise} \end{cases} \tag{2.115}$$

and

$$L_c = 4\sqrt{\frac{\gamma}{g\left(\rho_l - \rho_g\right)}}. \tag{2.116}$$

Moreover, Prince and Blanch modeled other mechanisms of bubble collisions, such as the ones due to buoyancy and shear rate in the liquid velocity field [156]. The former is expressed by

$$h_0(L_1, L_2) = 0.25\pi\left(L_1 + L_2\right)^2\left|u_{b,1}b - u_{b,2}\right| \tag{2.117}$$

where u_b is the bubble rise velocity:

$$u_b = \left(\frac{2.14\gamma}{\rho_l L} + 0.505gL\right)^{0.5}. \tag{2.118}$$

On the other hand, they modeled the collision efficiency due to shear rate effects as:

$$h_0(L_1, L_2) = \frac{1}{6}(L_1 + L_2)^3\overline{\frac{du_l}{dR}}, \tag{2.119}$$

with $\overline{\frac{du_l}{dR}}$ being the average shear rate of the liquid velocity and it can be computed in accordance with Walters and Blanch [168].

Collision efficiency

Three main approaches have been developed for the modeling of the collision efficacy, due to the interaction between the colliding bubbles.

a) Energy approach. The efficacy is related to the ratio of the interfacial energy E_γ and the collision kinetic energy E_k [169]:

$$\eta(L_1, L_2) = \exp\left[-C\frac{E_\gamma}{E_k}\right], \tag{2.120}$$

where C is a proportional constant. Sovová [169] suggested the following expression:

$$\eta(L_1, L_2) = \exp\left[-C_{\text{sov}}\frac{\gamma(V_1^{2/3} + V_2^{2/3})(V_1 + V_2)}{\rho_l \epsilon^{2/3} V_1 V_2 (V_1^{11/9} + V_2^{11/9})}\right], \tag{2.121}$$

with C_{sov} being a model constant.

b) Critical velocity approach. The outcome of the collision depends on the relative velocity of the bubbles along the direction perpendicular to the contact surface: coalescence occurs only if this value is smaller than a critical threshold u_{cr}. In accordance with experimental observations, Lehr et al. [158] suggested this expression:

$$\eta(L_1, L_2) = \min\left[\frac{u_{\text{cr}}}{u_{\text{rel}}}, 1\right], \tag{2.122}$$

where $u_{\text{cr}} = 0.08$ m/s for pure water-air systems and smaller for contaminated systems.

c) Film drainage approach. Following this approach, coalescence occurs only if the bubbles contact time is larger than the drainage time, i.e. the time interval necessary for the drainage of the liquid film trapped between the bubbles:

$$\eta(L_1, L_2) = \exp\left[-\frac{\tau_C}{\tau_D}\right]. \tag{2.123}$$

The drainage mechanism depends on the bubbles rigidity and the mobility of the interface: if the bubbles are small they can be assumed to behave like spherical rigid particles, while the presence of contaminants decreases the interface mobility [150]. Coulaloglou and Tavlarides [151] proposed the following expression for nondeformable bubbles with immobile interfaces

$$\eta(L_1, L_2) = \exp\left[-C_{CT}\frac{\mu_l \rho_l \epsilon}{\gamma^2}\left(\frac{L_1 L_2}{L_1 + L_2}\right)^4\right], \tag{2.124}$$

which was also adjusted for its application in case of high gas volume fraction:

$$\eta(L_1, L_2) = \exp\left[-C_{CT}\frac{\mu_l \rho_l \epsilon}{\gamma^2(1+\alpha_g)^3}\left(\frac{L_1 L_2}{L_1 + L_2}\right)^4\right], \tag{2.125}$$

It is worth noting that other expressions were developed for the coalescence efficiency following the time drainage approach [157, 164, 165], although Eq. (2.124) is the most used.

2.5.4 Quadrature Method of Moments

The different methods developed in the last decades to solve the PBE may be distinguished in three categories: class [170] and MUSIG [171] methods discretize the internal coordinate but they require considerable computational efforts, Monte Carlo methods [23] are based on stochastic differential equations and they are even more computationally demanding, methods of moments solve the transport equations of some moments of the NDF [46]. In this work the Quadrature Methods of Moments (QMOM) [172, 173] for univariate PBE is used and a brief description is given in this section. An extensive discussion of the subject can be found in the work by Marchisio and Fox [147].
As in the other moments based methods, in QMOM the PBE is not solved directly but, instead, the transport equations of low-order moments of the NDF are solved. The moment of order k respect to the only internal coordinate L is defined as

$$m_k = \int_0^\infty L^k n(L) dL \tag{2.126}$$

and the relative transport equation is

$$\frac{\partial \rho_g m_k}{\partial t} + \nabla \cdot (\rho_g \boldsymbol{u}_g m_k) = \rho_g S_k, \tag{2.127}$$

where S_k is the normalized source term related to the moment of order k. The moments defined in Eq. (2.126) are not only abstract mathematical entities, but they are linked to the characteristic of the bubble dispersion: m_0 is related to the number of bubbles per unit volume, m_2 and m_3 to the interfacial area and bubble volume through a shape factor respectively equal to π and $\pi/6$ for spherical bubbles. Moreover, the ratio of those moments corresponds to the Sauter mean diameter d_{32}, which is the diameter of a sphere with same volume-surface ratio:

$$d_{32} = \frac{m_3}{m_2}. \tag{2.128}$$

Eq. (2.127) generates a closure problem that must be overcome, since the source term depends on the NDF, which is unknown. With this aim, The QMOM uses a

Gaussian quadrature approximation of order N to estimate NDF with the following form:

$$n(L) \approx \sum_{i=1}^{N} w_i \delta(L - L_i), \tag{2.129}$$

where w_i and L_i indicate the weights and abscissas of the node i and δ the Dirac delta function. Applying the quadrature to Eq. (2.126)

$$m_k = \int_0^{\infty} L^k n(L) dL \approx \sum_{i=1}^{N} w_i L_i^k \tag{2.130}$$

Eq. (2.130) implies that first $2N$ moments must be known in order to calculate the N nodes and N weights needed for the Gaussian quadrature approximation in Eq. (2.129). With this aim, an inversion algorithm can be used [147].
After applying the quadrature approximation, the source term for the k-th moment may be written in a discretized form:

$$S_k \approx \frac{1}{2} \sum_{i=1}^{N} w_i \sum_{j=1}^{N} w_i h_{i,j} \left[(L_i^3 + L_j^3)^{k/3} - L_i^k - L_j^k \right] + \sum_{i=1}^{N} w_i g_i (\beta_i^k - L_i^k), \tag{2.131}$$

where $h_{i,j} = h(L_i, L_j)$, $g_i = g(L_i)$ and β_i^k is the moment of order k for the bubble size distribution relative to the daughter bubble of size L_i. If the expression proposed by Laakkoneen is used (Eq. (2.97)) an analytical formulation of β_i^k may be derived:

$$\beta_i^k = \frac{3240 L_i^k}{(k+9)(k+12)(k+15)} \tag{2.132}$$

Chapter 3

Mass transfer and slurry columns

In this chapter additional insights on particular aspects of the modeling of bubble columns are provided. In particular, in Section 3.1 a short overview of the modeling of the mass transfer phenomenon is given, focusing on the techniques to estimate the mass transfer coefficient, $k_l a_l$, from CFD simulations. In Section 3.2 the modeling of slurry bubble columns is analyzed and the main differences with the two-phase systems are highlighted.

3.1 Mass transfer modeling

Although a detailed description and modeling of the mass transfer phenomenon falls outside the aim of this work, an estimation of the mass transfer coefficient, $k_l a_l$ can be performed thanks to the CFD simulation. The assessment of this phenomenon is of crucial matter in modeling reactive systems, where the reactants and products transport between two or more phases is of pivotal interest for the performances of the whole process.
A common assumption is to consider the mass transfer between the liquid bulk and the bubbles interface as the limiting resistance because of the small diffusivity of the solute in the liquid phase and the small solubility of gaseous solutes in the liquid.
Therefore, the molecular flux of the species A can be written as

$$J_A = k_l a_l (\chi_A^* - \chi_A), \tag{3.1}$$

where k_l is the mass transfer coefficient, a_l is the interfacial area, χ_A^* is the molar concentration of A at the interface, which can be calculated through the Henry law if the concentration of A in the bulk of the gas phase is known, and χ_A is the concentration in the bulk of the liquid phase.

3.1.1 Estimation of k_l

Several studies have been performed for the estimation of the liquid side mass transfer coefficient k_l from the flow properties [174,175]. The basic approach is the two-film theory [176], that assumes the presence of stagnant films on both sides of the interface and, following the Fick law, estimated k_l as the ratio between the diffusivity and the film thickness. However, in bubble columns the mass transfer is an unsteady phenomenon and this description is not suitable.
Higbie's pioneering work [177] proposed the penetration theory for the evaluation of the mass transfer at the interfaces. According to Higbie's description, an element of fluid migrates toward the interface where it remains for a certain residence time, thus allowing the mass exchange with the gas phase. However, the residence time is short enough to not allow the transferred species to penetrate in the liquid bulk. Under the hypothesis of unsteady and laminar flow close to the interface, k_l may be expressed as:

$$k_l = \frac{2}{\sqrt{\pi}}\sqrt{\frac{\mathcal{D}_l u_{\text{slip}}}{d_b}}, \tag{3.2}$$

where $\mathcal{D}_l$ is the diffusivity coefficient in the liquid and u_{slip} is the bubble slip velocity. Danckwerts [178] further extended this theory, suggesting that the surface renewal period depends on the turbulence of the system. Lamont and Scott [179] proposed the idea that the mass transfer is controlled only be the renewal rate of small turbulence eddies and, in the framework of the Kolmogorov description of the turbulence, they derived:

$$k_l = 0.4\sqrt{\mathcal{D}_l\sqrt{\frac{\epsilon}{\nu_l}}}. \tag{3.3}$$

3.1.2 Estimation of a_l

In bubble columns, however, $k_l a_l$ is mainly dependent on the variation of a_l rather than k_l [180], thus a proper estimation of the interfacial area is fundamental for the proper modeling of the mass transfer.
As first approximation and with the assumption of spherical bubbles with uniform diameter, a_l can be estimated as

$$a_l = \frac{6\alpha_g}{d_b} \tag{3.4}$$

If coupled CFD-PBM simulations are performed, a_l can be estimated from the moments calculations taking into account the distribution of bubble size. Applying Eq. (2.126) for $k = 2$ it is possible to calculate the moment of order two:

$$m_2(\boldsymbol{x}) = \int_0^\infty L^2 n(L, \boldsymbol{x}) dL. \tag{3.5}$$

Recalling that $n(L, \boldsymbol{x})$ is a number density function and, therefore, $n(L, \boldsymbol{x})dL$ indicates the number of bubbles with size between L and $L + dL$ at the position $\boldsymbol{x}$, it is clear that $m_2(\boldsymbol{x})$ provides information on the bubbles interface area. Indeed, the two quantities are linked through the shape factor π:

$$a = \pi m_2. \tag{3.6}$$

In coupled CFD-PBM simulations the computation of interfacial area through Eq. (3.6) is particularly straightforward, being m_2 directly calculated throughout the domain.

3.2 Effect of the dispersed solid

As mentioned in Chapter 1 it is extremely common in the industrial practice the usage of three phase bubble columns, which contain solid particles in the liquid phase working as catalysts for a wide range of chemical reactions. The addition of solid particles significantly changes the fluid dynamics of the bubble columns and the interactions between the bubbles themselves, accordingly to the particles size and properties [4]:

- the global gas hold-up Φ decreases as the solid particles concentration and density increase [181–184], while the effect of the particles size seems to depend on their wettability [185], but there is no universal agreement on the mechanisms [186];
- the majority of authors agrees that small solid particles usually promote bubbles coalescence [56, 187, 188], thus leading to larger bubbles mean diameter and lower interfacial area. This can be explained assuming that the particles migrate mainly toward the bubble-liquid interface, reducing the drainage time and thus improving the collision efficacy;
- assuming that the only non-negligible resistance to mass transfer is at the liquid-gas interface, the effect of solid particles on the mass transfer coefficient $k_l a_l$ mainly depends on their impact on bubble coalescence: if the bubble diameter d_b decreases, $k_l a_l$ decreases as well due to the predominant effect of the interfacial area a_l, although k_l could also increase as a consequence of the enhanced refreshment rate of the liquid at the interface [189] and of the absorption/desorption and catalytic capability of the particles [190];
- it was found [191] that the presence of small (d_s =100 µm) hydrophilic particles causes a shift of the transition and heterogeneous regime at lower gas velocity (Fig. 3.1). Moreover, for $C_s \geq 5\%$, only the heterogeneous regime was detected, regardless of the gas velocity.

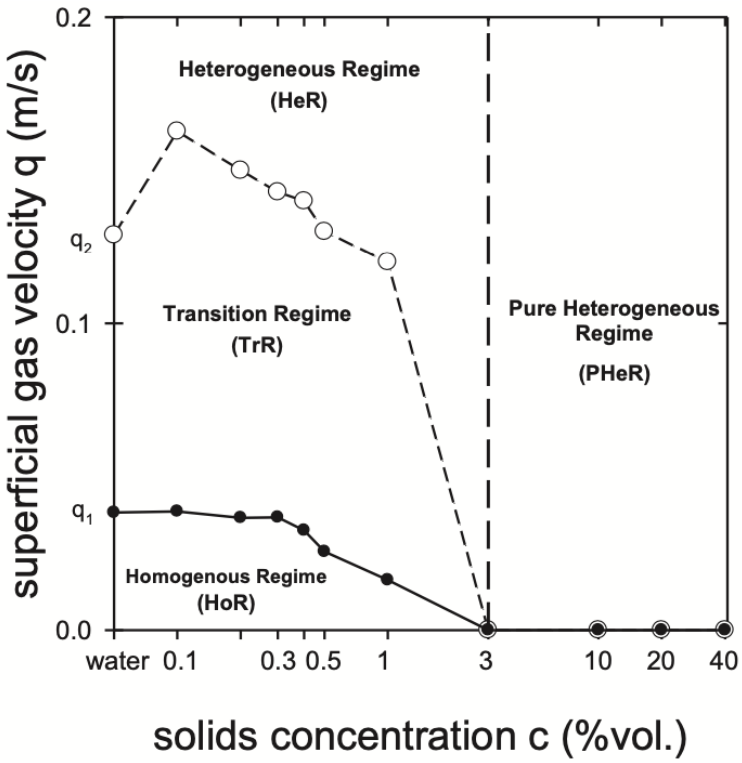

Figure 3.1: Flow regimes map in slurry bubble columns, extracted from [191].

However, these considerations are valid in the most common industrial operating conditions, i.e. particles diameter d_s between 10 and 2000 µm; for smaller particles at volume concentration $C_s \leq 6\%$ or larger particles at $C_s \geq 10\%$ the observed impact is opposite [9]: the interfacial area increases, the bubbles are smaller and, consequentially, the global gas hold-up is higher.

3.2.1 CFD modeling

There are two main approaches to include the presence of solid particles in the computational modeling of bubble columns, according to the particles inertia [192]:

- negligible particles inertia. This assumption is valid for small particles ($d_s \leq 100$ µm) which follow the liquid streamlines. In this case, the mixture liquid-solid may be approximated as a single pseudo-homogeneous slurry phase [104, 193];
- non-negligible particles inertia. This is the preferable framework in case of particles with $d_s > 100$ µm, since their own inertia can not be neglected. The solid particles are treated as a separate phase, therefore a proper selection

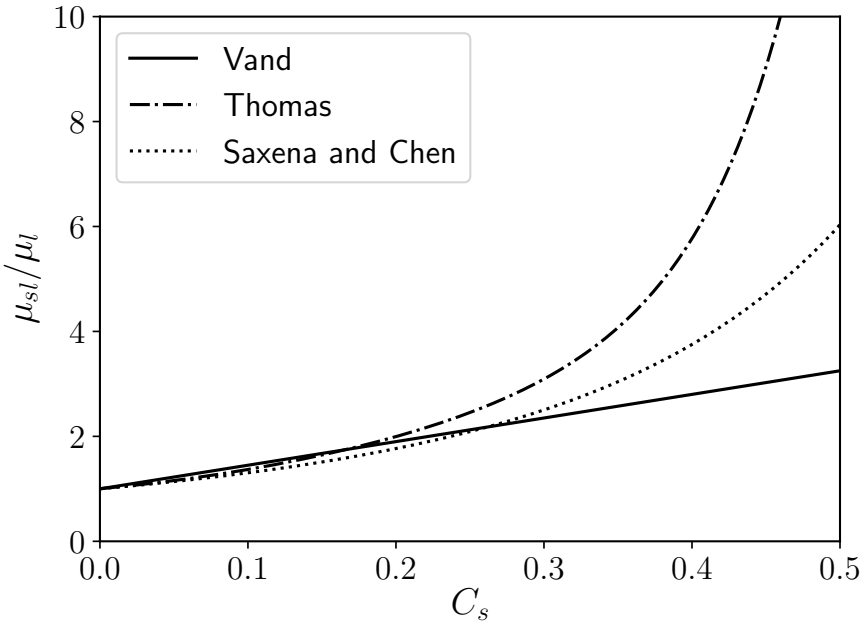

Figure 3.2: Slurry viscosity correlations: Vand et al. [197], Thomas et al. [198], Saxena and Chen [199].

of models to describe the gas-solid or liquid-gas or both interactions must be performed [57, 194, 195].

In most industrial applications catalytic particles are often micro or nanosized to maximize the interfacial area and the catalytic activity. Therefore, the pseudo-homogeneous phase approach allows to obtain a reliable model of the slurry bubble column with a low computational impact.

Following this approach, the density and viscosity of the slurry phase are calculated adjusting the liquid density and viscosity as functions of the solid concentration. In particular, the slurry density is calculated through a volume average of the liquid and solid viscosity [196]:

$$\rho_{sl} = C_s\rho_s + (1 - C_s)\rho_l \tag{3.7}$$

For the estimation of the slurry viscosity a number of correlations based on the Einstein equation for the viscosity of suspensions have been proposed [194] (Fig. 3.2):

- Vand et al. [197]:

$$\mu_{sl} = \mu_l \exp\left[\frac{2.5C_s}{1 - 0.609C_s}\right] \tag{3.8}$$

- Thomas [198]:

$$\mu_{sl} = \mu_l \left(1 + 2.5C_s + 10.05C_s^2 + 0.00273\exp[16.6C_s]\right) \tag{3.9}$$

- Saxena and Chen [199]:

$$\mu_{sl} = \mu_l(1 + 4.5C_s) \tag{3.10}$$

3.2.2 PBM modeling

The solid particles move mainly towards the bubbles interface and, necessarily, play an active role on the bubbles interactions, enhancing or hindering the coalescence and breakage phenomena. As pointed out by Mühlbauer et al. [192], in the recent literature the coupling of CFD simulations to slurry bubble columns to PBM, accounting for the impact of the solid particles on these phenomena, may be achieved with three different approaches:

- Adjusting of existing coalescence and breakage kernels through the introduction of fitting constants [200] or the combination of different kernels [59]. This approach is often aimed to reproduce the outcome of specific experimental measurements and lacks of universal applicability;

- Modifying the turbulence dissipation rate which is attenuated in dilute suspensions [201]. Troishko and Zdravistch [193] modeled this attenuation as a function of the volumic solid concentration:

$$\frac{\epsilon}{\epsilon_0} = \exp[-1.2846C_s] \tag{3.11}$$

- introducing a solid-effect multiplier β [56] which takes into account the enhancing effect of the solid particles on the coalescence efficiency by reducing the drainage time:

$$\eta(L_1, L_2) = \exp\left[-\frac{\beta\tau_C}{\tau_D}\right] \tag{3.12}$$

  The multiplier β was experimentally calculated and it is depicted in Fig. 3.3 as function of the solid loading.

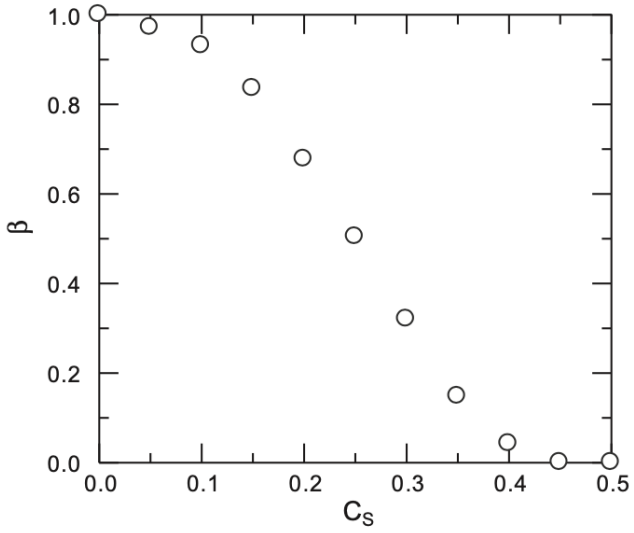

Figure 3.3: Solid-effect multiplier for the coalescence efficiency extracted from [56].

Chapter 4

Experimental set-ups

In this chapter the experimental set-ups used for the models validation are presented and briefly discussed. Four different systems were used: two circular columns and two square columns. The circular columns were used to validate the general features of the model such as blending, turbulence and population balance implementations. On the other hand, the experimental studies that adopted square columns focused on particular aspects such as the impact of solid particles and the mass transfer and, therefore, they contributed to the validation of the modeling of the specific phenomenon.

4.1 Gemello set-up

The first experimental set-up used in this work for validation is the one investigated by Gemello et al. [16, 41] and it is depicted in Fig. 4.1. It is a circular column with water and air respectively used as liquid and gas phases at room conditions and the operating details are summarized in Table 4.1. In particular the sparger consists in a perforated plate with 92 holes of 0.5 mm and, since the outer holes are not on the edge of plate, the effective diameter of the aerated region of sparger D_{in} was set to 0.38 m. The total height is 3.6 m and the initial liquid height is 1.6 m. The investigated gas superficial velocity ranged from 0 03 to 0.25 $\text{m}\,\text{s}^{-1}$, thus exploring both homogeneous and heterogeneous regimes. In the original experimental work, the effect of various degrees of contamination of the water on the hydrodynamics is analyzed as well, although in the present work only the results obtained with pure water are used for model validation.
The key aspect of this set-up is the abundance of local experimental measurements: radial profiles of gas fraction, liquid velocity and bubble diameter are provided at different locations of the columns and at various gas superficial velocity: this large amount of experimental values allows a solid validation of the computational models.

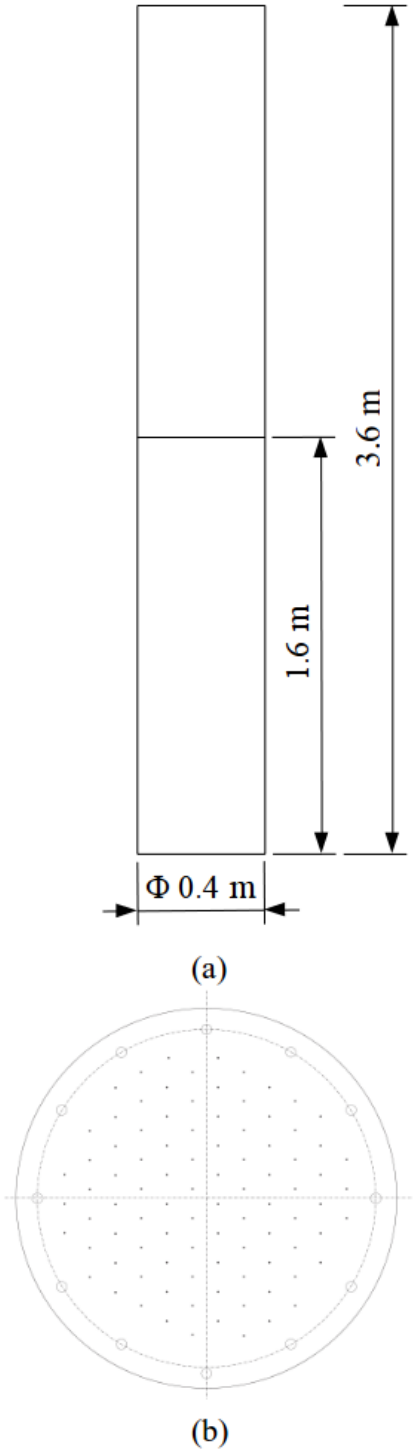

Figure 4.1: Experimental configuration of Gemello column. (a) Front view: the total height is 3.6 m, the initial liquid height is 1.6 m and the outer diameter of the column is 0.4 m. (b) Sparger view (extracted from [41]): the aerated area of the sparger is limited to a diameter of 0.38 m.

Property	Value	Units
D	0.4	m
H_t	3.6	m
H_0	1.6	m
D_{in}	0.38	m
μ_l	1.003	mPa s
ρ_l	998.2	kg m^{-3}
μ_g	0.0182	mPa s
γ	0.072	N m^{-1}
d_b	6.5	mm
U	0.03-0.09-0.16	m s^{-1}

Table 4.1: Details of Gemello set-up.

4.2 McClure set-up

A similar system was investigated by McClure et al. [29, 67] and its features are summarized in Table 4.2. The key feature of this study is the usage of three different spargers. In particular, two spargers with different hole size inject the gas symmetrically into the column, while in the third it is fed asymmetrically only through one half of the sparger. In this study the focus was is put on sparger #1 and sparger #3 (Fig. 4.2), where the hole size is equal to 0.5 mm and the only difference is the injection type, i.e. symmetrical or asymmetrical.
The asymmetric injection provided by sparger #3 results in a different distribution of the flow inside the column, because the gas mainly flows in the half of the column where it is injected. The features of this flows have many implications, especially on the investigation of the transversal interfacial forces such as the lift force, and, therefore, it could be used to assess their effective relevance.
Moreover, the experimental configuration has a truncated cone shape below the sparger. However, since this part of the domain has a negligible impact on the fluid dynamics of the gassed region, in the computational domain used for the simulations it is omitted. Therefore, only the part of the column above the sparger was simulated and is discussed in the following.
Another significant difference with the column studied by Gemello et al. is the aspect ratio, i.e. the ratio between the total height H_t and the diameter D, which, in this experimental set-up, is lower, resulting in a wider and smaller column.

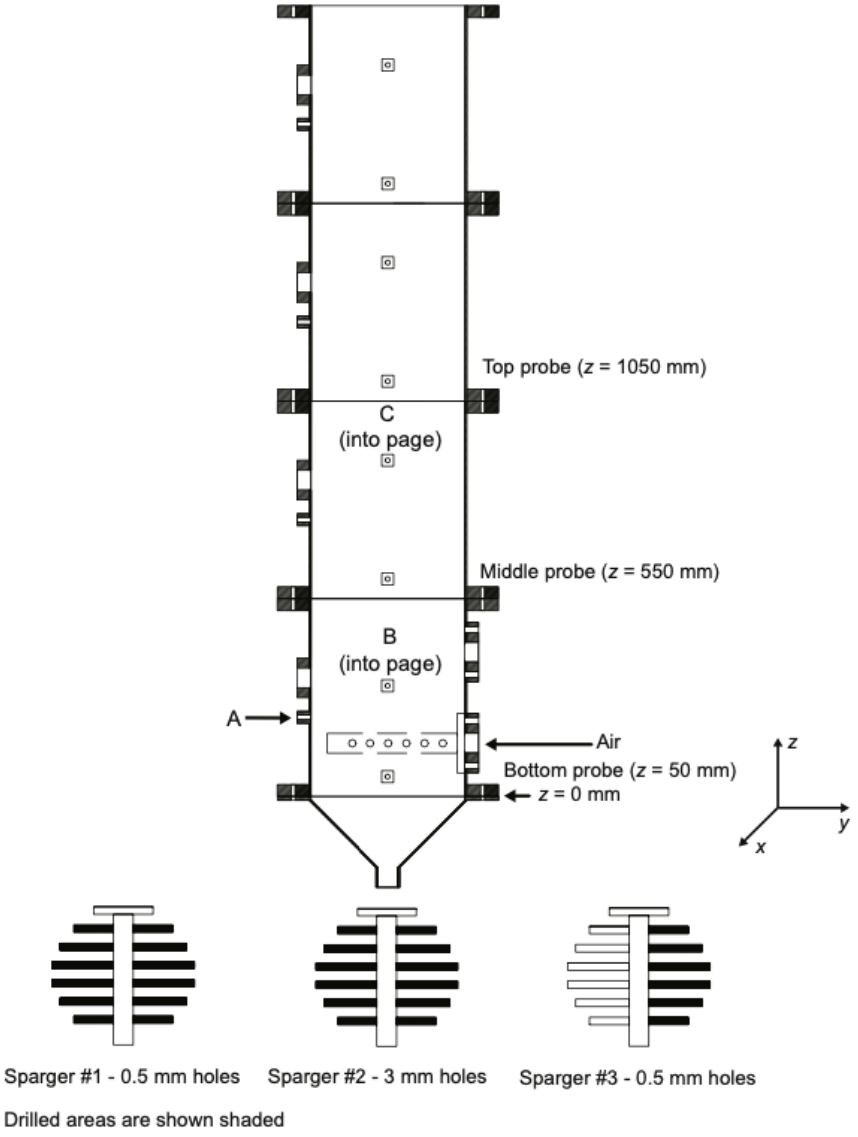

Figure 4.2: Experimental configuration of McClure column (extracted from [67]): the flow variables are sampled at the middle and top probe. Among the spargers used experimentally, the sparger #2 is not investigated in this study.

4.3 Ojima set-up

Unlikely the previously described systems, the one investigated by Ojima et al. [56] is not cylindrical but has a square cross section whose side (and hydraulic diameter) is equal to 0.2 m The column is depicted in Fig. 4.3 and the details are reported in Table 4.3.

Property	Value	Units
D	0.39	m
H_t	1.865	m
H_0	0.865	m
D_{in}	0.38	m
μ_l	1.003	mPa s
ρ_l	998.2	kg m^{-3}
μ_g	0.0182	mPa s
γ	0.072	N m^{-1}
d_b	7.5	mm
U	0.16 -0.25	m s^{-1}

Table 4.2: Details of McClure set-up.

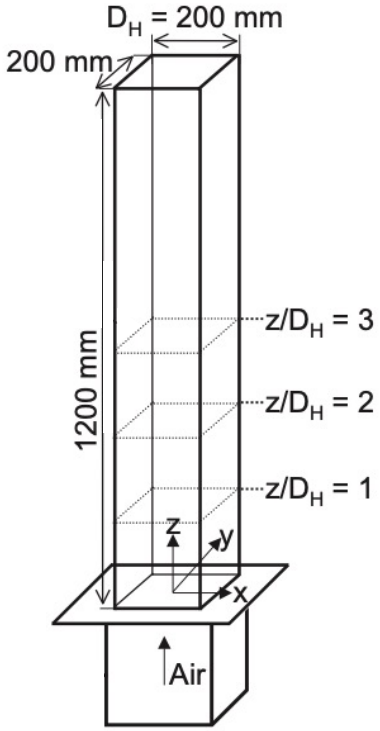

Figure 4.3: Experimental configuration of Ojima column (extracted from [56]). The total height of the column is 1.2 m, while the samplings are performed at $z/D_H =$ 1, 2 and 3.

Property	Value	Units
D_H	0.2	m
H_t	1.2	m
H_0	0.865	m
$D_{H,\text{in}}$	0.19	m
μ_l	1.003	mPa s
ρ_l	998.2	kg m^{-3}
μ_g	0.0182	mPa s
γ	0.072	N m^{-1}
d_s	100	µm
C_s	0 ÷ 0.50 %	-
ρ_s 2400		kg m^{-3}
U	0.02 -0.034	m s^{-1}

Table 4.3: Details of Ojima set-up.

The peculiarity of this study is that both two and three phase systems were investigated: air and water were used as gas and liquid phase and, furthermore, silica particles, with volumetric solid loading C_s ranging from 0 to 50%, were used as solid phase. The diameter of the used particles is equal to 100 µm, therefore their inertia is small enough to allow the usage of the pseudo-homogeneous slurry phase mentioned in Section 3.2.1.
Moreover, this is one of the few works on slurry bubble columns presenting local information of the volume gas fraction and bubble diameter, which are crucial for model validation. In fact, the experimental measurements of these local properties are particular challenging in slurry systems due to the cloudiness given to the presence of solid particles. Those difficulties increase as the solid concentration or the gas velocity increases and, therefore, the choice of experimental works for validating CFD models developed for slurry bubble columns is markedly arduous.

4.4 Kouzbour set-up

The last experimental work used in this study for model validation was performed by Kouzbour et al. [202, 203] using a square column having the same hydraulic diameter as the column investigated by Ojima: it is represented in Fig. 4.4 and further details are reported in Table 4.4.
Similarly to the work performed by Gemello, this study focused on the presence of contaminants of different kinds (such as cationic and anionic surfactants) in the liquid medium and their impact on the hydrodynamics of the column and, specifically, on the global gas hold-up and the mass transfer coefficient. In particular, this latter is experimentally measured with two oximeters placed at different heights

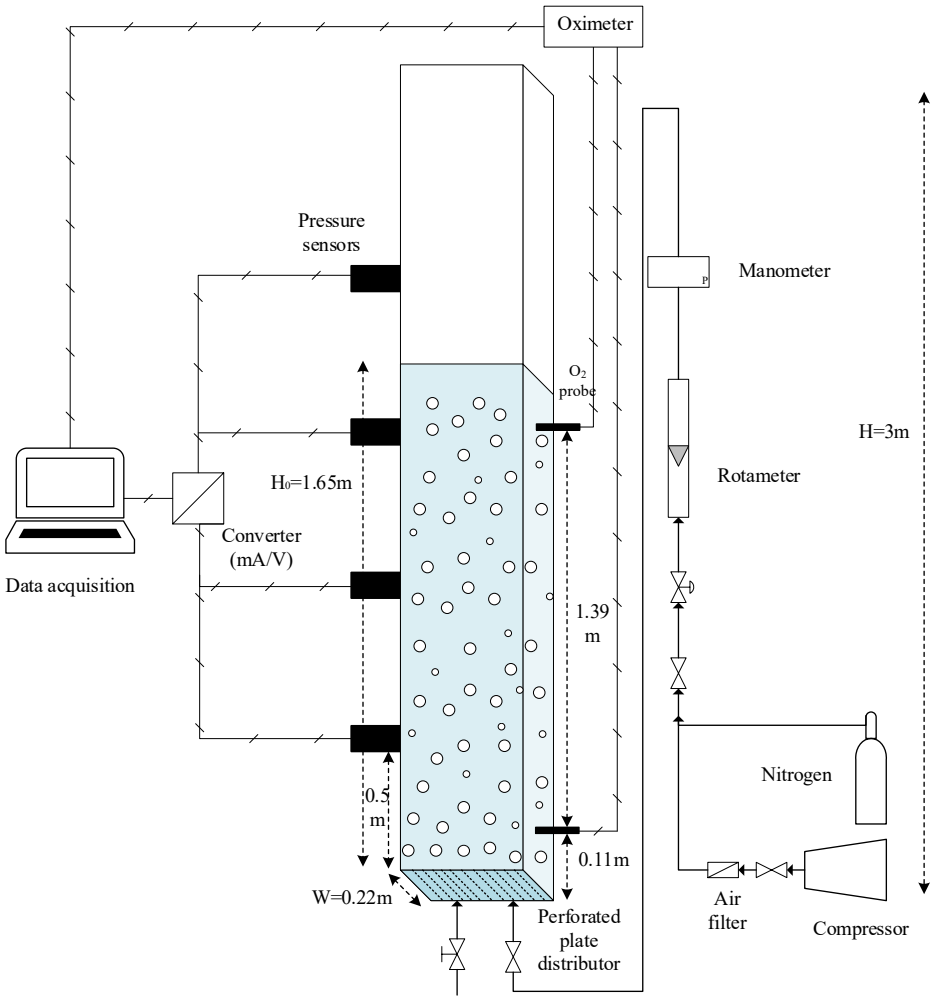

Figure 4.4: Experimental configuration of Kouzbour column (extracted from [202]). The gas hold-up is sampled with two sensors at $z = 0.5$ and 1.65 m (left side of the column in the picture) while the oxygen concentration is sampled at $z = 0.11$ and 1.5 m (right side of the column in the picture).

that measure the oxygen concentration in water with and without the presence of impurities. The corresponding mass transfer coefficient $k_l a_l$ is then calculated and referred to a standard temperature through an extrapolation.

Property	Value	Units
D_H	0.2	m
H_t	3.0	m
H_0	1.65	m
$D_{H,\text{in}}$		m
μ_l	1.003	mPa s
ρ_l	998.2	kg m^{-3}
μ_g	0.0182	mPa s
γ	0.072	N m^{-1}
U	$0.01 \div 0.09$	m s^{-1}

Table 4.4: Details of Kouzbour set-up. Liquid properties relate to uncontaminated water.

Chapter 5

Phase blending: analysis and applications

In this chapter[1] it is described the application of the Euler-Euler methodology in a RANS turbulence framework to simulate the cylindrical air-water bubble column investigated by Gemello et al. (Section 4.1) using the open-source CFD code `OpenFOAM`.
In particular the implementation of the so-called "blending approach", outlined in Section 2.3, is analyzed, with the aim of describing the regions of high gas content through its application. To the best of our knowledge, this approach has not yet exhaustively discussed in the scientific literature. The comparison of the results to numerical and experimental data available in the literature shows how the correct outcome may be achieved with a remarkable gain in computational speed and simulation robustness with respect to the usual method. The study was performed using a linear blending model, although the same conclusions might be drawn when the hyperbolic method is applied.

5.1 Introduction

As mentioned in Section 2.3, a fine blending implementation is crucial to take into account phase inversion and to achieve numerical stability in the simulation of dispersed multiphase systems. In this perspective, both air-in-water and water-in-air dispersions occur in bubble columns and are describable in `OpenFOAM` blending

[1]This chapter is mainly based on the conference proceeding [45]: F. Maniscalco, M. Shiea, A. Buffo, D. Marchisio, and M. Vanni, "Performance of the blending factor approach for modeling the interfacial forces in bubble columns operating at high gas hold up," in *Proceedings from the 14th International Conference on CFD in Oil & Gas, Metallurgical and Process Industries* (S. A. Press, ed.), pp. 64–71, 2020.

implementation.
However, in the description of bubble columns the most relevant case is the dispersion of air in water, therefore the usage of the relative blending factors f_1 will be discussed, being fundamental in the prediction of the fluid dynamical properties of interest (gas fraction, water and air velocity, etc). The evaluation of f_2, the blending factor for the dispersion of water and droplets in air, is relevant only at excessively high gas velocity, when phase inversion may occur locally, or in the head space: an accurate modeling of this part of the domain would require a convenient choice of α_{FD} and α_{PD} for the water phase, in addition to a proper selection of the drag law. Nevertheless, the main interest of this work is the modeling of the lower part of the domain, where the air is dispersed into water: the blending parameters and the interfacial laws for the upper part are selected in such a way to guarantee numerical stability. If blending were not implemented, the solver would treat the head space as if air were still the dispersed phase and water the continuous one, leading to serious convergence issues.

5.2 Computational set-up

Simulations were performed using `twoPhaseEulerFoam` solver by `OpenFOAM 5.0`. To simulate the system, experimentally investigated by Raimundo et al. [204] and Gemello et al. [16] whose details are summarized in Table 4.1, a grid of 45600 cells was generated (Fig. 5.1): approximately 20 cells are set along the diameter direction and each one of them is 3 cm high in the axial direction.
The simulation were carried out from time 0 to 180 s, being the presented results averaged from time 80 s to 180 s in order to discard the initial behavior, which is too sensitive to the starting condition. The investigated range of superficial gas velocity starts from 0.03 reaching 0.25 m s^{-1}, spacing thus from homogeneous to heterogeneous hydrodynamics regime. The fluids are air and water.
An adaptive time-step was used, as the maximum Courant number was set to 0.65. According to Gemello et al. [16] RNG k-ϵ guarantees the most accurate result for bubbly flows, but this turbulence model is unavailable in `twoPhaseEulerFoam`: therefore the standard k-ε was used for the continuous phase, being the dispersed phase treated as laminar. Simulations were performed using a fixed bubble diameter equal to 6.5 mm.
The drag coefficient C_D was calculated accordingly to Tomiyama correlation for partially contaminated air-water systems (Eq. (2.19)) and the swarm factor correction term h (Eq. (2.21)) proposed by Simonnet et al. (Eq. (2.24)). The usage of the swarm factor with the blending model is further discussed in Section 5.3.1. The other interfacial forces, described in Section 2.2.3, were not considered.
The inlet section was modeled as an homogeneous area with uniform properties, whose diameter was set to 0.38 m. The gas fraction was fixed equal to 0.5 and

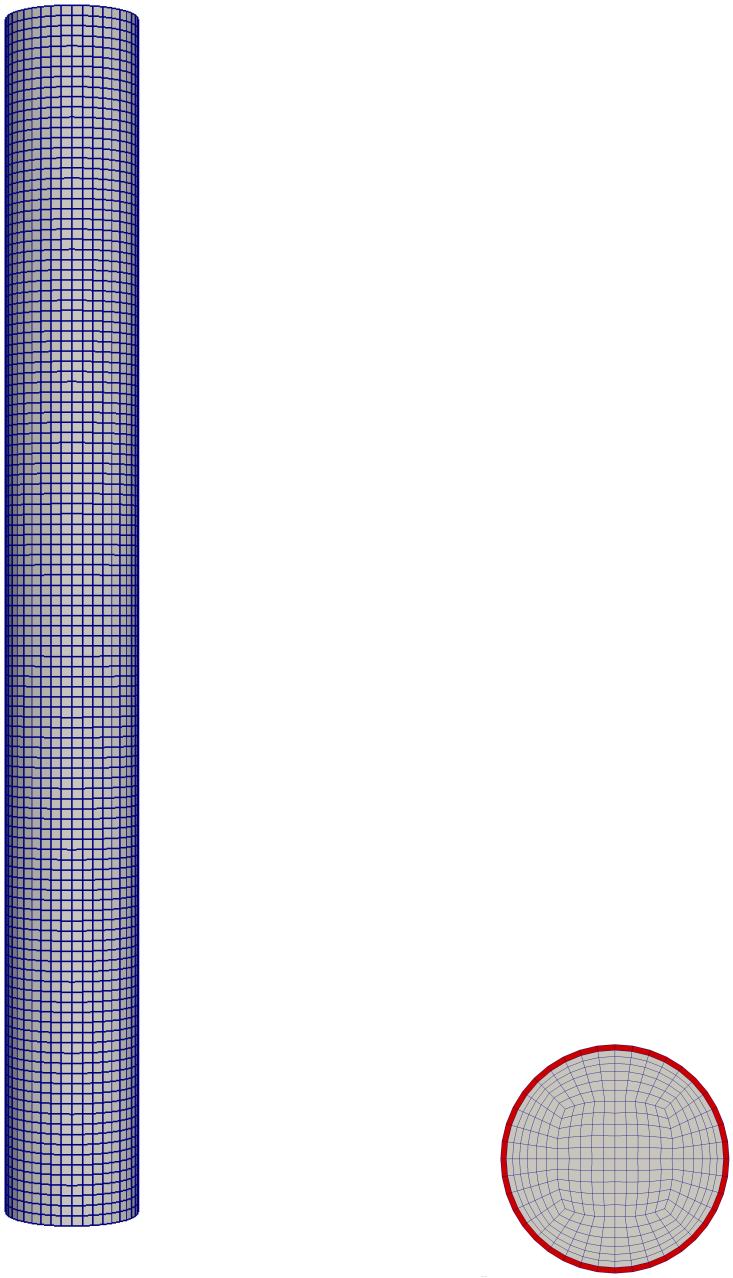

(a) (b)

Figure 5.1: Computational mesh used for RANS simulation of Gemello set-up: (a) side view, (b) bottom view. The red area is not included in the sparger.

the liquid z-velocity (as well x and y components for both phases) to 0. Air inlet z-velocity was accordingly set in such a way that the resultant superficial velocity

was equal to the desired value. The values of k and ϵ corresponded to turbulence intensity and viscosity ratio equal to 5 % and 10. At the top of the column a zero gradient condition was applied to all variables, with these conditions:

- gas fraction equal to 1 in case of backflow;
- `pressureInletOutletVelocity` for both gas and liquid velocities, which corresponds to the usual pressure outlet condition;
- `inletOutlet` for k and ϵ, which corresponds to a zero gradient condition with a user-defined value in case of backflow. These are set equivalently to a turbulence intensity equal to 0.01 % and turbulent length scale equal to the column diameter. The former two are typically `OpenFOAM` outlet conditions.

A standard wall function was used as wall condition for the turbulent variables, coupled with no-slip condition for the water velocity, slip condition for the air velocity and a zero gradient condition for the other variables.
The equations were spatially discretized using the Van Leer scheme [205], while the Crank-Nicolson scheme [206] was adopted for the time discretization.

5.3 Result and discussion

Experimental and simulation data here used for comparison are taken from Raimundo [204] and Gemello et al. [207]: in particular simulation results from the latter were computed using Ansys Fluent, RNG k-ϵ model for turbulence and setting h_0 equal to 0.15 in Eq. (2.27).

5.3.1 Use of swarm correction, h_0 and blending parameters

Swarm and blending factors are both multiplicative coefficients of the drag force term, although their physical meaning is significantly different: while the former takes into account the presence of a plurality of bubbles, the latter works as indicator of the continuous or dispersed phase.
In particular the limitation of the Simmonet's relation for swarm factor with the lower bound h_0 was proposed mainly for reasons of numerical stability: in some commercial solvers it is required the definition *a priori* of the dispersed and the continuous phases, which in systems such as bubble column reactors may cause instability when the air fraction overcomes the dispersed-continuous threshold. Eq. (2.24) approaches quickly to 0 when the local value of the gas phase fraction overcomes 0.35: at this value the gas is physically still dispersed but the drag term is close to 0, originating a miscalculation of the fluid dynamical quantities, leading to the non-physical outcome of big clusters of bubbles [16]. Imposing the minimum value h_0 apparently solves this issue, but it does not exist a rigorous method for

its determination, since it is chosen dependently on the gas superficial velocity and the size of the column, making the simulation not fully-predictive.
The blending factor implementation, on the other hand, tackles this problem differently, accounting for the phase inversion: when the gas fraction is high, the drag force is reduced according to the blending factor and, when it overcomes the maximum dispersion value, air is treated as the continuous phase and the air-in-water drag force is not taken into account. Therefore, a valid choice of the blending model may replace the limitation to the swarm factor, with the advantage that the parameters are not dependent on the particular experimental configuration at certain operating conditions.

5.3.2 Blending approach vs h_0 approach

Fig. 5.2 and 5.3 show the results obtained with the blending model in OpenFOAM implementing the original swarm correction formula proposed by Simonnet (Eq. (2.24)) and compare them with both experimental measurements and the outcome of the simulations performed by Gemello et al. [16], who limited the Simmonet correlation as in (2.27) using $h_0 = 0.15$. The blended model slightly overestimates the gas fraction, especially in the central part of the section. This fact is due to the use of standard k-ϵ turbulence model for the liquid phase, which results in higher prediction for α_g in the heterogeneous regime in comparison with the RNG k-ϵ model used by Gemello et al. [16].
On the other hand, both models provide an excellent prediction of the axial water velocity (Fig. 5.3) in the homogeneous and heterogeneous regimes. Also in this case, the lower prediction suggested by OpenFOAM owes to a different turbulence model rather than the usage of blending factors.
To remove the effect of the different code and turbulence model used by Gemello et al. [16] from the comparison, the simulations based on the h_0 correction of the swarm effect were repeated in OpenFOAM using the `twoPhaseEulerFoam` solver with the standard k-ϵ model and without blending.
Comparison with the blending approach is shown in Fig. 5.4 and 5.5. The gas fraction prediction matches exactly at the center of the column, while the model implementing blending slightly overestimates the trend shifting toward the walls, in homogeneous and heterogeneous regime as well: in both scenarios the agreement of the simulation data to the experimental results may be considered satisfying.
The predicted axial velocity profiles (Fig. 5.5) are nearly coincident, proving how the choice between presenting a lower limit for the swarm correction factor and the usage of blending factors has a negligible impact on them. For this reason, the choice of the model and/or the eventual parameters adjustment needs to be executed on the basis of the prediction of α_g rather than the liquid velocity.

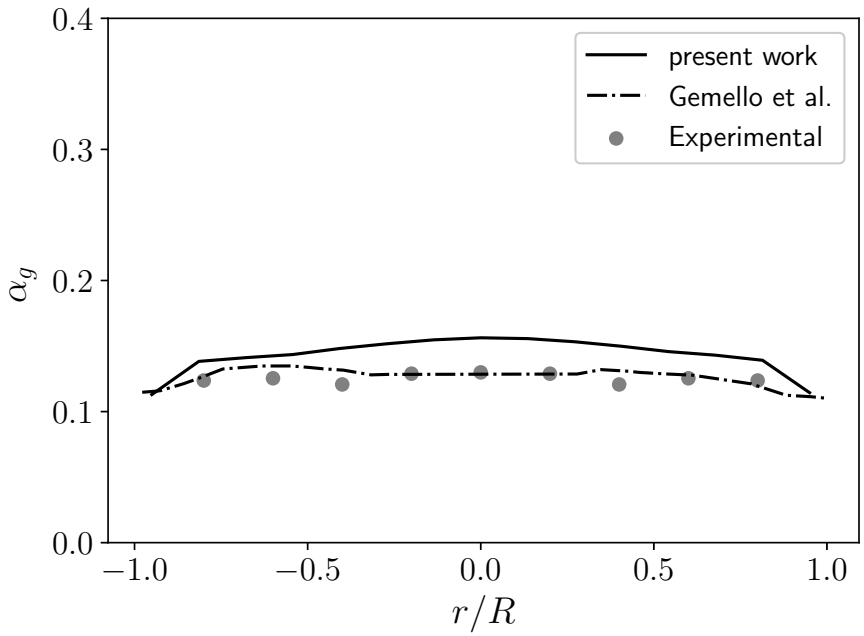

(a)

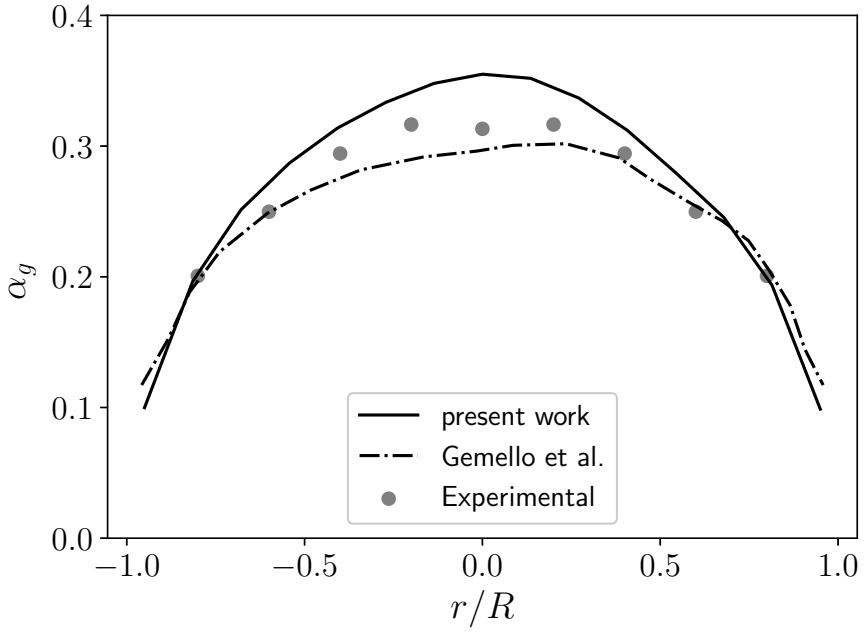

(b)

Figure 5.2: Time-averaged gas fraction profiles at height $z/D = 2.5$ at superficial gas velocity (a) $0.03\,\mathrm{m\,s^{-1}}$ and (b) $0.16\,\mathrm{m\,s^{-1}}$: comparison with Gemello et al. [16].

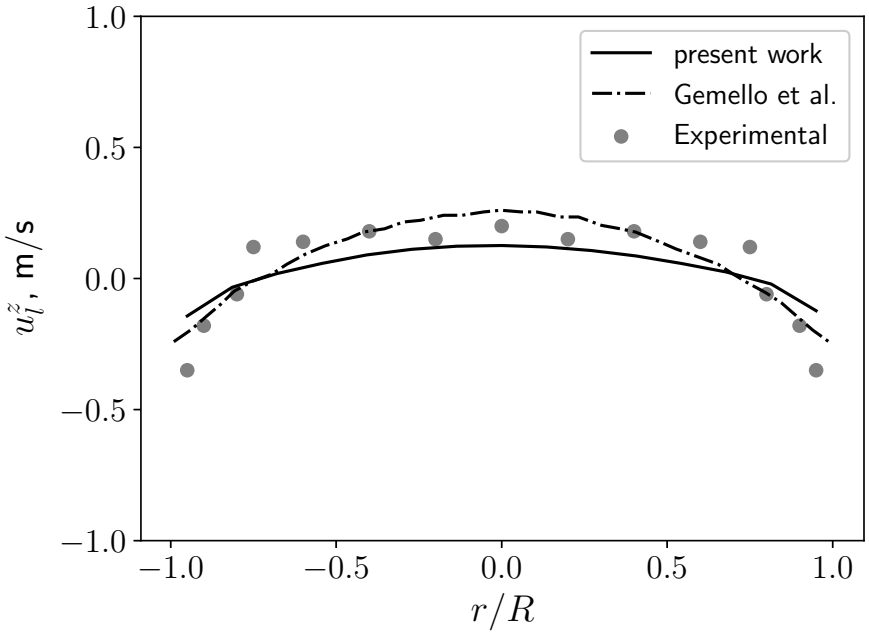

(a)

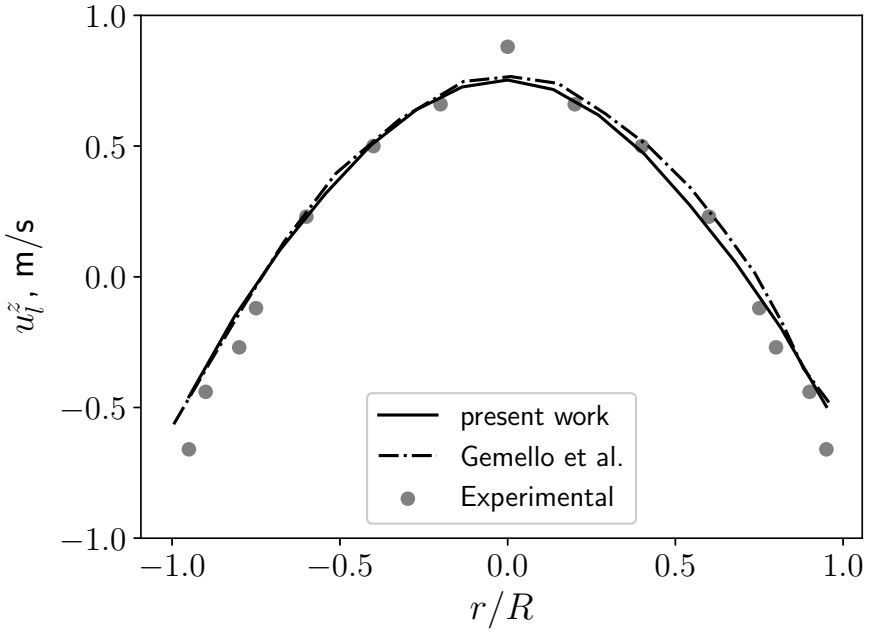

(b)

Figure 5.3: Time-averaged liquid z-velocity profiles at height $z/D = 3.75$ at superficial gas velocity (a) $0.03\,\mathrm{m\,s^{-1}}$ and (b) $0.16\,\mathrm{m\,s^{-1}}$: comparison with Gemello et al. [16].

5.3.3 Blending factors impact

In the modeling of bubble columns it is recommended to vary the blending parameters described in section 2.3 from the default values for both air and water (α_{FD} and α_{PD} equal respectively to 0.3 and 0.5) used for the calculation of f_1 (Eq. (2.45)) and f_2 (Eq. (2.46)) since they cause divergence issues.
As stated before, the primary interest in the head space is to achieve numerical stability rather than an accurate prediction of the water drops dispersion: since the water fraction values are extremely low in this domain area, the $\alpha_{FD,l}$ and $\alpha_{PD,l}$ parameters relative to water have been set equal to 0.05 and 0.2.
The choice must be conducted more carefully when considering the gas dispersion into water; the maximum gas fraction achievable by the gaseous phase, corresponding to a close-packing state of bubbles, is approximately 0.75 [107]: blending parameters thus for air must be chosen accordingly, a reasonable guess for the maximum value corresponding to partial dispersion may fall in the range 0.7–0.8. The limit for the total dispersion however needs to be set somewhere 0.1 and 0.5: a lower value will be unreasonably too close to zero and, on the other hand, a value larger than 0.5 will cause a steep linear variation from 0 to 1 in f_1.
Fig. 5.6a shows how the variation of $\alpha_{FD,g}$ (here and in the following the g subscript is dropped in sake of simplicity) affects the results in gas fraction and liquid velocity prediction for the heterogeneous regime ($U = 0.16\,\mathrm{m\,s^{-1}}$), spanning from 0.2 to 0.5. It is clear that the impact is totally absent in the outer part of the cross-section, where the gas fraction is in fact lower than 0.2, being thus completely included in the total dispersion range for any value of α_{FD} considered. In the central part of the column the predictions, although quite close, do not match perfectly: the gas phase here is considered as partly dispersed and the blending factor varies accordingly to the specified α_{FD}. The maximum deviation at the center of the column is however less than 1%, comparable or even smaller than the experimental error, showing, in any case, the robustness of the results.
Water axial velocity profiles are reported in Fig. 5.6b: the trends deviation is even smaller compared to Fig. 5.6a, except for the column axis where a negligible divergence is notable.
Considering the more accurate prediction of the gas fraction trend and the willing to set the slope of the linear piece of f_1 to the slightest possible value to make the simulation more stable, the best choice for $\alpha_{FD,g}$ is 0.2. Moreover, $\alpha_{PD,g}$ have to be set as well: again simulations using the values of 0.7 and .0.8 were run and the results are shown in Fig. 5.7. Unlikely the fully dispersion, this limit value has a complete negligible impact even on the air distribution throughout a section: both values therefore may be used but, in the light of what stated ahead, setting $\alpha_{PD,g} = 0.8$ would guarantee a less steep linear variation in the blending factor.

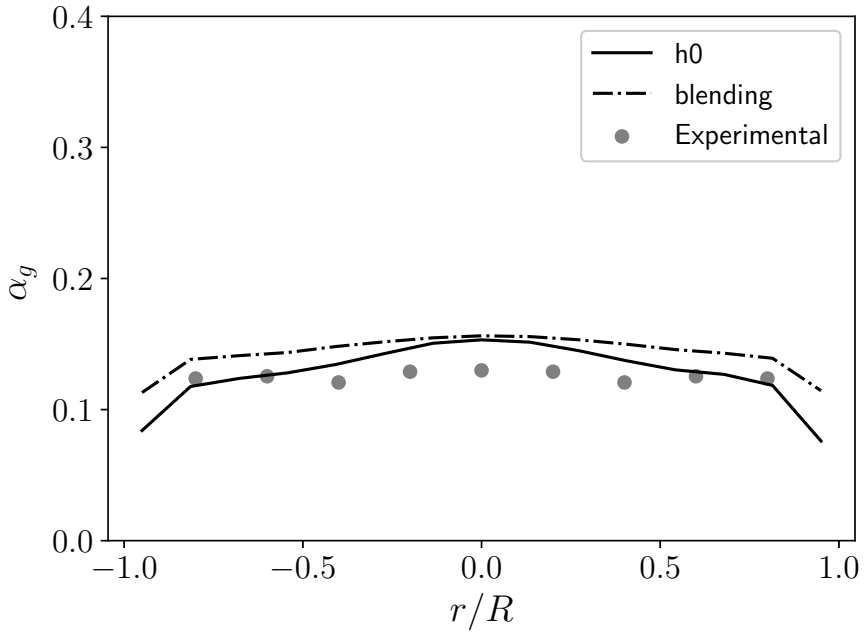

(a)

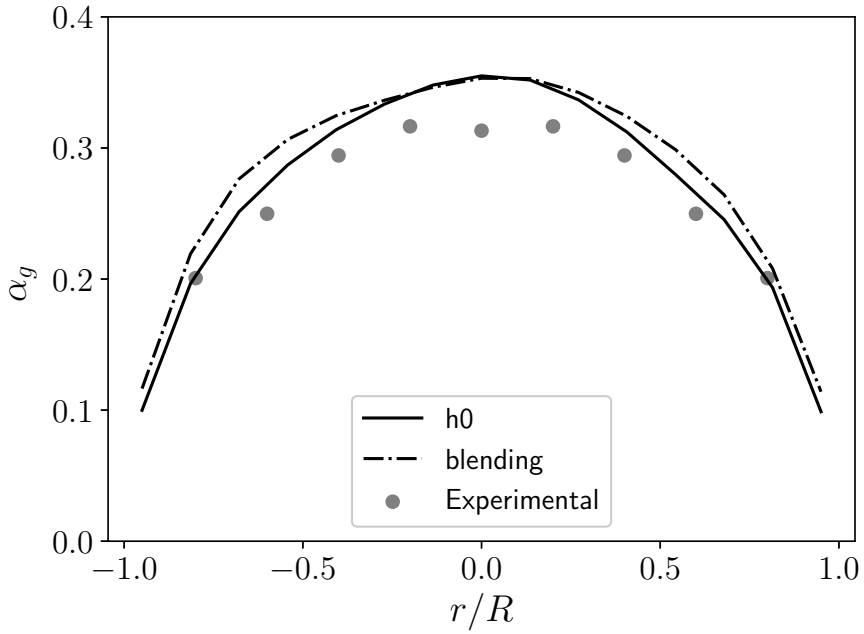

(b)

Figure 5.4: Time-averaged gas fraction profiles at height $z/D = 2.5$ at superficial gas velocity (a) $0.03\,\mathrm{m\,s^{-1}}$ and (b) $0.16\,\mathrm{m\,s^{-1}}$: comparison between the h_0 approach (with $h_0 = 0.15$) and the blending method in OpenFOAM.

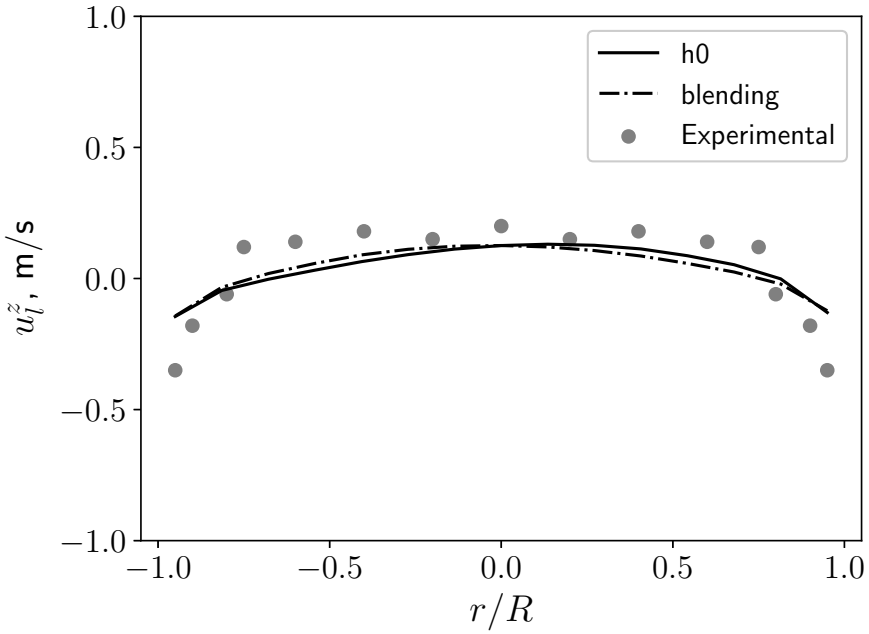

(a)

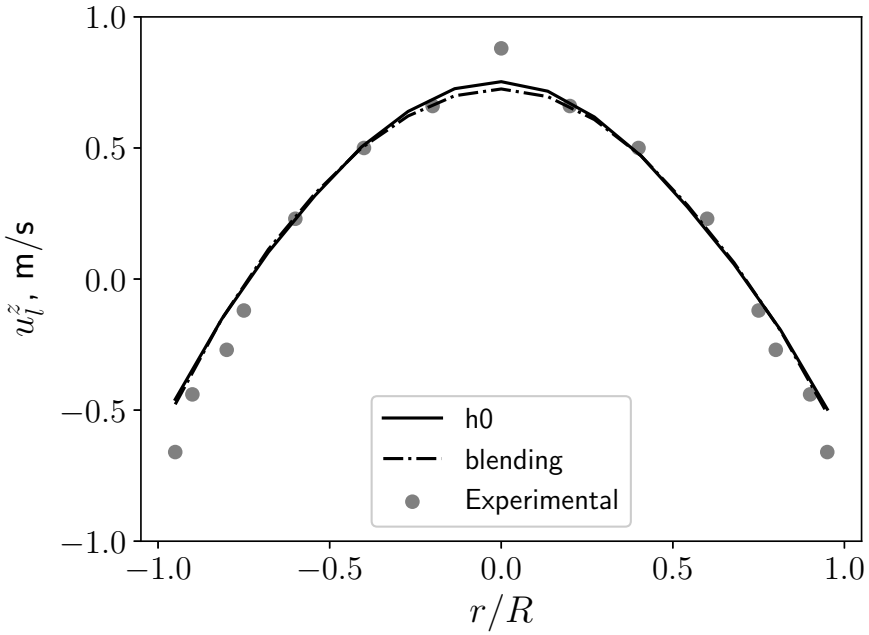

(b)

Figure 5.5: Time-averaged liquid z-velocity profiles at height $z/D = 3.75$ at superficial gas velocity (a) $0.03\,\mathrm{m\,s^{-1}}$ and (b) $0.16\,\mathrm{m\,s^{-1}}$: comparison between the h_0 approach (with $h_0 = 0.15$) and the blending method in OpenFOAM.

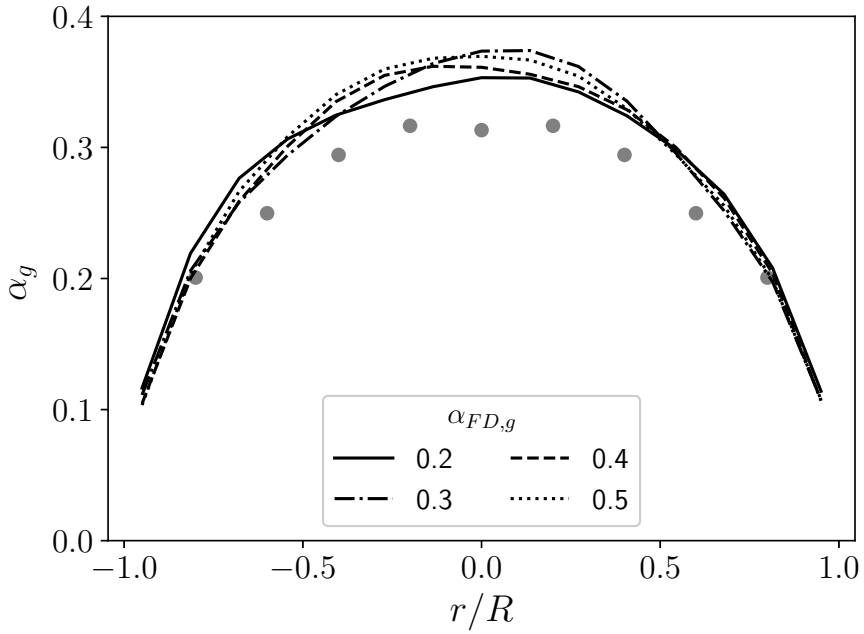

(a)

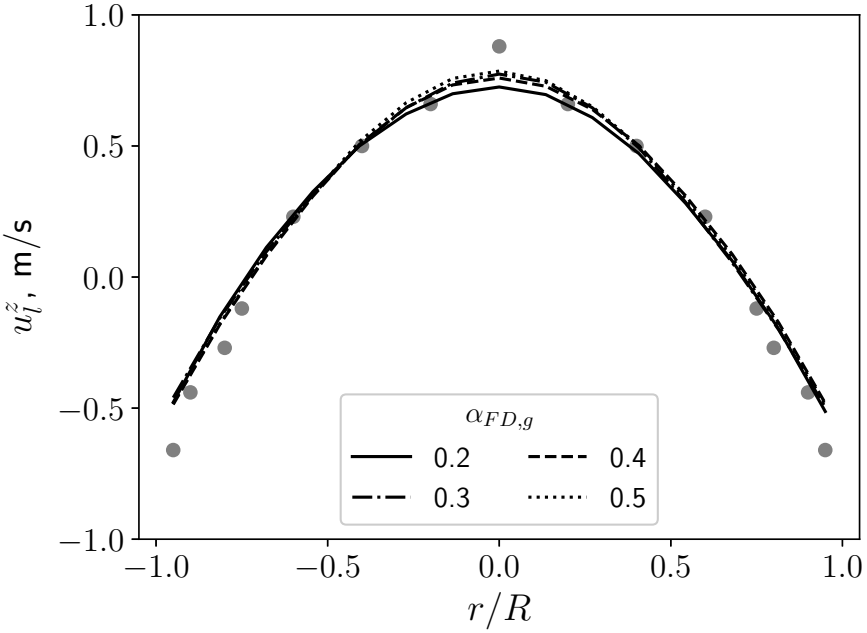

(b)

Figure 5.6: Time-averaged gas fraction (at height $z/D = 2.5$) (a) and water z-velocity profiles (at height $z/D = 3.75$) (b) at superficial gas velocity $0.16\,\mathrm{m\,s^{-1}}$: impact of $\alpha_{FD,g}$ parameter and comparison with experimental data (dots).

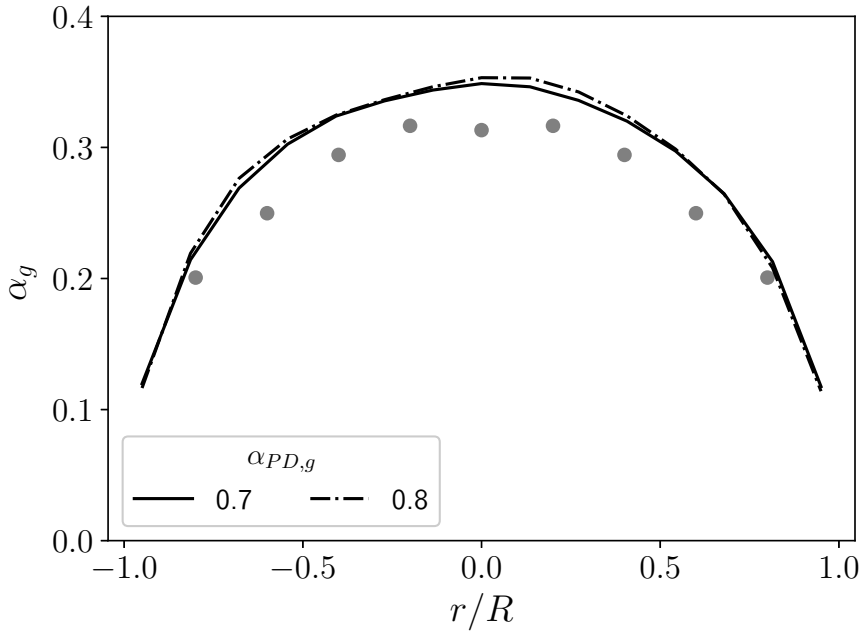

(a)

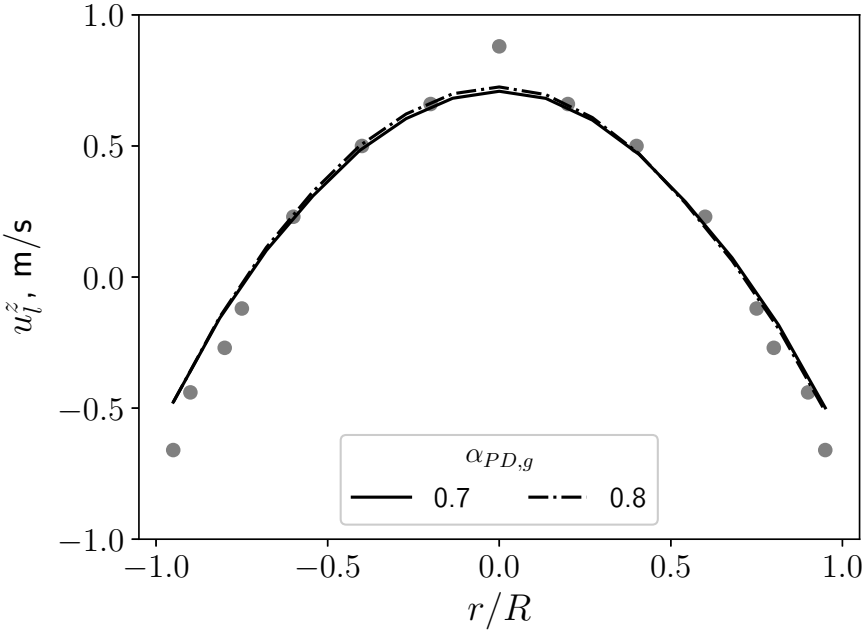

(b)

Figure 5.7: Time-averaged gas fraction (at height $z/D = 2.5$) (a) and water z-velocity profiles (at height $z/D = 3.75$) (b) at superficial gas velocity $0.16\,\mathrm{m\,s^{-1}}$: impact of $\alpha_{PD,g}$ parameter and comparison with experimental data (dots).

5.3.4 Impact of the lift force

Figs. 5.8 and 5.9 compare the volume gas fraction and water z-velocity profiles obtained activating the lift force using the lift coefficient C_L proposed by Tomiyama (Eq. (2.29)) with the ones where it is disabled and experimental data. The lift force has a negligible impact in the homogeneous regime, being the velocity profiles nearly uniform throughout the radial section; however when the superficial gas velocity U allows the transition between homogeneous and heterogeneous regime, both gas fraction and liquid axial velocity profiles flatten out if the lift force is activated.
This is probably due to the radial distribution of the water velocity, which causes a significant variation in the vorticity field (i.e. the curl of the water velocity, often denoted as $\boldsymbol{\omega}$), affecting the resulting lift force value according to Eq. (2.28). Fig. 5.10 shows the radial behavior of the magnitude of the vorticity vector at two different heights and superficial velocities. In the heterogeneous regime $\boldsymbol{\omega}$ can reach a value 5 times higher with respect to the homogeneous one, confirming that the discrepancies revealed in Fig. 5.9 are caused by the wide quasi-parabolic water velocity profile.
The use of Tomiyama correlation for lift force thus overpredicts the migration of the air bubbles in the wall direction, especially in the outer radial areas: here the vorticity reaches the highest values, flattening the corresponding gas fraction profile.
The reason of the worsening of the numerical prediction caused by the activation of the lift force could be twofold. On one hand, the correlation proposed by Tomiyama for the calculation of the lift coefficient is strongly dependent on the Eötvös number and, therefore, on the bubble size. The assumption of fixed bubble size thus may strongly impact the role of the lift force, since a proper implementation would require a full calculation of the bubble size distribution. On the other hand, the activation of the sole lift force might be not enough to enrich the quality of the flow prediction, thus possibly requiring the activation of other counteracting interfacial forces that balance the lift force. However it can be concluded that the lift force does not lead to an improvement in the modeling of the flow, as clearly shown by Figs. 5.8 and 5.9.

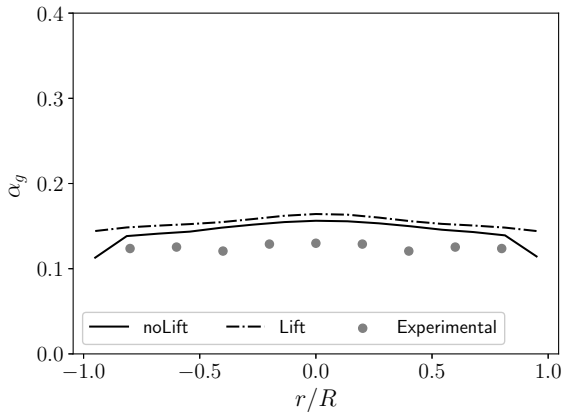

(a)

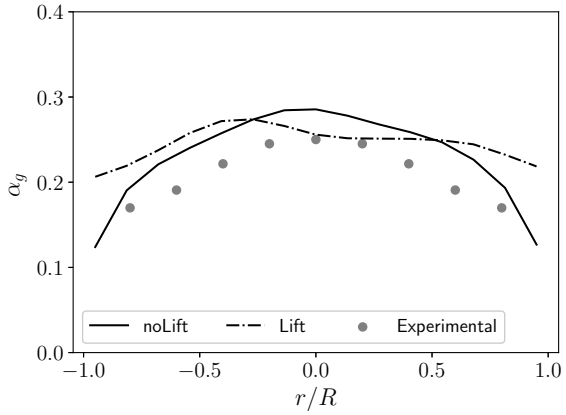

(b)

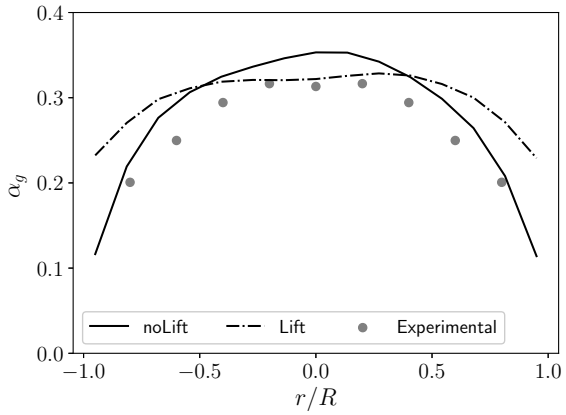

(c)

Figure 5.8: Time-averaged gas fraction profiles at height $z/D = 2.5$ at superficial gas velocity (a) $0.03\,\mathrm{m\,s^{-1}}$, (b) $0.09\,\mathrm{m\,s^{-1}}$ and (c) $0.16\,\mathrm{m\,s^{-1}}$: impact of the activation of lift force.

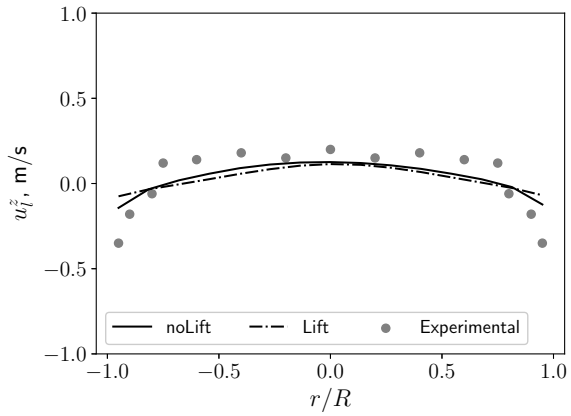

(a)

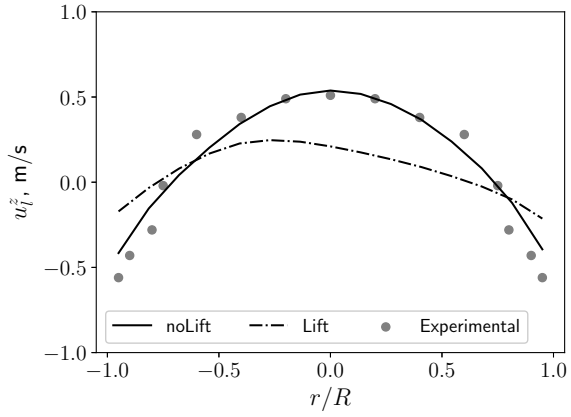

(b)

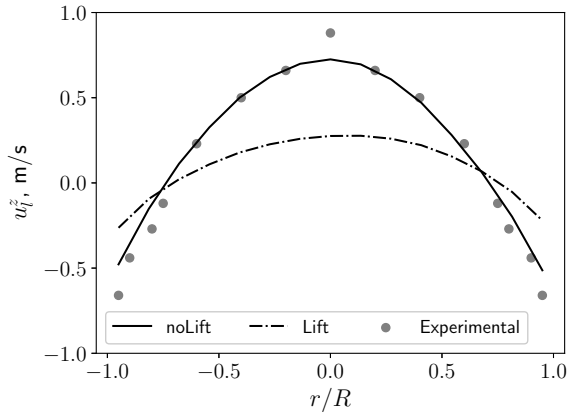

(c)

Figure 5.9: Time-averaged water z-velocity profiles at height $z/D = 3.75$ at superficial gas velocity (a) $0.03\,\mathrm{m\,s^{-1}}$, (b) $0.09\,\mathrm{m\,s^{-1}}$ and (c) $0.16\,\mathrm{m\,s^{-1}}$: impact of the activation of lift force.

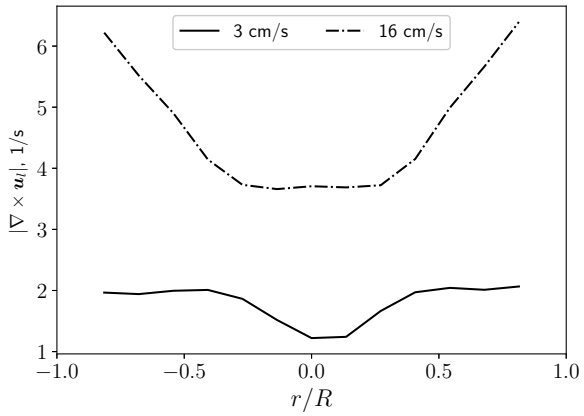

(a)

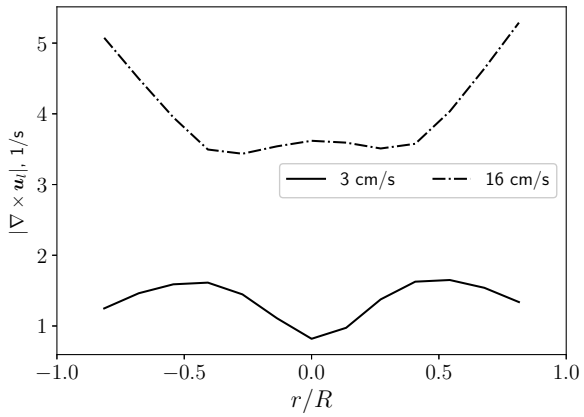

(b)

Figure 5.10: Time-averaged vorticity magnitude radial profiles at height $z/D = 2.5$ (a) and 3.75 (b).

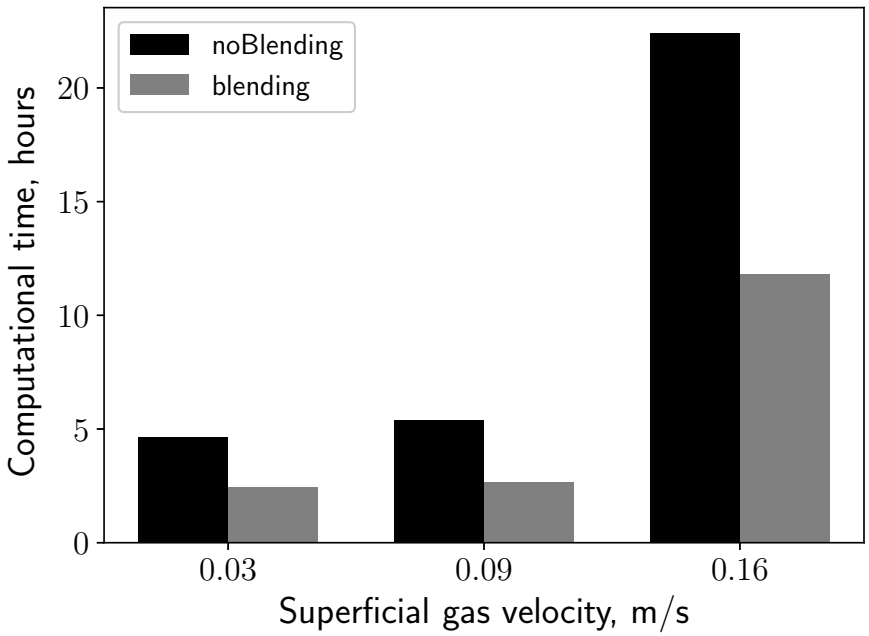

Figure 5.11: Computational time of simulation at different superficial gas velocities (4 processing units used).

5.3.5 Performance enhancement

Since the implementation of blending allows the local identification of the dispersed phase throughout the domain, the performed simulations may show a remarkable gain in numerical performance and computational speed compared to model where such blending is disabled. As a results, the portion of the domain above the free surface of liquid is properly modeled as a water-in-air dispersion, preventing the convergences issues previously caused by ignoring the phase inversion. Fig. 5.11 shows the computational time requested by the simulations with and without blending at various superficial velocities; every simulation is performed using 4 processing units Intel Xeon E5-2680 v3 2.50 GHz. It is clear that, both in homogeneous and heterogeneous regime simulations, the blending implementation allows a notable speed up in the overall duration of the computations, with a decrease of about 50% in the elapsed time.

5.4 Conclusions

The implementation of the blending approach, together with its capability of capturing the phase inversion, showed an excellent potential of predicting the fluid dynamics of a two phase column and significant improvements in computational

performances compared with other models that do not account such blending approach.
Moreover, it was proved that Gemello modification of Simonnet law for swarm correction, which sometimes appears ambiguous, may be replaced by an appropriate choice of blending parameters, leading to significant improvements in computational performances. In fact, this approach provides a more physical description of the dispersion, preventing the usage of semi-empirical correlations requiring *ad hoc* parameters to adjust the numerical issues arising from the miscalculation of the drag force when the gas hold-up is high. This matter is addressed through a definition of a partial dispersion zone, where the drag force relevance is often and eventually vanished as the phase-inversion zone is reached. The choice of these parameters was then investigated, with a sensitivity analysis that, starting from physical assumptions, led to their determination.
Moreover, the activation of lift force was then analyzed using the coefficient proposed by Tomiyama, showing that in the studied system this model overestimates the bubble migration toward the column walls, with the final result of flatter profiles for the local gas fraction.

Chapter 6

Slurry columns modeling

Before going through the application of the blending modeling, described in Chapter 5, to the LES turbulence models coupled with population balance in Chapter 7 and 8, this chapter [1] spotlights a variation of a classic RANS-modeled bubble column, where solid particles are dispersed in the liquid medium. Here the Ojima column, described in Section 4.3, is modeled and simulated with different percentage of solid loading. To conclude, the population balance modeling was coupled to the simulations to predict the bubble diameter in the presence of solid.
The main goal was the analysis of the impact of solid particles on the overall and local fluid dynamics of bubble columns and the comparison of their behavior with the analogous two-phase systems.
However, given the difficulty to obtain exhaustive experimental data from these systems due to their turbidity as mentioned in Section 4.3, an exhaustive validation cannot be performed until local experimental distributions of quantities such volume gas fraction, bubble diameter or velocities of at least one phase are thoroughly measured in slurry columns. In this perspective, the Ojima column was chosen because the experimental work performed, in terms of local measurements, is among the widest available in the literature. Nevertheless, being a square column, the traditional RANS approaches did not work perfectly and some numerical issues were detected at the corners of the sections. Therefore, some adjustments were required, like the activation of the lift and wall lubrication forces, to obtain satisfactory agreement with the experimental data even without the presence of the solid particles. Once the right modeling of the gas-liquid flow was identified, the method was be applied to gas-liquid-solid flows to test properly the validity of the approach with an additional solid phase, achieving good agreement with the experimental measurements.

[1] This chapter is mainly based on the paper [45]: F. Maniscalco, A. Raponi, M. Vanni, and A. Buffo, "Computational modeling of the impact of solid particles on the gas hold-up in slurry bubble columns," *Chemical Engineering Transactions*, vol. 86, pp. 1141–1146, 2021.

6.1 Computational set-up

The square bubble column investigated by Ojima [56] (Section 4.3) was simulated in Ansys Fluent 19 using a computational mesh made up of about 32000 cells with an average cell size of about 6 mm, selected after a mesh independency test. The final mesh is similar to the mesh that is used for the Kouzbour set-up in Chapter 8 (Fig. 8.1), which has the same geometry and dimensions. The average cell size is 1.5 cm.
Since the silica microparticles have mean diameter equal to 100 µm, the modeling approach used to account for their presence is the one considering the mix solid-liquid as a single pseudo-homogeneous slurry phase, described in Section 3.2.1. Therefore, the slurry viscosity and density as functions of the particles density and loading were calculated using Eq. (3.7) and Eq. (3.8).
The simulations performed with the inclusion of PBM were conducted to evaluate if the distribution of the bubble diameter has a detectable impact on the distribution of the gas fraction, which is the only quantity experimentally measured in terms of local distribution in this study. Therefore, the QMOM with 6 moments, described in Section 2.5.4, was applied to solve the population balance equations. The breakage events were accounted for by using the breakage frequency and daughter size distribution suggested by Laakkonen (Eq. (2.90) and Eq. (2.98)).
On the other hand, the identification of the appropriate coalescence kernel is less straightforward since coalescence implies various collision mechanisms [56]. In particular, we used a linear combination of (i) the coalescence kernel proposed by Wang modeling the collisions due to the wake entrainment effects (Eq. (2.113)) and (ii) the correlations proposed by Prince and Blanch modeling the coalescence due to turbulence fluctuations (Eq. (2.106)), buoyancy (Eq. (2.117)) and shear rate effects (Eq. (2.119)). This approach is required by the multiple phenomena characterizing bubble coalescence where solid particles are involved as well. With this perspective, the coalescence efficiency related to the velocity fluctuations, buoyancy and local shear rate is adjusted by the multiplier β, discussed in Section 3.2.2: the role of solid particles is predominant in these mechanisms and hence it must be taken into account in the relative coalescence kernel. The solid particles do not play a role in the coalescence mechanism caused by the wake entrainment phenomenon, therefore its presence is not accounted in the corresponding kernel (i.e. the multiplier β is not present in the expression of the coalescence efficiency related to wake entrainment). The final overall coalescence kernel used may expressed as:

$$h(L_1, L_2) = h_W(L_1, L_2) + h_{0,PB}\eta_{PB} = h_W(L_1, L_2) + (h_0^t + h_0^b + h_0^s)\eta_{PB}, \qquad (6.1)$$

where $h_W(L_1, L_2)$ denotes the Wang coalescence kernel due to wake entrainment and $h_{0,PB}$ the collision frequency expressed by Prince and Blanch as summation of terms modeling turbulent fluctuations (h_0^t), buoyancy (h_0^b) and shear rate (h_0^s)

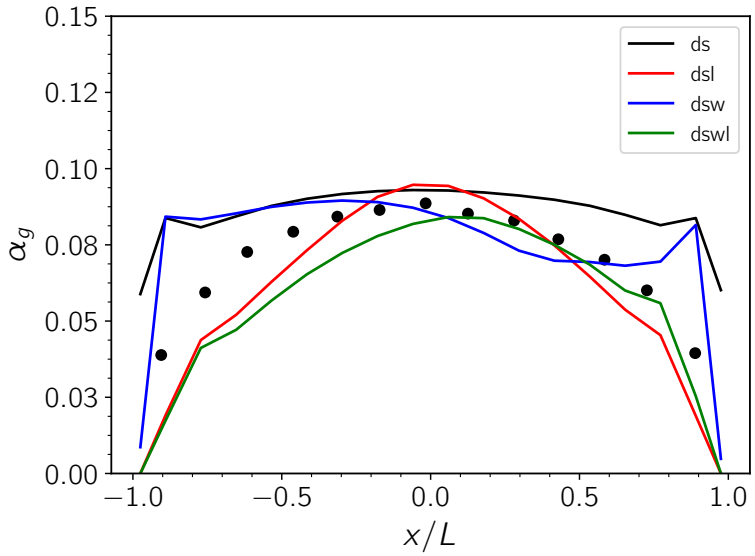

Figure 6.1: Time-averaged volume gas fraction at $z/L = 3$ with 0% of solid loading at gas velocity $U = 0.02\,\mathrm{m\,s^{-1}}$. In the legend, each letter is the initial of the activated interfacial forces in the relative plotted line: (d) drag force, (s) swarm correction, (l) lift force, (w) wall lubrication force.

effects, while η_{PB} is the collision efficacy, modified to account for the presence of solid particles as in Eq. (3.12).
Once more, since in bubble columns the flow pattern reaches only a pseudo-stationary state, the simulations were performed transiently and the results presented in the following section are averaged on a time period equal to 180 s, after having discarded the first 80 s of simulations to exclude the initial transient behavior.
In simulations with fixed bubble size, the bubble diameter was set equal to 8 mm accordingly to experimental observations. The gas phase was assumed laminar, while the slurry phase was modeled as turbulent accordingly to the standard k-ϵ model.
The drag force was implemented using the drag coefficient law proposed by Tomiyama for partially contaminated air-water systems (Eq. (2.19)) with the swarm factor correction suggested by Gemello (Eq. (2.27)) since in Ansys Fluent a fine phase blending modeling, such as the one investigated in OpenFOAM in Chapter 5 is not available. The choice of other interfacial forces is further discussed in Section 6.2.
At the inlet section the gas fraction was set to 0.5 and the velocity was set accordingly to the gas superficial velocity considered, while the turbulence intensity and viscosity ratio are equal to 0.05 and 10 respectively.
The local profiles shown in the next section are obtained averaging the sampling performed through the two perpendicular lines passing through the center of the

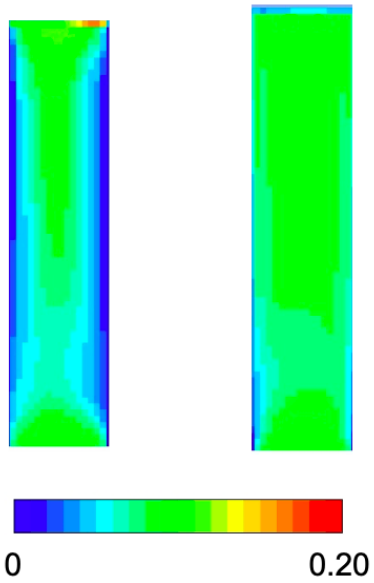

Figure 6.2: Contour plot of the time averaged gas volume fraction in the axial section at $U = 0.02\ \mathrm{m\,s^{-1}}$ and 0% of solid loading with (left) and without (right) the lift force.

section.

6.2 Interfacial forces

Primarily, a pure gas-liquid system was considered in order to assess the effective relevance of the interfacial forces besides the drag force. Local profiles of gas fraction at elevation $z/L = 3$, evaluated with gas superficial velocity equal to $0.02\,\mathrm{m\,s^{-1}}$, are reported in Fig. 6.1 for different sets of interfacial forces. In particular, the lift force and the wall lubrication force, with the coefficients proposed by Tomiyama (Eq. (2.29) and Eq. (2.40)) were tested. What stands out is that the combination of the drag force, including the correction accounting for the swarm effect, with the lift and wall lubrication forces provides the most accurate results. In fact, when the lift force is omitted the gas fraction profile is unrealistically flat. This is also evident when looking at the contour plots of the gas fraction in an axial section of the column with and without the presence of the lift force (Fig. 6.2). If the lift force is not activated, the distribution of the gas fraction is flat not only through a radial section, as shown in Fig. 6.1, but also along the longitudinal coordinate of the column.
To isolate the impact of the correlation used for the calculation of the lift coefficient

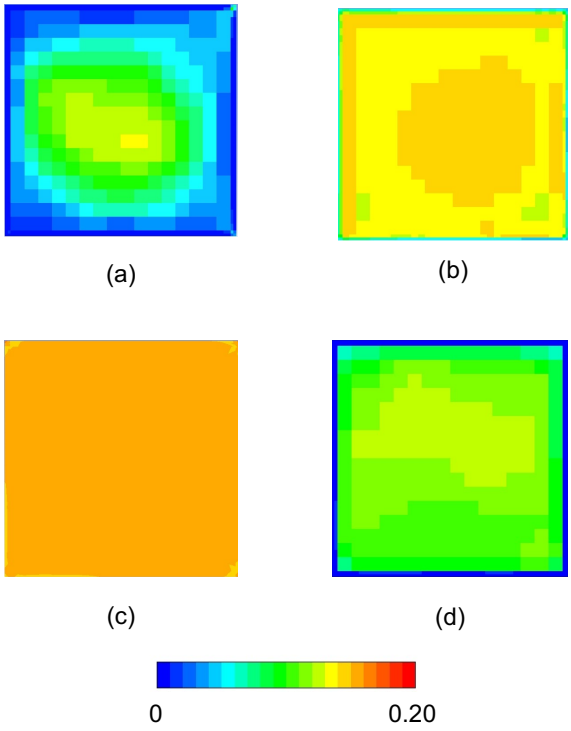

Figure 6.3: Contour plot of the time averaged gas volume fraction in a horizontal section ($z/L = 3$) at $U = 0.034$ m s^{-1} and 0% of solid loading with different lift coefficients. (a) Tomiyama, (b) no lift, (c) Legendre-Magnaudet, (d) Moraga.

C_L, simulations were performed also using the correlations proposed by Moraga (Eq. (2.33)) and Legendre-Magnaudet (Eq. (2.35)). Time-averaged contour plots of the gas fraction in a horizontal section, at $z/L = 3$ are depicted in Fig. 6.3 with various lift coefficients. What emerges is that the usage of other coefficients than the one proposed by Tomiyama leads to a unrealistic flat distribution of the gas fraction field, which does not correspond to experimental observations. Therefore, it can be concluded, at least using Ansys Fluent to simulate this specific case, the lift force with C_L calculated accordingly to Tomiyama must be included to achieve realistic results.
The role of the wall lubrication force is to numerically stabilize the simulations, especially at the corners of the column, peculiar features of a square geometry. Analyzing once more the contour plot of the time-averaged gas fraction in a radial section at at $z/L = 3$ (Fig. 6.4), it clearly appears that the wall lubrication force, here calculated using the correlation proposed by Tomiyama, reported in Eq. (2.40) significantly reduces the numerical issues occurring at the corners of the section,

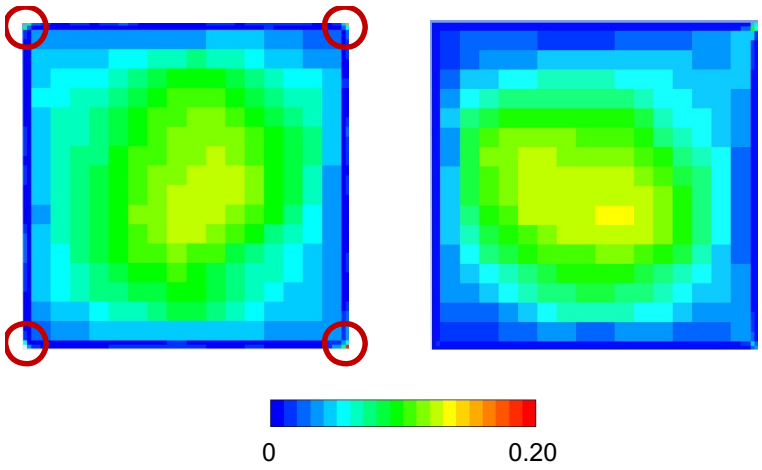

Figure 6.4: Contour plot of the time averaged gas volume fraction in a radial section ($z/L = 3$) at $U = 0.034\ \mathrm{m\,s^{-1}}$ and 0% of solid loading without (left) and with (right) lubrication force. Red circles indicate the numerical issues at the corner partially solved by the wall lubrication force.

where the mean gas fraction reaches unrealistic high value if lubrication is neglected. To conclude, the set of the interfacial forces that must be activated to perform stable RANS simulations and achieve physical results for this case is composed of the drag force, corrected by the swarm term, wall lubrication and lift force. With this set-up, the time averaged radial profiles of the gas fraction α_g provide a satisfactory agreement with the experimental measurements for C_s up to 20%, as shown in Fig. 6.5.

With the purpose of further improving the quality of the results and, mostly, consolidating the numerical stability achieved with the implementation of the wall lubrication force, the inlet condition of the gas velocity was modified by simulating a noisy disturbance on the velocity distribution at the sparger. The idea behind on this choice relies on the possibility that the velocity fluctuations may dismiss the gas accumulation at the corners of the section. The noise of the inlet gas velocity is implemented as summation of sinusoidal functions, whose spatial average is equal to the undisturbed inlet velocity:

$$U(x,y,t) = U_0\left[1 + 0.2\left[\left(\sum_{k=1}^{3} a_k(t)\sin\left(2k\pi\frac{x}{L}\right)\right) + \left(\sum_{k=1}^{3} b_k(t)\sin\left(2k\pi\frac{y}{L}\right)\right)\right]\right] \tag{6.2}$$

with U_0 being the undisturbed inlet velocity. $a_k(t)$ and $b_k(t)$ are time dependent coefficients:

$$a_k(t) = \sin\left(\frac{2\pi}{T}t + \alpha_k\right), \tag{6.3}$$

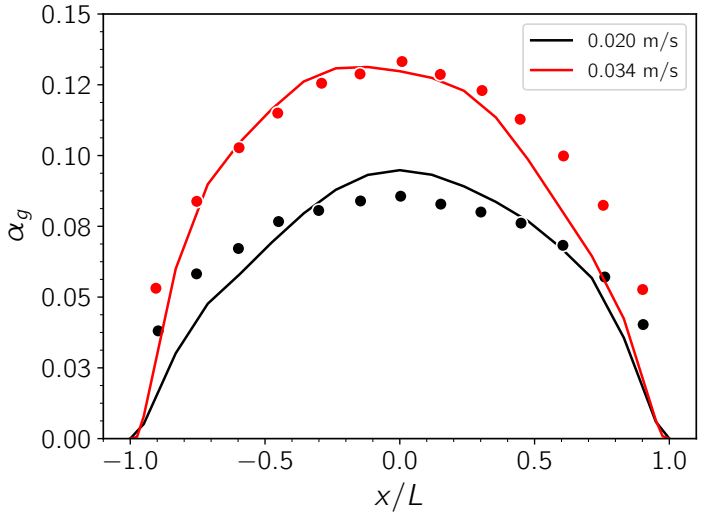

(a)

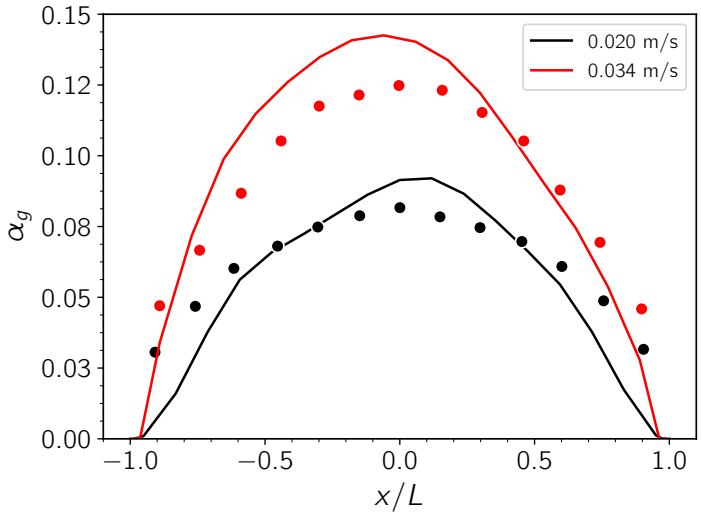

(b)

Figure 6.5: Time averaged volume gas fraction at $z/L = 3$ with (a) 10% and (b) 20% of solid loading and gas superficial velocity of 2.0 and 3.4 cm s^{-1}

$$b_k(t) = \sin\left(\frac{2\pi}{T}t + \beta_k\right). \tag{6.4}$$

Here T is the period in the time domain, α_k and β_k random numbers in the range $[-\pi, \pi]$. Fig. 6.6 shows the inlet velocity distribution for $U_0 = 0.02\,\mathrm{m\,s^{-1}}$. Nevertheless, this variation of the inlet velocity did not show a significant effect on the final outcome of the simulations, and therefore is omitted in the following CFD-PBM simulations.

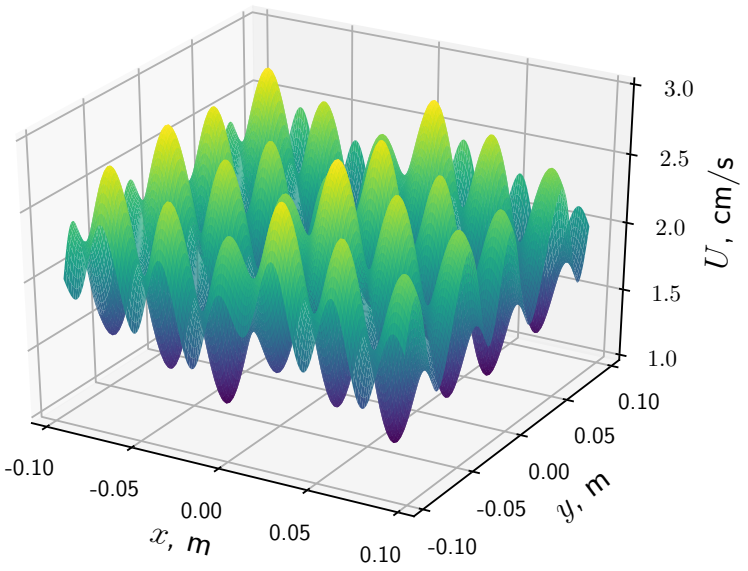

Figure 6.6: Instantaneous snapshot of the velocity disturbance at the inlet section with $U_0 = 0.02\,\mathrm{m\,s^{-1}}$.

6.3 CFD-PBM simulations

The quality of the results may be also improved if the bubble diameter is not fixed but estimated locally throughout the domain. With this aim, a population balance model was coupled to the CFD simulations as described in Section 6.1. However, the experimental work did not provide a local distribution of the mean bubble diameter and, therefore, the impact of the CFD-PBM coupling should be assessed by the variation of the local gas fraction radial profiles compared with the simulations performed at fixed diameter.

The outcome of the simulations confirms the experimental trend, where it was reported that the increase in the volumetric concentration of the solid particles promotes coalescence and the increase of the mean bubble size. Fig. 6.7 shows the instantaneous contour plot of the Sauter mean diameter, d_{32} at the superficial gas velocity U equal to $0.02\,\mathrm{m\,s^{-1}}$ and with solid loading C_s equal to 10% and 20%. The increase in the bubble size is remarkable (from about 6 to 15 mm) and is notable throughout the column and it is consistent with the experimental observation by Ojima et al. [56], who followed up the evolution of the size of a single bubble with the addition of the solid particles. However, as aforementioned, a thorough

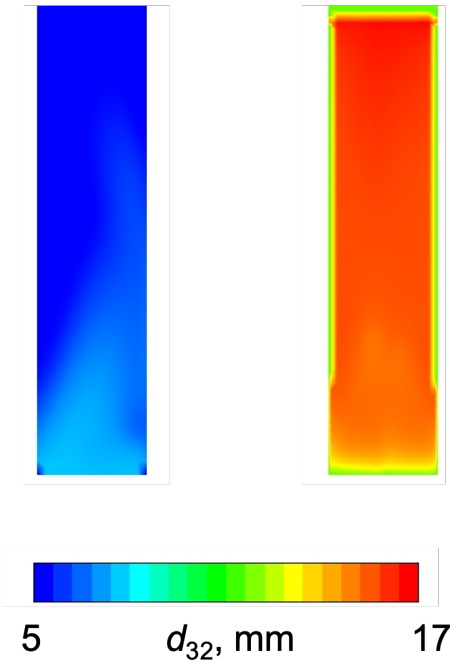

Figure 6.7: Contour plot of the instantaneous Sauter diameter in the axial section at $U = 0.02\,\mathrm{m\,s^{-1}}$ and solid loading equal to 10% (left) and 20% (right).

validation of the model is not practicable given the lack of the local distribution of the bubble size along the column.
When comparing the local distribution of the gas fraction with and without the usage of PBM, shown in Fig. 6.8, it is striking that, in such conditions, the implementation of a PBM modeling and the subsequent estimation of the local mean bubble size did not contribute to a noteworthy improvement of the results and the prediction of the experimental data, especially when the gas superficial velocity is equal to $0.02\,\mathrm{m\,s^{-1}}$. The difference is larger when U is increased to $0.034\,\mathrm{m\,s^{-1}}$; however, in our opinion, there is not a considerable gain in the accuracy of the results to compensate the usage of PBM models, which are considerably computational demanding.
Moreover, at $U = 0.034\,\mathrm{m\,s^{-1}}$ a slight underprediction of the gas fraction in the outer region, close to the walls, may be detected, especially with $C_s = 10\%$. This could suggest that solid particles may have an impact on the later motion of the bubbles and, hence, on the lift force as well. In this scenario, the lift coefficient C_L should be corrected in order to consider this effect promoted by the solid particles.

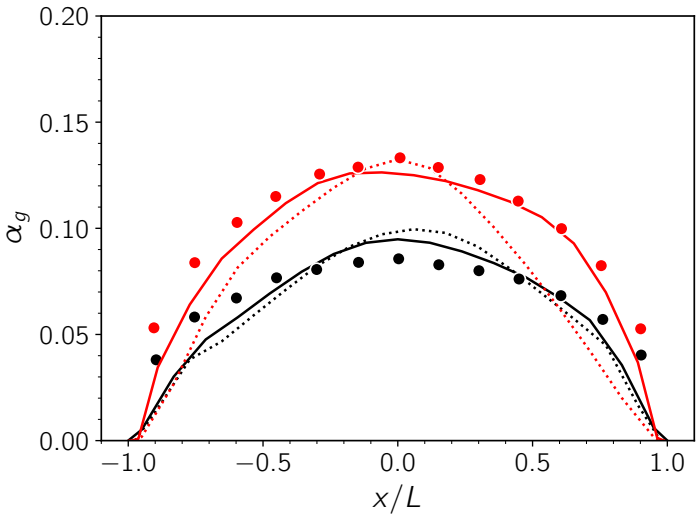

(a)

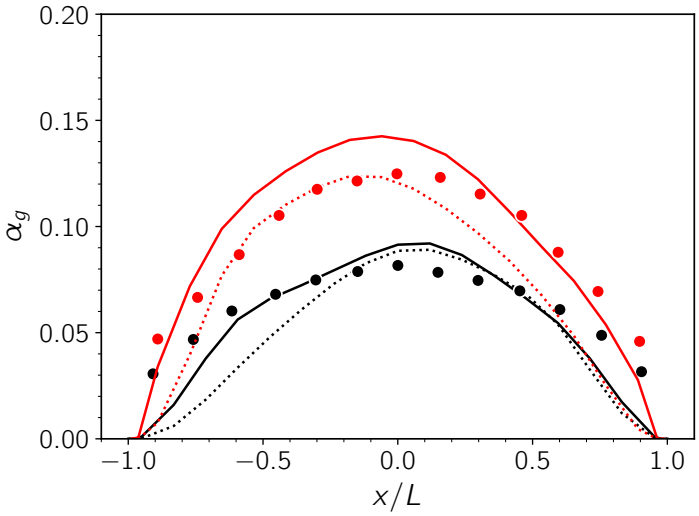

(b)

Figure 6.8: Time averaged volume gas fraction at $z/L = 3$ obtained with CFD (solid lines) and CFD-PBM (dotted lines) simulations with (a) 10% and (b) 20% solid loading at $U = 0.02$ (black lines) and $0.034\,\mathrm{m\,s^{-1}}$ (red lines).

6.4 Conclusions

The simulations here discussed tried to shed lights on the modeling of slurry bubble columns, confirming the difficulty of the formulation of a consistent model. This difficulty is even worsened by the experimental procedures for sampling flow quantities such as gas fraction or bubble diameter, which become challenging to perform

when solid particles are present in the liquid medium.
Furthermore, the square section of the column and the adoption of the RANS turbulence approach produced numerical issues, especially at the corners of the section and exceedingly flat profiles. As a consequence, the modeling of this system required specific assumptions to provide satisfactory results, such as the implementation of the wall lubrication force and the lift force, even for pure two-phase flows. However, the modeling framework identified with the gas-liquid simulations was successfully applied for the gas-liquid-solid configurations as well.
The coupling of a population balance model to the CFD simulations allowed to estimate the bubble size distribution in the column but, however, did not significantly improve the quality of the results obtained using a fixed bubble diameter.

Chapter 7

LES and LES-PBM modeling

In this chapter[1] the blending model, described in Chapter 5 in the framework of a RANS turbulence approach, is further extended to a LES turbulence approach. To strengthen its validity, three formulations for the subgrid-scale viscosity were tested in different regimes and operating conditions. Results showed the excellent capability of the LES framework to predict such flows.
To conclude, a PBM model is coupled to LES simulation which is, to best of our knowledge, a major novelty in the computational modeling of the bubble columns.

7.1 Introduction

In the computational description of bubble columns, turbulence modeling is crucial and has been a topical matter of scientific interest. In particular, the ambitious aim of the latest research efforts is the formulation of a simple and effective model for covering a wide range of operating conditions, from transition to fully turbulent regimes [10, 38, 114].
Within this framework, the RANS approach is the most used and k-ϵ closures have shown the best performances [16, 29]. However, the intrinsic averaging process of RANS models inevitably causes loss of information, especially when the flow field is complex as in bubble columns. On the other hand, LES models attempt to address, at least partially, this issue: in such models the turbulence spectrum is exactly resolved at the larger scales, while only the turbulence phenomena related to the smaller scales of motion are modeled. In this perspective, a cut off length Δ is defined to separate the resolved and modeled field (Fig. 2.13). Nevertheless, when applied to multiphase system, the LES approach presents several points to be

[1] This chapter is partly based on the paper [97]: F. Maniscalco, A. Buffo, D. Marchisio, and M. Vanni, "Numerical simulation of bubble columns: LES turbulence model and interphase forces blending approach," *Chemical Engineering Research and Design*, vol. 173, pp. 1–14, 2021.

addressed as well, such as the determination of the SGS length or the modeling for the smaller scales compared to the dimension of the dispersed phase, as described in Section 2.4.3.
Only lately the LES turbulence descriptions have been used for modeling bubble columns [18]. However, they have been mainly applied to simple systems, such as plumes [17,89] or flat 2D systems [208–210], or low gas superficial velocity and hold-up [28, 30, 38, 136], which are often far from industrial operating conditions. Here an Eulerian model is proposed, based on a LES description of the turbulence and the blending approach discussed in Chapter 5. The model is capable of properly describe the fluid dynamics of industrial-scale bubble columns under a large variety of operating conditions, from low to high gas velocity and for partially and fully aerated columns and, in this respect, it is superior to the usual RANS approach. Different test cases were used to further sustain the model validation: the fully aerated column experimentally studied by Gemello et al. [16] and described in Section 4.1 and the column investigated by McClure et al. [29, 67] and described in Section 4.2 and here represented in Fig. 7.1, where the gas can be fed either symmetrically (activating both sparger areas at the basis of the column, observable in Fig. 7.1) or asymmetrically (activating only one of the two halves of the sparger).

7.2 Computational set-up

As performed in Chapter 5 using a RANS approach, simulations were performed in the framework of the Eulerian-Eulerian method, using the drag force, including the swarm correction term, as the only interfacial force. While the impact of the lift is assessed in Section 7.3.3, the other interfacial forces are here omitted since, as discussed in Section 2.2.3, their role is secondary compared to the drag force.
Simulations were, once again, performed using the OpenFOAM 5.0 code `twoPhaseEulerFoam` setting an adaptive time step in such a way that the maximum Courant number is equal to 0.65. The maximum time step, which is used if the maximum Courant number condition returns a larger one, is equal to 0.001 s. As in the previous chapters, the results presented in the following sections were time averaged for 100 s after discarding an initial transient equal to 80 s, with the aim of removing the initial transient behavior from the statistics. In the discretization of the equations, the same temporal and spatial schemes as reported in Section 5.2 are here used.
The computational meshes, selected after a mesh independency analysis, have an average cell size between 0.015 and 0.020 m with a total number of cells equal to 60000 for the Gemello configuration and 41920 for both McClure symmetrical and asymmetrical operating conditions. The same grids were used also for the LES simulation, since they approximately satisfy the criterion proposed by Milelli et al. [18, 138], for whom the cell size should be 1.2-1.5 times the bubble size.

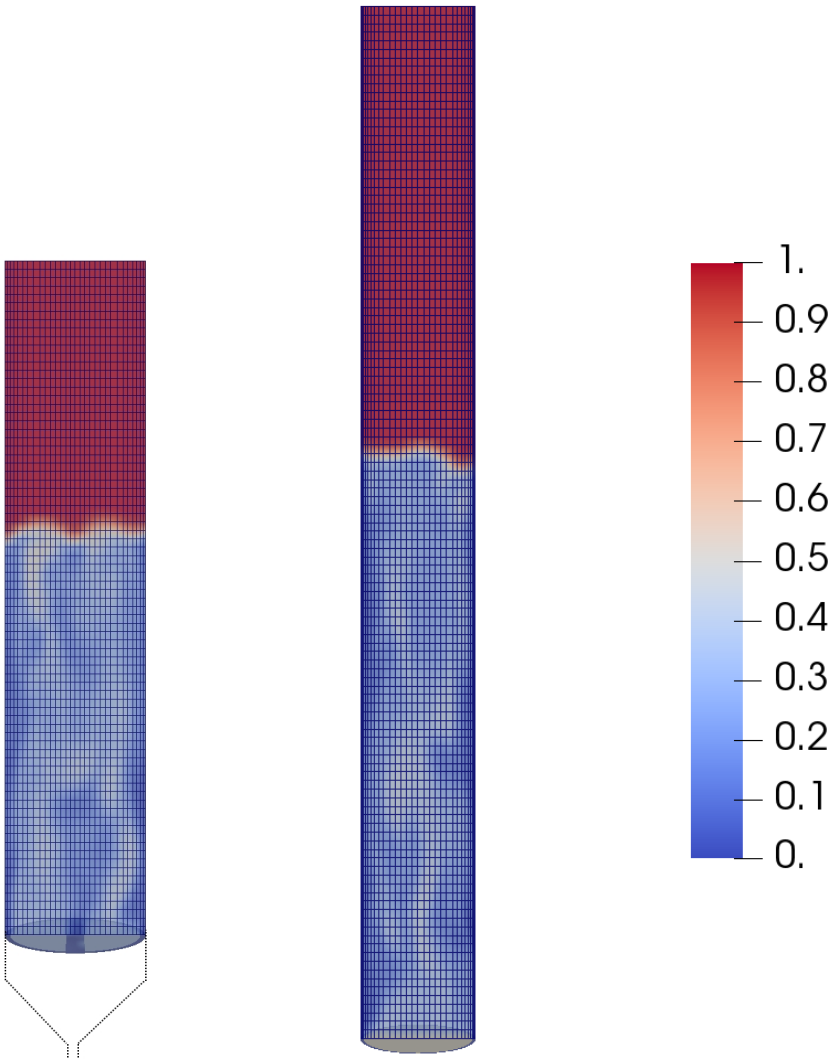

Figure 7.1: Configuration of McClure (left) and Gemello (right) columns, including an insight of the inlet sections. The instantaneous gas fraction α_g is plotted. The height H_t of the meshed cylinders is 1.865 m for McClure and 3.6 m for Gemello, and it is significantly higher than the liquid level.

7.2.1 Further considerations on computational meshes

To further confirm the suitability of the meshes, it must be verified that at least 80% of the turbulent kinetic energy field is entirely resolved [137]. As a consequence, no more than 20% of the turbulent eddies are described by the SGS model. Therefore, the two fields of the resolved ($k_{l,\mathrm{res}}$) and sub-grid scale modeled ($k_{l,\mathrm{SGS}}$) energy should be explicitly computed and compared. While the latter is calculated by the turbulence model, the former is explicitly calculated from the resolved water

velocity field. With this aim $\boldsymbol{u}_l$, was split into the time-averaged and fluctuating terms [2]:

$$\boldsymbol{u}_l = \bar{\boldsymbol{u}}_l + \boldsymbol{u}'_l. \tag{7.1}$$

$k_{l,\mathrm{res}}$ is then computed as the half of the trace of the resolved Reynolds stress tensor $(\overline{\boldsymbol{u}'_l \boldsymbol{u}'_l})$:

$$k_{l,\mathrm{res}} = \frac{1}{2}\,\mathrm{tr}(\overline{\boldsymbol{u}'_l \boldsymbol{u}'_l}). \tag{7.2}$$

However, when the flow is pseudo-stationary as in bubble columns, the choice of $\bar{\boldsymbol{u}}_l$ as time average between 80 and 180 s could lead to a sensible overestimation of $k_{l,\mathrm{res}}$, being the flow largely variable in time scales within this period. To address this issue, $\bar{\boldsymbol{u}}_l$, and $k_{l,\mathrm{res}}$ were calculating adopting a moving average with a window equal to $D/U \approx 2.54\,\mathrm{s}$ if $U = 0.16\,\mathrm{m\,s^{-1}}$. The choice of this window must be carefully performed, since it must be wide enough to distinguish average and instantaneous velocity, but, on the other hand, narrow enough to not overestimate the resolved turbulent kinetic energy. Fig. 7.2 reports the instantaneous and time-averaged z-velocity for a point at $r/R = 0.45$ and $z = 1\,\mathrm{m}$ in the Gemello column.
Therefore, the instantaneous values of $\boldsymbol{u}'_l$, the ratio $\frac{k_{l,\mathrm{res}}}{k_{l,\mathrm{res}}+k_{l,\mathrm{SGS}}}$ was first evaluated instantly and then time averaged from 80 to 180 s in the domains. Fig. 7.3 reports the percentage of resolved liquid turbulent kinetic energy at $z = 1\,\mathrm{m}$ and $z = 0.415\,\mathrm{m}$ for the investigated systems with gas superficial velocity $U = 0.16\,\mathrm{m\,s^{-1}}$. The results clearly indicate that more than 80% of the turbulent kinetic field is fully resolved, thus further confirming the meshes suitability.

7.2.2 PBM modeling

In the last part of this chapter (Section 7.3.6) coupled CFD-PBM are discussed, with the aim to assess the capability of a LES turbulence framework to predict the distribution of the mean bubble diameter as well. In fact, a population balance approach, and the relative solving algorithm, have not been coupled yet to a LES turbulence framework for describing the complex fluid dynamics involved in a bubble column. In this perspective, the aim would be to assess if LES modeling could be a valid alternative to the simpler and more popular RANS approaches when PBM equations are further added to the model. In fact, RANS-PBM modeling have often presented some issues especially in the heterogeneous regime, when the turbulence is well developed and the prediction of the bubbles breakage and coalescence, and therefore of the bubbles size, becomes harder [41].

[2] It is important to stress that this operation is performed on the *resolved* velocity fields: therefore the overbar $\bar{\cdot}$ and the apostrophe $'$ denote respectively a time-averaged and a fluctuating term of the *resolved* field.

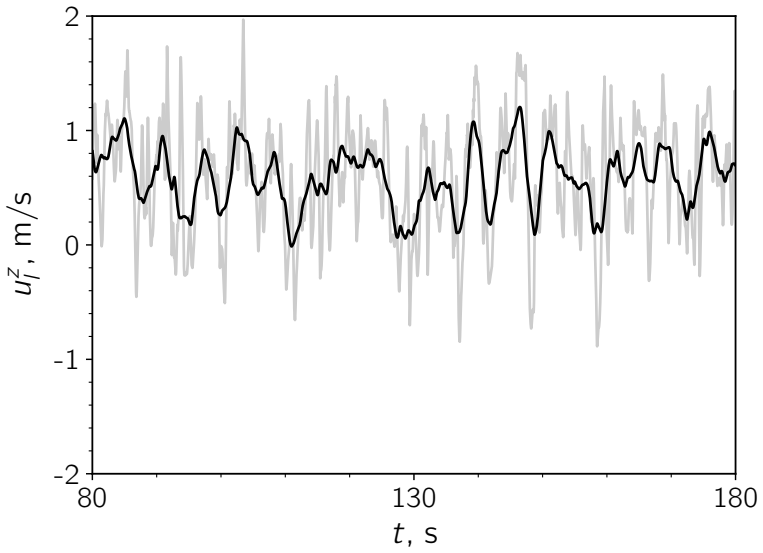

Figure 7.2: Sampled (shaded line) and moving-averaged (solid line) liquid z-velocity at $r/R = 0.45$ and $z = 1\,\mathrm{m}$ in the Gemello column and $U = 0.16\,\mathrm{m\,s^{-1}}$. A window of 2.54 s was used for the moving average.

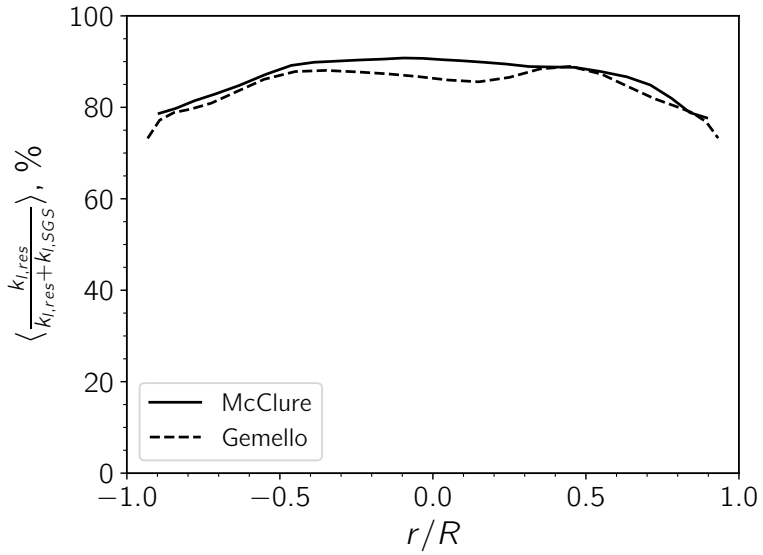

Figure 7.3: Time averaged radial profiles at $z = 1\,\mathrm{m}$ (Gemello) and $z = 0.415\,\mathrm{m}$ (McClure) of the percentage of the resolved liquid turbulent kinetic energy, $k_{l,\mathrm{res}}$, at $U = 0.16\,\mathrm{m\,s^{-1}}$

With this purpose, the PBM modeling was implemented and solved using the QMOM algorithm described in Section 2.5.4 and six additional transport equations,

each one relative to the corresponding moment, from order zero to five, of the NDF (Eq. (2.126)). In order to preserve numerical stability, the upwind scheme [211] was used for the spatial discretization of the six moments equations, while the time derivatives are discretized applying the Crank-Nicolson scheme [206], as for the other flow variables.
Breakage was modeled using the Laakkonen breakage rate (Eq. (2.90)) and daughter size distribution (Eq. (2.98)) regardless of the hydrodynamical regime. On the other hand, the coalescence is modeled differently in the homogeneous and heterogeneous regime since the prevailing mechanism leading to bubble collision and, eventually, coalescence is different as well. Therefore, for the homogeneous regime the original collision frequency first proposed by Prince and Blanch (Eq. (2.106) with $C_1 = 0.28$ was used, together with the coalescence efficiency proposed by Coulaloglou and Tavlarides (Eq. (2.124)) since, at such low gas velocity, the outcome of a collision is mainly related to the drainage time of the liquid film trapped by the two colliding bubbles. In Eq. (2.124) C_{CT} was set equal to 6×10^9. On the other hand, when the gas velocity is high and the heterogeneous regime is reached, Eq. (2.106) must be corrected in order to account for the high values of gas fraction: hence Eq. (2.112), first proposed by Wang is used. In particular, C_2' was set equal to 0.15, while Eqs. (2.108) and (2.110) were respectively used to calculate Θ and Λ in Eq. (2.112), with $C_\Lambda = 3.0$ and $\alpha_{g,\max} = 0.8$. Moreover, in this scenario, characterized by higher velocities, the coalescence efficiency is mainly related to the relative velocities between colliding bubbles, therefore the efficacy developed by Lehr (Eq. (2.122)) is used.
In the simulation, PBM was activated after the flow reached the pseudo-stationary state using a constant diameter. At the inlet, a log-normal distribution was assumed using as mean diameter the value experimentally observed and a deviation of 0.15 (a brief discussion on the impact of the inlet conditions is performed at the end of this chapter). As in the previous chapters, the results were sampled and then time averaged for 100 s after the pseudo-stationary state is anew reached.

7.3 Results and discussion

7.3.1 RANS and LES turbulence

Since the two columns here investigated have different aspect ratios, it would be interesting to look into the developments of the flow patterns above a certain height: in this way, the possible impact of the inlet section is vanished out.
Fig. 7.4 reports the averaged radial profiles of the volume gas fraction α_g and the liquid axial velocity u_l^z at different heights for the symmetrical configurations computed with the Smagorinsky-Zhang model (Section 7.3.2). Although the aspect ratio varies sensibly, the flow settling does not change significantly from one system

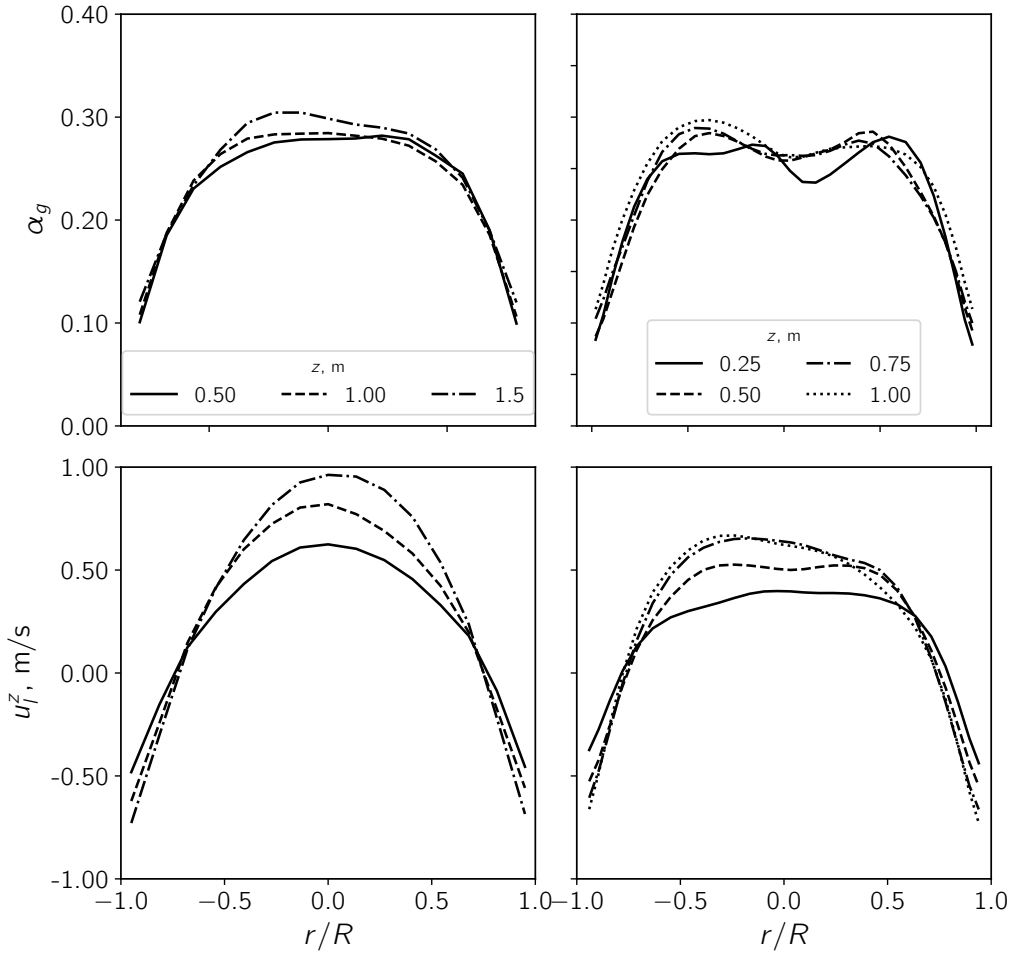

Figure 7.4: Time-averaged radial profiles of gas fraction (top) liquid axial velocity (bottom) at different heights for $U = 0.16\,\mathrm{m\,s^{-1}}$ in Gemello (left) and McClure symmetrical column (right) calculated by the Smagorinsky-Zhang LES model.

to the other, reaching a developed condition throughout the columns, as soon as the impact of the sparger becomes negligible.
A comparison of the turbulent fields, i.e. the liquid turbulent kinetic energy k_l and the turbulence dissipation rate ϵ_l, provides additional information about the difference with the same fields calculated by the traditional RANS models such as the standard k-ϵ. This comparison is interesting not only to investigate how these different models estimate the turbulent quantities, but, also to understand the effect

on the PBM coupling, whose modeling largely uses the turbulent dissipation rate as input variables for the formulation of the breakage and coalescence kernels. To this purpose, in the LES simulation the turbulence dissipation rate related to the liquid phase ϵ_l is estimated as [97]:

$$\epsilon_l = 2\nu_{l,\text{eff}} \left(\bar{\boldsymbol{S}}_l : \bar{\boldsymbol{S}}_l \right) \tag{7.3}$$

where $\bar{\boldsymbol{S}}_l$ is the strain rate of the resolved liquid field.
The time averaged radial profiles of the turbulent kinetic energy and turbulent dissipation rate, in the operating condition of symmetrical gas feed for both systems, are displayed in Fig. 7.5. The results are mostly consistent with the literature, and, in particular, confirm that the RANS standard k-ε model provides the highest estimation of k_l not only between specific RANS models, as reported in the work of Gemello [207], but also compared to the Smagorinsky-Zhang LES model.
Furthermore, another useful tool for model comparison could be the total power input related to the gas injection,

$$E_{\text{in}} = \frac{\pi}{4} D^2 H_0 U (\rho_l - \rho_g) g, \tag{7.4}$$

and the comparison with the integral of the turbulence dissipation rate calculated over the volume occupied by the gas-in-liquid dispersion V,

$$E_{\text{t}} = \int_V \alpha_l \varepsilon_l \rho_l \, dV, \tag{7.5}$$

Under the assumption that the whole energy furnished by the gas is entirely dissipated by the turbulence, the two terms should correspond. However, this comparison is non-trivial: Khan et al. [114] showed that this equivalence may not be valid in the heterogeneous regime and, recently, Magolan et al. [212] urged that the inclusion of the bubble induced turbulence may possibly result in large errors in the computation of the turbulent quantities. This could be the case of the investigation performed in this Chapter: for instance, at $U = 0.16\,\text{m}\,\text{s}^{-1}$ in the Gemello configuration the gas injection provides approximately 310 W, while the volume integral of the turbulence dissipation (Eq. (7.5)) yields 65 W for the standard k-ε model and 80 W for the Smagorinsky-Zhang model. Likewise, in the McClure symmetrical configuration the energy input associated to the gas is 185 W, whereas E_{t} for both cases is around 30 W.

7.3.2 LES turbulence models comparison

Several turbulence models were tested and they are compared in this section. With this aim, the simulations were performed at $U = 0.16\,\text{m}\,\text{s}^{-1}$ to guarantee a sufficiently high degree of turbulence.

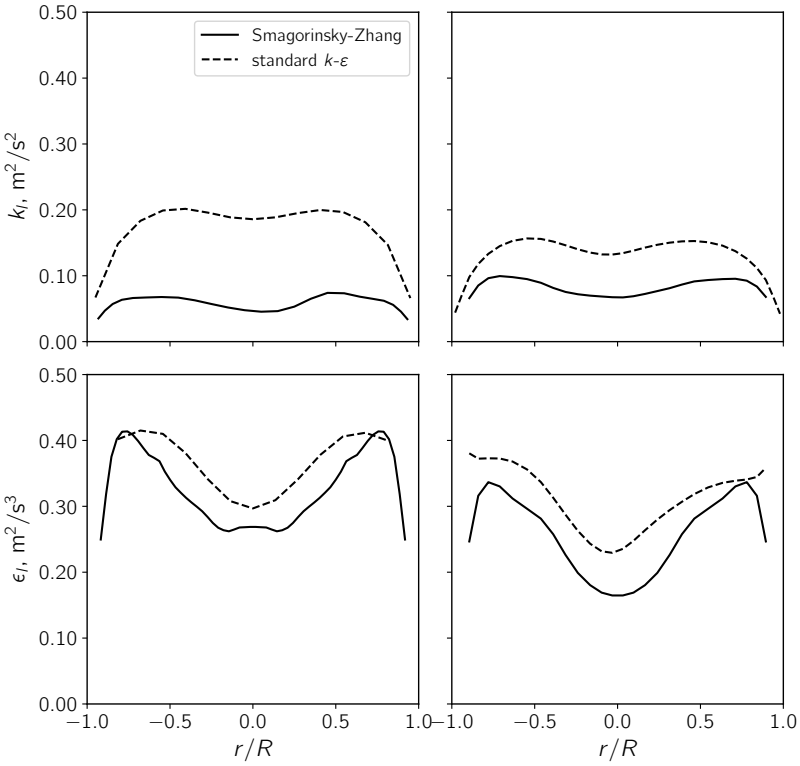

Figure 7.5: Time-averaged radial profiles of liquid turbulent kinetic energy (top) and turbulence dissipation rate (bottom) at $U = 0.16\,\mathrm{m\,s^{-1}}$ in Gemello column at $z = 1\,\mathrm{m}$ (left) and McClure symmetrical column at $z = 0.415\,\mathrm{m}$ (right).

On these grounds, the LES models for the calculation of the SGS viscosity described in Section 2.4.2 were used, and the outcome was compared to the standard k-ϵ RANS model as well . Results are respectively shown in Fig. 7.6 for the Gemello and Fig. 7.7 for the McClure symmetrical configurations. What mostly emerges is a broad equivalence of the LES models in predicting the behavior of the symmetrically-fed systems. Moreover, all LES models showed positive prediction performances, given the good match with experimental measurements that can be noted for both gas volume fraction and liquid axial velocity profiles. As largely discussed in Chapter 5, the results provided by the RANS formulation present a satisfactory accuracy as well; however, the deviation with experimental data is larger compared with the LES models.
Nonetheless, the most interesting results come from the simulations of the McClure set-up performed in the operating conditions of asymmetrical gas feed and they

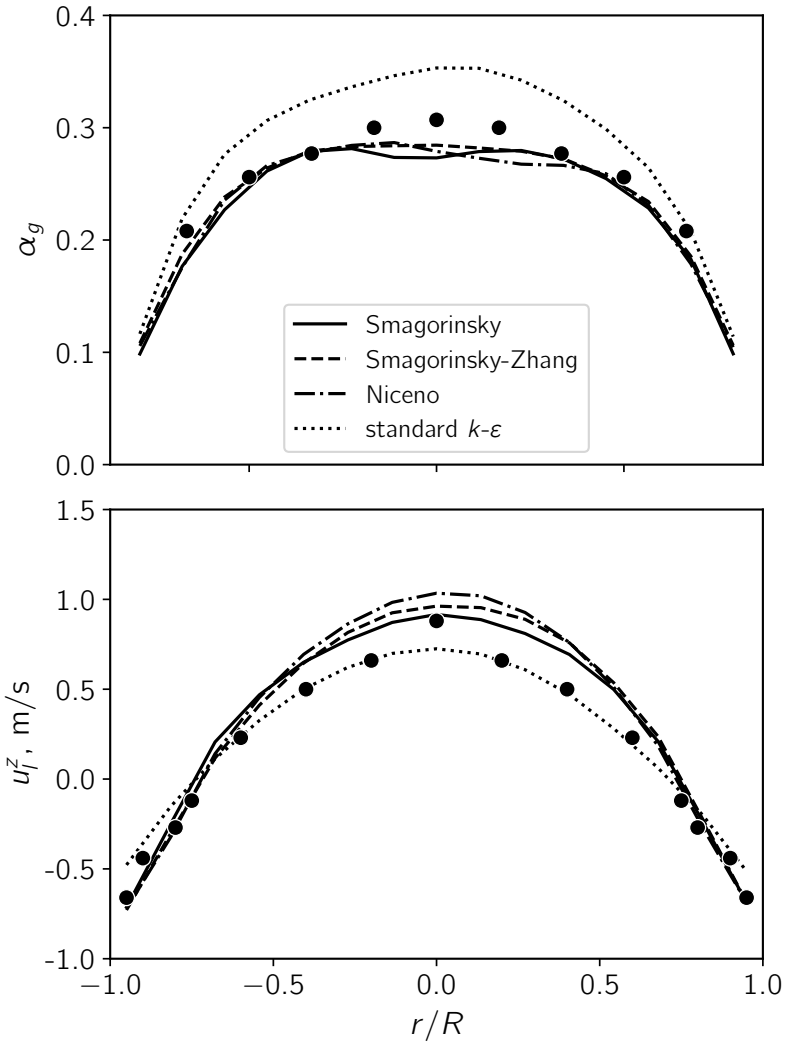

Figure 7.6: Effect of turbulence models at $U = 0.16\ \mathrm{m\,s^{-1}}$ in Gemello column and comparison with experimental data (circles): time-averaged radial profiles of the gas fraction at $z = 1\,\mathrm{m}$ (top) and the liquid axial velocity at $z = 1.5\,\mathrm{m}$ (bottom).

are depicted in Fig. 7.8. In particular, the three models within the LES framework showed a striking ability of capturing the peculiar flow patterns arising from an asymmetrical gas injection. In contrast, the RANS standard k-ϵ model was not capable to perform in the same way. The reason for such distance between LES and RANS turbulence models should be looked for in the radically different approach

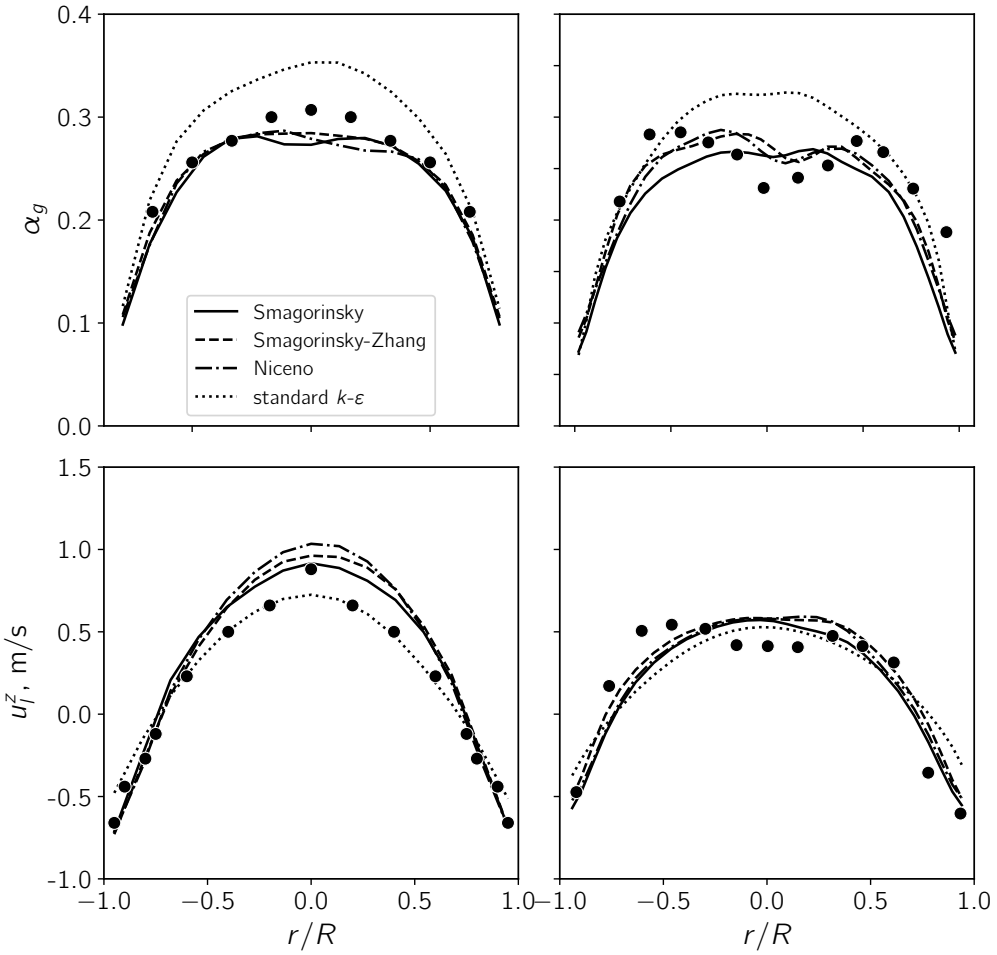

Figure 7.7: Effect of turbulence models at $U = 0.16\ \mathrm{m\,s^{-1}}$ in McClure symmetrical column and comparison with experimental data (circles) : time-averaged radial profiles of the gas fraction (top) and the liquid axial velocity (bottom) at $z = 0.415\,\mathrm{m}$ (left) and $z = 0.915\,\mathrm{m}$ (right).

in modeling the turbulence whose effects are exacerbated by the asymmetrical condition. As pointed out in Section 2.4, the RANS description involves an averaging procedure that unavoidably generates a loss of information on the flow field variance. The strong non-uniformity of the flow, originated by the asymmetrical gas injection, further shows up the weakness of this model.
On the other hand, the Smagorinsky, Smagorinsky-Zhang and Niceno LES models

showed a shared better capability to describe the asymmetrical gas flow, even if with different outcomes. However, it can be noted that the Smagorinsky-Zhang model, which takes into account also BIT effects, provided the most accurate description of the flow patterns and, therefore, the optimal results. This fact suggests that, in such heavily non-uniformity of the flow, BIT could play a much more relevant role compared to the systems where the gas is fed throughout the section of the sparger. Notwithstanding this, Niceno turbulence model, which computes the SGS viscosity including BIT as well, did not prove the same effectiveness. A straightforward explanation for this outcome is difficult, although it might be related to the average size of the computational grid, which may be not fine enough to solve with an acceptable degree of accuracy the transport equation for k_l, required by the Niceno model.
In conclusion, the most performing LES turbulence model to describe both symmetrical and asymmetrical operating conditions appears to be the one proposed by Smagorinsky with the addition of the BIT phenomenon inclusion, coherently with Eqs. (2.69) and (2.71), namely the Smagorinsky-Zhang model. It should be noted that the usage of a LES turbulence approach could be successfully applied to square column as well, as discussed in Chapter 8. In particular, the choice of the LES over the traditional RANS approach allowed to simulate these systems using only the swarm-corrected drag force as interfacial forces, thus addressing the issues highlighted in Chapter 6 which were only partially solved by the inclusion of secondary interfacial forces. Therefore, the adoption of a LES turbulence framework could represent a big step forward toward the formulation of a single model valid for every operating condition or column geometry.
Finally, Figs. 7.9 and 7.10 delineate a picture of the flow field in the asymmetrical and symmetrical gas-feeding conditions in McClure set-up (the outcome for the Gemello set-up is analogous to the latter), depicting respectively the contour plot of the volume gas fraction and the vector plot of the liquid z-velocity, both as time averaged variables. As widely expected, since the gas feed in the asymmetric case is performed only in the left half side of the cross-section area, the flow field is strongly asymmetrical in the lower region close to sparger. As the gas bubbles flow up, the flow becomes progressively more symmetric approaching the liquid free surface, coherently with experimental inspections [67]. On the contrary, when the gas injection is performed uniformly across the sparger, a symmetric flow field is reached throughout the system, including the region directly above the sparger.

7.3.3 Impact of the lift force

In Section 5.3.4 it was proved that, in the framework of RANS turbulence description coupled with blending models, the implementation of the lift force may lead to significant mispredictions of the flow patterns: the aim of this Section is to verify if this is valid for the LES approach as well. Furthermore, the operating condition of

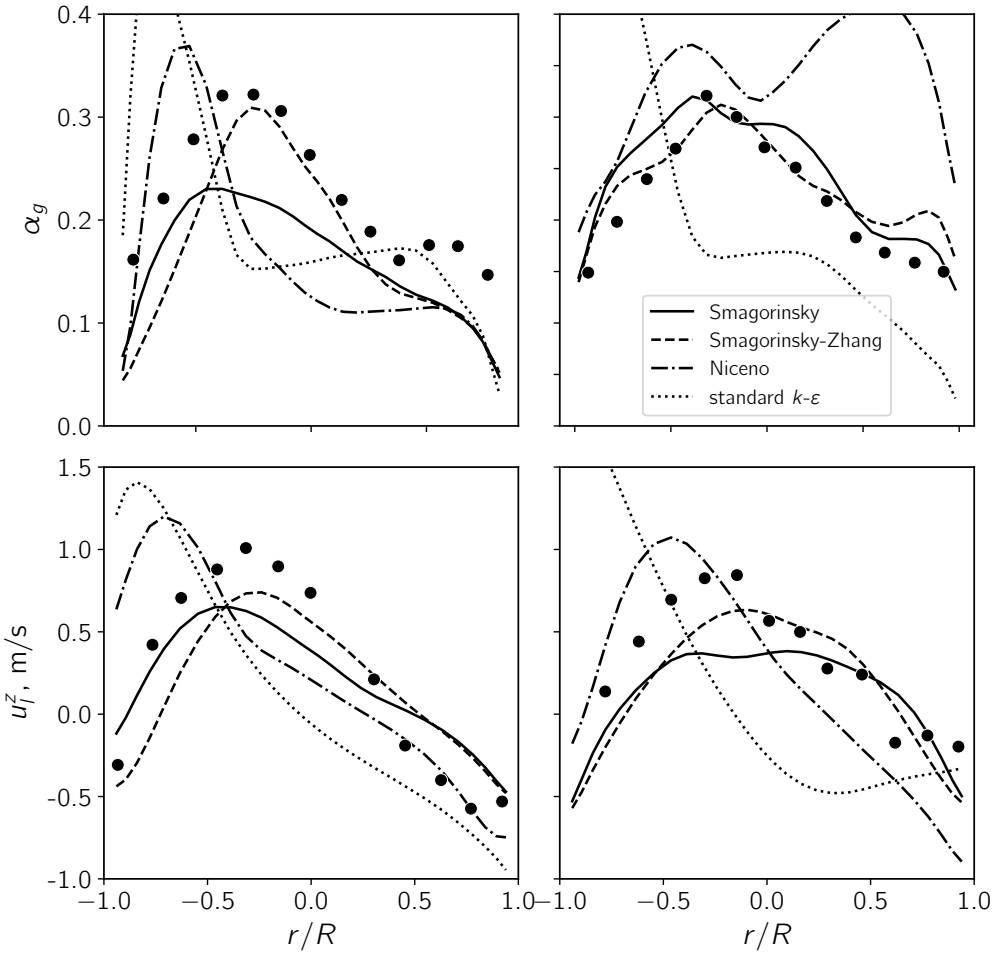

Figure 7.8: Effect of turbulence models at $U = 0.16\,\mathrm{m\,s^{-1}}$ in McClure asymmetrical column and comparison with experimental data (circles) : time-averaged radial profiles of the gas fraction (top) and the liquid axial velocity (bottom) at $z = 0.415\,\mathrm{m}$ (left) and $z = 0.915\,\mathrm{m}$ (right).

the asymmetrical feed is crucial to this purpose because, being a transversal force, it acts perpendicularly to the main direction of the bubbles flow and is related to the phases velocity gradient. Therefore, if present, the lift force should be predominant in the asymmetrical conditions.

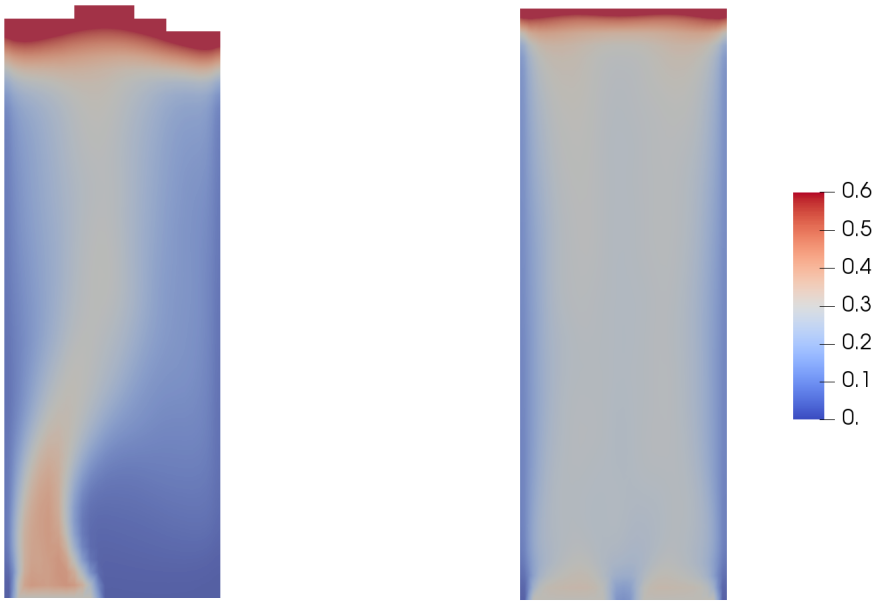

Figure 7.9: Contour plots of the time-averaged gas volume fraction at $U = 0.16\,\mathrm{m\,s^{-1}}$ in McClure asymmetric (left) symmetric and (right) configuration.

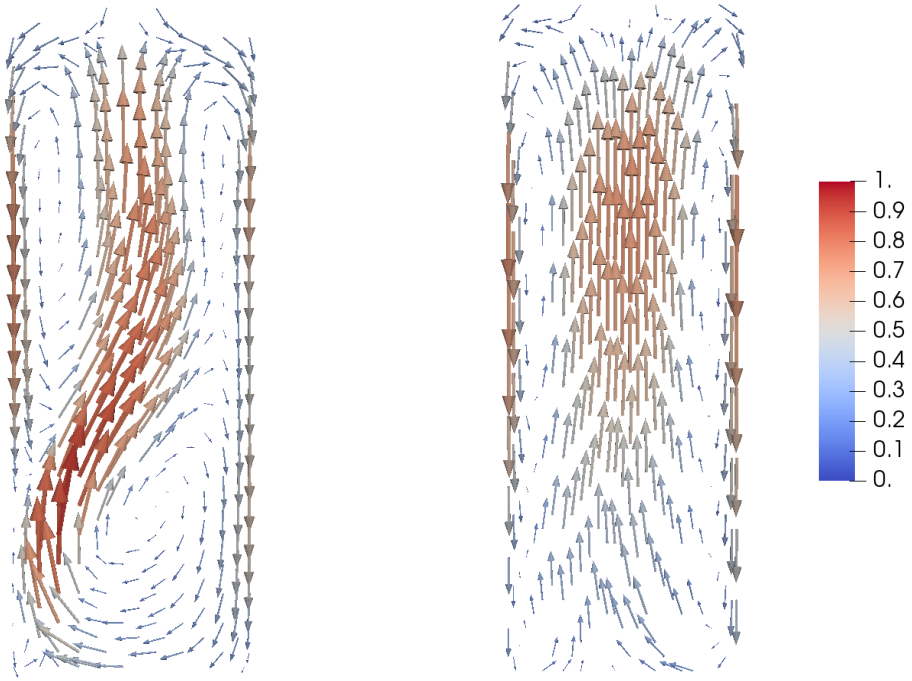

Figure 7.10: Vector plots of the time-averaged liquid velocity ($\mathrm{m\,s^{-1}}$), depicted accordingly to its magnitude, at $U = 0.16\,\mathrm{m\,s^{-1}}$ in McClure asymmetric (left) and symmetric (right) configuration.

The asymmetric system was then further simulated adopting the LES Smagorinksy-Zhang model and, in the first place, activating the lift force using Tomiyama correlation for C_L, reported in Eq. (2.29). Results, shown in Fig. 7.11 clearly indicate that, in systems where the gas is fed uniformly, the activation of the lift force has a low impact compared to the case where $C_L = 0$ with extremely marginal improvements in the prediction of the flow variables in such system: as an example, Fig. 7.11 reports the results of the symmetrically-fed McClure configuration.
However, the most interesting results come from the comparison performed in the asymmetrical conditions. Instead of improving the quality of the results, the activation of the lift force even leads to serious miscalculations of both the gas fraction and liquid z-velocity profiles. The radial profiles calculated with the implementation of the lift force sensibly differ from the experimental measurements, if they are compared with the uniformly-fed systems. This is related to the fact that the lift force strongly pushes the bubbles towards the wall of the aerated half column in a non-physical manner, suggesting that the correlation developed by Tomiyama for the lift coefficient leads to an incorrect calculation of this interfacial force. In fact, the prediction of the flow fields in the asymmetric column is satisfactory by the sole adoption of drag force and the swarm correction as interfacial force, the LES Smagorinsky-Zhang turbulence model and the linear blending approach, hence without any additional secondary interfacial force such as the lift.
Nonetheless, it should be stressed that the correlation developed by Tomiyama for the lift force coefficient broadly depends on the bubble Eötvös number and, therefore, on the bubble diameter d_b: in particular, for the range of bubble diameter here used, the dependence is particularly strong and a little change in the bubble size may have an impact on the sign of C_L and, consequentially, on the direction of the lift force, which may point either toward the center of the column or toward the walls. As example, in the set-up of Gemello, with $d_b = 6.5\,\mathrm{mm}$, $C_\mathrm{L} = 0.03$ while, in the McClure configurations, $d_b = 7.5\,\mathrm{mm}$ yields $C_\mathrm{L} = -0.14$. In order to discard this potential bias, the partially aerated system was also simulated using constant lift coefficients, ranging from -0.2 to +0.2.
The results (Fig. 7.11) confirmed again that the lift force is not suitable to be taken into account for the studied systems in this computational framework. In particular, the usage of the Tomiyama lift coefficient clearly overpredicts the lateral motion of the bubbles, as well as the adoption of a positive constant lift coefficient. On the other hand, negative values of C_L produce better results, but still far from the experimental measurements. To conclude, it can be said that the activation of the lift force alone, in the simulation of large bubble columns and using the model here presented (LES turbulence framework and phases blending approach with fixed bubble diameter), does not lead to a significant improvement of the results, regardless of the value used for the lift coefficient C_L. As suggested in Section 5.3.4, this outcome could also be ascribed to the activation of the sole lift force, hence the lack of other transverse forces, such as the turbulent dispersion

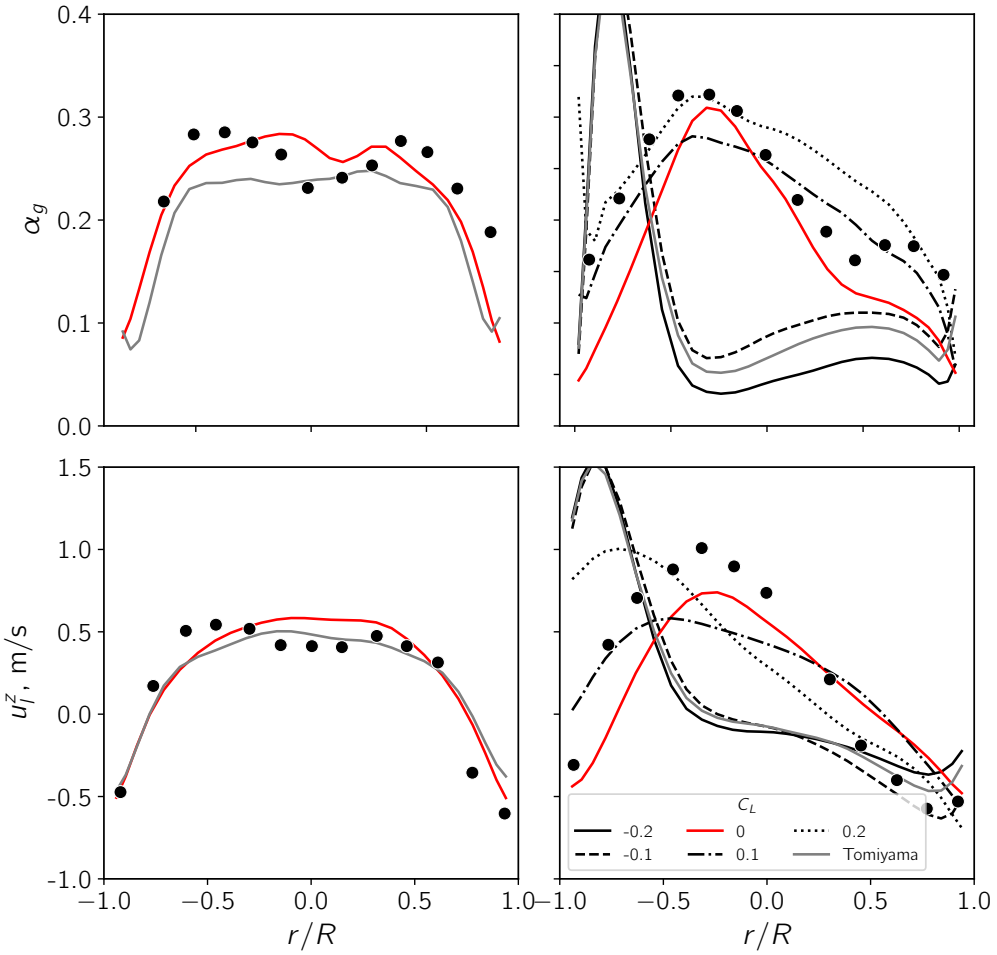

Figure 7.11: Effect of the lift force coefficient at $U = 0.16\,\mathrm{m\,s^{-1}}$ in McClure symmetrical (left) and asymmetrical (right) configuration at $z = 0.415\,\mathrm{m}$ and comparison with experimental data (circles). Time-averaged radial profiles of the gas fraction (top) and the axial liquid velocity (bottom).

force, balancing the lift force might contribute to the mispredition of the flow patterns. However, this point is worthy of deeper investigation in the future, under the perspective of the definitive assessment of the role of the lift force.

7.3.4 Extension to transitional and homogeneous regime

The results above discussed are all related to simulations performed at $U = 0.16\,\mathrm{m\,s^{-1}}$, which corresponds to a fully developed turbulent flow if the column diameter is equal to 0.39 or 0.4 m [213]. In this condition the agitation is intense and the interactions between bubbles, that may lead either to breakage or coalescence, occur in the whole air-in-water dispersion. However, when the gas superficial velocity is reduced, the system reaches back the pure homogeneous regime, where, as explained in Chapter 1, the degree if agitation is lower and bubbles interact more rarely than in the heterogeneous regime. Hence, to assess the validity of the model in the homogeneous and transition hydrodynamic regimes as well, the Gemello set-up was further investigated at lower gas superficial velocity U and, in particular, at $0.03\,\mathrm{m\,s^{-1}}$ and $0.09\,\mathrm{m\,s^{-1}}$, corresponding approximately to homogeneous and transition regime respectively. Fig. 7.12 summarizes the radial profiles of the time averaged α_g and u_l^z. The Smagorinsky-Zhang LES model coupled with the blending approach proved again a good capability of prediction, even at these lower superficial velocity, conferming the outcome of the corresponding RANS k-ε simulations performed for the same setup and discussed in Chapter 5.
To further strengthen the wide range of applicability of this model, the global gas hold-up, Φ, which is the average percentage of volume increase in the air-water system compared to the initial air-free volume of water (Eq. (1.1)), is calculated and then compared to experimental data or values computed from general correlations. The value of Φ is experimentally determined according to the difference in liquid height before and after the gas injection [16] or through differential pressure method [67]. In the simulations here performed, the global hold-up is calculated as the ratio of the volume of the gas-liquid dispersion, identified by summing the total volume of the cells where the local time averaged α_g is larger than 0.8, and the initial volume of liquid. The comparison is performed in Fig. 7.13 for superficial gas velocities up to $0.20\,\mathrm{m\,s^{-1}}$ both for fully (Gemello) and partially aerated systems, also reporting the correlation for the global hold-up developed by Reilly et al. [214], which estimates Φ with a statistical approach using the data available in the literature for fully aerated columns with D larger than 0.15 m.
The prediction of the LES model are very accurate when the gas superficial velocity is smaller than $0.15\,\mathrm{m\,s^{-1}}$. Beyond this value the global gas hold-up is slightly underestimated by the model here presented. This could be due to the polydispersity of the system, which becomes more relevant as the gas velocity increases [215].

7.3.5 Computational performances

As performed in Section 5.3.5 for RANS simulations, the investigation of the computational demand of this model might provide interesting insides, being a point

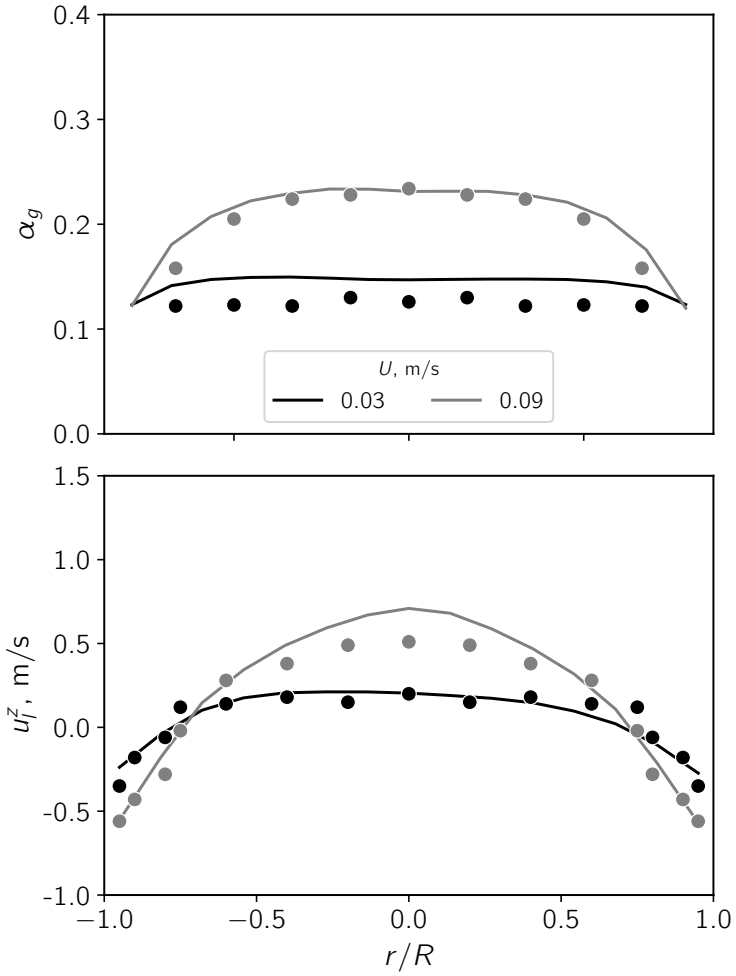

Figure 7.12: Effect of the hydrodynamical regime variation in Gemello column with Smagorinksy-Zhang LES turbulence model and comparison with experimental data (circles). Time-averaged radial profiles of the gas fraction at $z = 1$ m (top) and the liquid axial velocity at $z = 1.5$ m (bottom).

worthy of further studies. In fact, LES models are known to require larger computational resources compared with RANS. The main reason is that the bigger part of the turbulent spectrum is fully resolved by LES, while in RANS the turbulence is entirely modeled regardless of the considered length scale. Fig. 7.14 summarizes the computational time elapsed per 100 cells of domain for three investigated systems at $U = 0.16\,\mathrm{m\,s^{-1}}$, keeping mesh unchanged for both turbulence models,

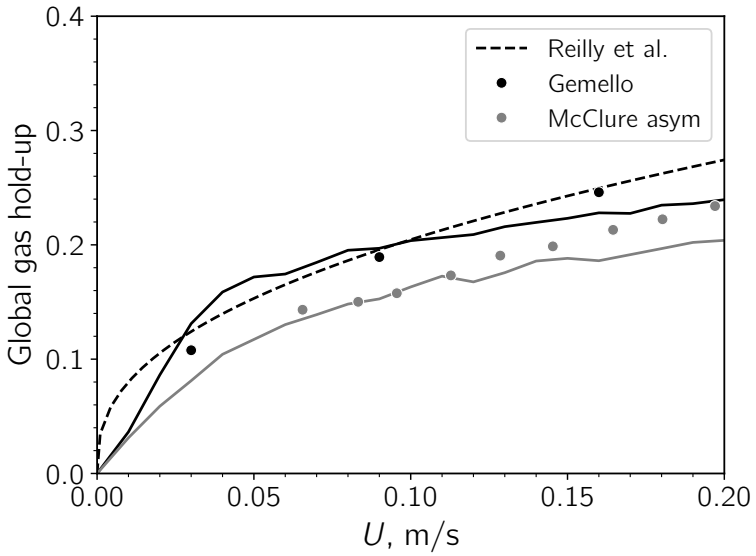

Figure 7.13: Global gas hold-up: comparison between Reilly correlation for fully aerated columns (dashed line), experiments (circles) and results obtained by using Smagorinsky-Zhang model (solid lines) for the fully aerated Gemello and partially aerated McClure asymmetrical systems.

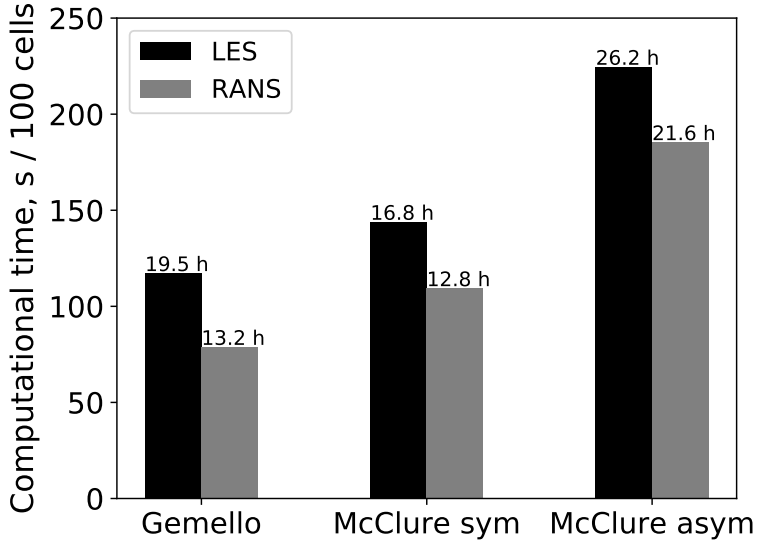

Figure 7.14: Elapsed computational time per 100 cells for the simulated system at $U = 0.16\,\mathrm{m\,s^{-1}}$ using 4 processing units Intel Xeon E5-2680 v3 2.50 GHz: comparison between standard k-ε (RANS) and Smagorinsky-Zhang (LES) models.

which are the standard k-ϵ model for the RANS and the Smagorinsky-Zhang for the LES approach. As expected, the latter showed an heavier computational demand compared with the former. Nonetheless, the increase in computational time detected when using the LES model is smaller than 50% in all the configurations. This drawback is highly compensated by the larger accuracy in the results provided by the Smagorinsky-Zhang model, especially for the partially aerated system where the difference of computational performances is the lowest and, at the same time, the discrepancy in the performances between the LES and RANS models is the highest.

7.3.6 CFD-PBM simulations

To conclude, we included the PBM in the present CFD model and it was implemented as described in Section 7.2.2. Fig. 7.15 compares the mean Sauter diameter obtained with LES Smagorinsky-Zhang and RANS standard k-ϵ models with experimental data sampled in Gemello set-up at $U = 0.03\,\mathrm{m\,s^{-1}}$. Once more it emerges the remarkable capability of the Smagorinsky-Zhang model to describe such bubbly flows, compared with the classical RANS approach. This outcome could be due to different reasons, related to the distinct calculation in the two models of the the characteristic flow variables such as gas fraction or liquid velocity as discussed above. However, the main reason should be looked for in the different prediction of the turbulence dissipation rate as highlighted in Fig. 7.5, whose field is an 'input' parameter for both coalescence and breakage kernel. Therefore, different estimations of the field of ϵ may lead to significant discrepancies in the prediction of the mean bubble diameter, as pointed out by Fig. 7.15 for the homogeneous regime and Fig. 7.16 for the heterogeneous regime.
In Section 7.2.2 it was mentioned that in the different hydrodynamical regimes the predominant phenomena involved in bubble coalescence may change, and therefore different coalescence kernels were used. Fig. 7.17 further confirms this hypothesis, showing that, if at low gas velocity the coalescence is modeled in the framework proposed by Wang, the predicted bubble diameter profiles sensibly diverge from the experimental data.
This is also confirmed at the heterogeneous regime, by performing the same simulation at $U = 0.16\,\mathrm{m\,s^{-1}}$, whose results are reported in Fig. 7.18. The outcome is reversed if compared to the homogeneous regime: the coupling of the Wang collision frequency and Lehr coalescence efficacy provided a notably more precise prediction of the mean Sauter diameter compared to Fig. 7.17.

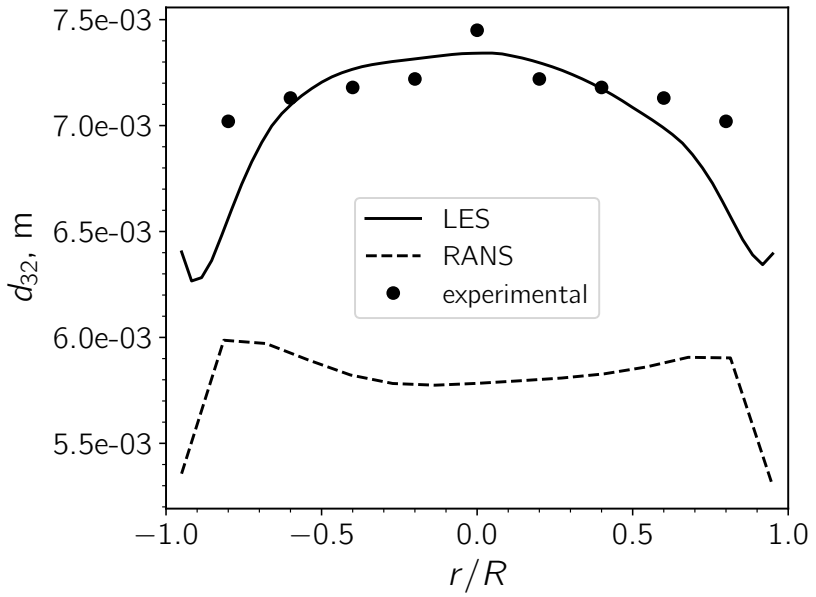

Figure 7.15: Time averaged radial profiles of the mean Sauter diameter at $z = 1\,\mathrm{m}$ and $U = 0.03\,\mathrm{m\,s^{-1}}$ in the Gemello set-up: comparison between LES Smagorinsky-Zhang model and RANS standard k-ϵ model.

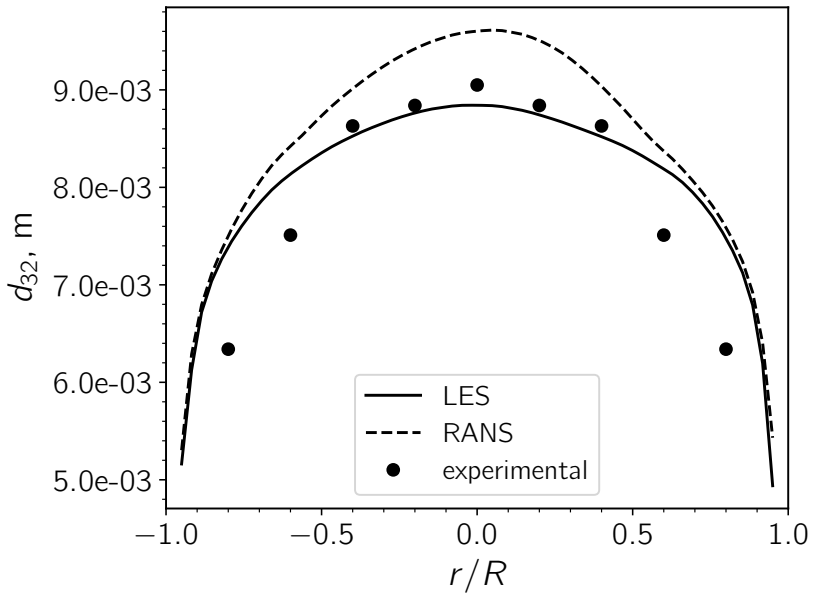

Figure 7.16: Time averaged radial profiles of the mean Sauter diameter at $z = 1\,\mathrm{m}$ and $U = 0.16\,\mathrm{m\,s^{-1}}$ in the Gemello set-up: comparison between LES Smagorinsky-Zhang model and RANS standard k-ϵ model.

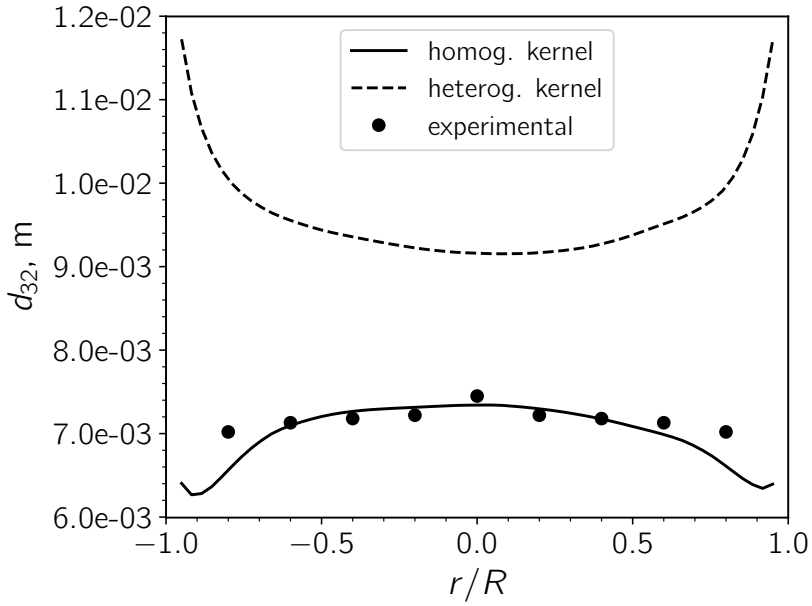

Figure 7.17: Time averaged radial profiles of the mean Sauter diameter at $z = 1\,\mathrm{m}$ and $U = 0.03\,\mathrm{m\,s^{-1}}$ in the Gemello set-up: comparison between coalescence kernels as described in Section Section 7.2.2.

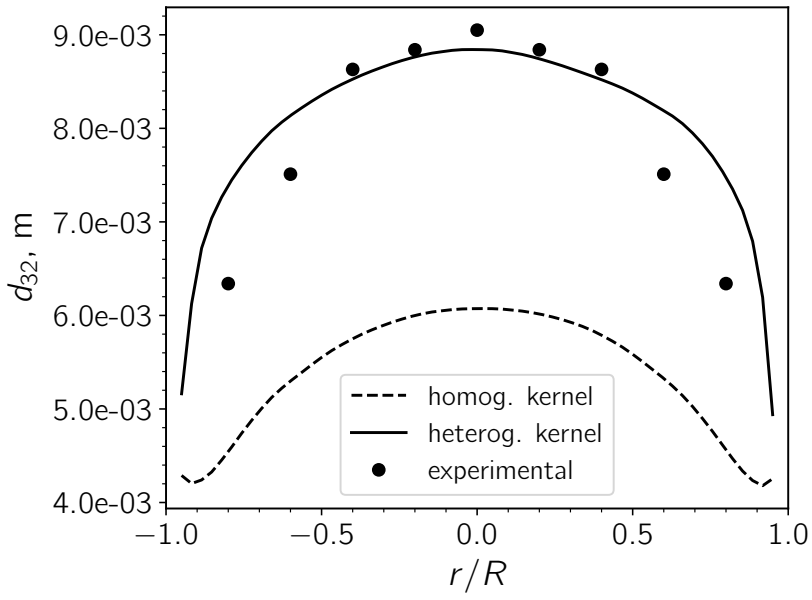

Figure 7.18: Time averaged radial profiles of the mean Sauter diameter at $z = 1\,\mathrm{m}$ and $U = 0.16\,\mathrm{m\,s^{-1}}$ in the Gemello set-up: comparison between coalescence kernels as described in Section 7.2.2.

7.4 Conclusions

LES turbulence models were successfully applied, in the framework of an Eulerian-Eulerian formulation, for the modeling of bubble columns. In particular, the LES description showed excellent performances in predicting the flow at both low and high gas velocity. To further maximize the validity of this approach, different operating conditions were tested, by simulating systems with symmetrical and non-symmetrical gas injection. LES model widely outperformed the classical RANS k-ϵ approach and, in particular, the formulation proposed by Smagorinsky for the computation of the subgrid turbulence viscosity, coupled with the inclusion of the BIT effects, presented the best results among the LES models.
The relevance of the lift force was then tested, with particular focus on the asymmetrical gas feed condition, being the configuration where this force was expected to be relevant at the most. To isolate the impact of the bubble diameter on the lift coefficient, constant values were used as well. Results showed that the inclusion of the lift force did not lead to an improvement of the result accuracy.
Finally, coupled CFD-PBM simulations were performed to assess the capability of the LES turbulence approach to estimate the bubble size distribution. The outcome revealed that, if the coalescence is properly modeling in accordance with the hydrodynamical regime, the Smagorinsky-Zhang model provides once more excellent ability to estimate the local mean bubble diameter, at both low and gas high velocity.
The successful coupling of PBM-LES simulations applied to bubbly flows may open new scenarios in the description of bubble columns. In the next chapter, as an example, it will be applied for the estimation of the mass transfer coefficient in a different experimental set-up.

Appendix: sensitivity the inlet conditions in PBM simulations

A further interesting point could be the investigation of how the boundary conditions of the PBM equations, i.e. the mean bubble size and the variance in the log-normal distribution imposed at inlet, impact on the evolution of the bubble diameter through the axial coordinate. We used experimental data of the column of Gemello in the homogeneous regime ($U = 0.03\,\mathrm{m\,s^{-1}}$)
Fig. 7.19 shows the axial profiles of d_{32} with different means and deviations μ set at the inlet section using the RANS k-ϵ approach. What emerges is that the inlet value of the Sauter diameter is highly relevant only in the bottom part of the column: after a distance approximately equal to the column diameter (which is also the length commonly recognized within the flow stabilizes), the variation with z is sensibly smaller. Morever, it can be identified a range of 'optimal' initial mean diameters, between 8 and 10 mm: within this interval, that includes the value experimentally observed, the axial evolution of d_{32} is extremely similar. Therefore, it can be concluded that, in the specification of the inlet conditions for the bubble diameter, a certain margin for error is allowed, at least in the homogeneous regime.

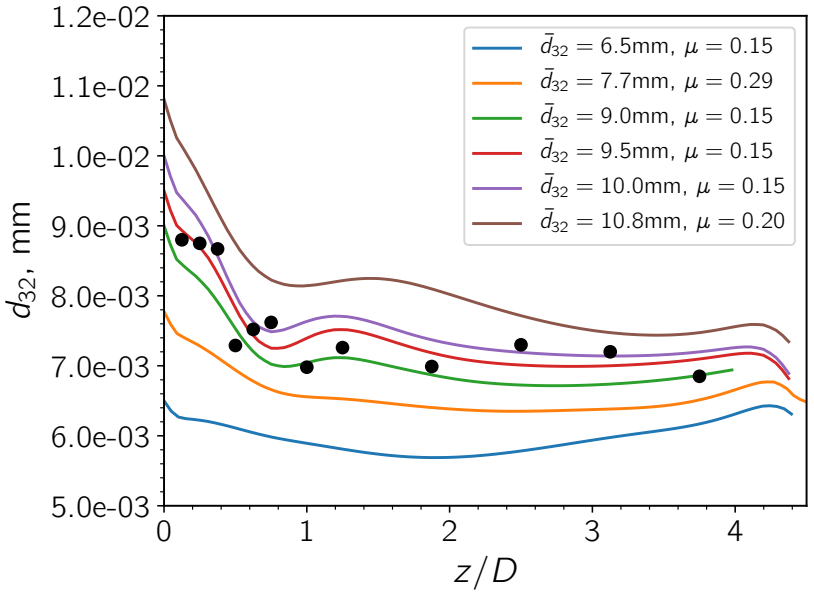

Figure 7.19: Time-averaged Sauter diameter axial profiles at $U = 0.03\,\mathrm{m\,s^{-1}}$ using RANS k-ϵ approach. Impact of the mean Sauter diameter ($\bar{d}_{32}$) and of the standard deviation (μ) of the log-normal distribution imposed at the inlet section.

Chapter 8

LES-PBM simulations for mass transfer estimation

In this chapter[1] the coupled LES-PBM model, described in Chapter 7, is adopted to investigate the fluid dynamics and quantify the mass transfer phenomenon in the square bubble column described in Section 4.4. In Chapter 6 it was discussed that the adoption of a RANS turbulence framework to describe square bubble columns could lead to numerical issues, whose solution requires further specific modeling assumptions. On the other hand, in this Chapter it is shown that the LES turbulence description allows to address these points without further assumptions on the secondary interfacial forces, using only the drag force, with the swarm correction, as interfacial forces, as performed for the cylindrical columns.
Moreover, the effect of the presence of small quantities of sodium dodecyl solfate (SDS) in the liquid phase is studied, with a particular focus on its effect on the bubble size distribution and mass transfer performances. In particular, the prediction of the mass transfer coefficient is a test to assess the quality of the population balance approach.

8.1 Introduction

The experimental work performed by Kouzbour et al. [202,203] investigated the role of surfactants, and of SDS in particular, on the gas hold up, bubble size and mass transfer coefficient for O_2 in the square bubble column described in Section 4.4, using gas superficial velocity up to $0.09\,\mathrm{m\,s^{-1}}$. It was reported that the addition

[1]This chapter is mainly based on the paper [203]: S. Kouzbour, F. Maniscalco, A. Buffo, M. Vanni, X. F. Grau, G. Bouchaib and Y. Stiriba, "Effects of SDS surface-active agents on hydrodynamics and oxygen mass transfer in a square bubble column reactor: Experimental and CFD modeling study" (to be submitted to *Chemical Engineering Science*).

of SDS, regardless of its concentration, leads to higher global gas hold-up, with a difference up to 25% compared with the experiments performed with water. This is probably due to the role of SDS in bubbles interactions, which inhibits coalescence and leads to a smaller average size of the bubbles, resulting in a larger gas hold-up. This phenomenon is also at the root of other main findings of the study: the mass transfer coefficient $k_l a_l$ is larger as the SDS is added in the heterogeneous regime. The impact of the addition of SDS to the liquid phase is actually twofold: on one side it decreases k_l because the corresponding oxygen diffusivity in water is lower, since the SDS molecules migrate toward the bubble-liquid interface, hindering the O_2 transfer from one phase to the other; on the other side, it increases a_l due to the inhibition of bubbles coalescence and, therefore, the lower mean bubble size. Among these two effects, the latter is predominant and, therefore, $k_l a_l$ increases in the contaminated systems.
In this Chapter, the LES-PBM model described in Chapter 7 is applied to assess its potential to predict the above phenomena.

8.2 Computational set-up

The simulations were performed using the computational grid described in Fig. 8.1. In particular, the same criterion discussed in Section 7.2 is followed, with the resulting cell size ranging from 6.8 to 14 mm
As done for the other set-ups, the sampled fields were time averaged after the flow reached the pseudo-stationary state: here the results presented in Section 8.3 were averaged over a time period equal to 60 s. The CFD model used in Chapter 7 is analogously applied: the only interfacial force considered is the swarm-corrected drag force, using the drag coefficient proposed by Tomiyama for partially contaminated air-water systems (Eq. (2.19)) and the Simonnet swarm factor (Eq. (2.24)). The phase blending is implemented as well, as described in Chapter 5.
Considering the investigated range of gas velocity, the PBM was implemented as done in Chapter 7 using the coalescence kernel valid for the homogeneous regime. Coherently, the mean diameter at the inlet was set accordingly to the values estimated by visual inspection of the experimental flows. In the QMOM algorithm, the six moments of the NDF were then calculated, as done in Section 7.3.6, by assuming a log-normal distribution with standard variation equal to 0.15. The boundary conditions and numerical schemes described in Chapter 5 and Chapter 7 are here adopted as well.
Furthermore, it could be argued that the presence of contaminants should be properly accounted in the coalescence and breakage kernels given their impact on the bubbles interface mobility [150] and the hindrance effect on the bubbles coalescence. However, the range of concentrations used for the SDS solutions, spanning from 0 to 30 ppm, is extremely low: hence here the effect of the contaminant is considered

only by reducing the interfacial tension γ, which was experimentally measured as function of the SDS concentration.
In the computational estimation of $k_l a_l$, k_l was calculated used the correlation proposed by Lamont and Scott (Eq. (3.3)) and the reduction of the oxygen diffusivity coefficient in water due to presence of SDS is extrapolated by the experimental measurements performed by Hebrard et al. [216]. The specific interfacial area a_l was computed from the LES-PBM simulations using Eq. (3.6).

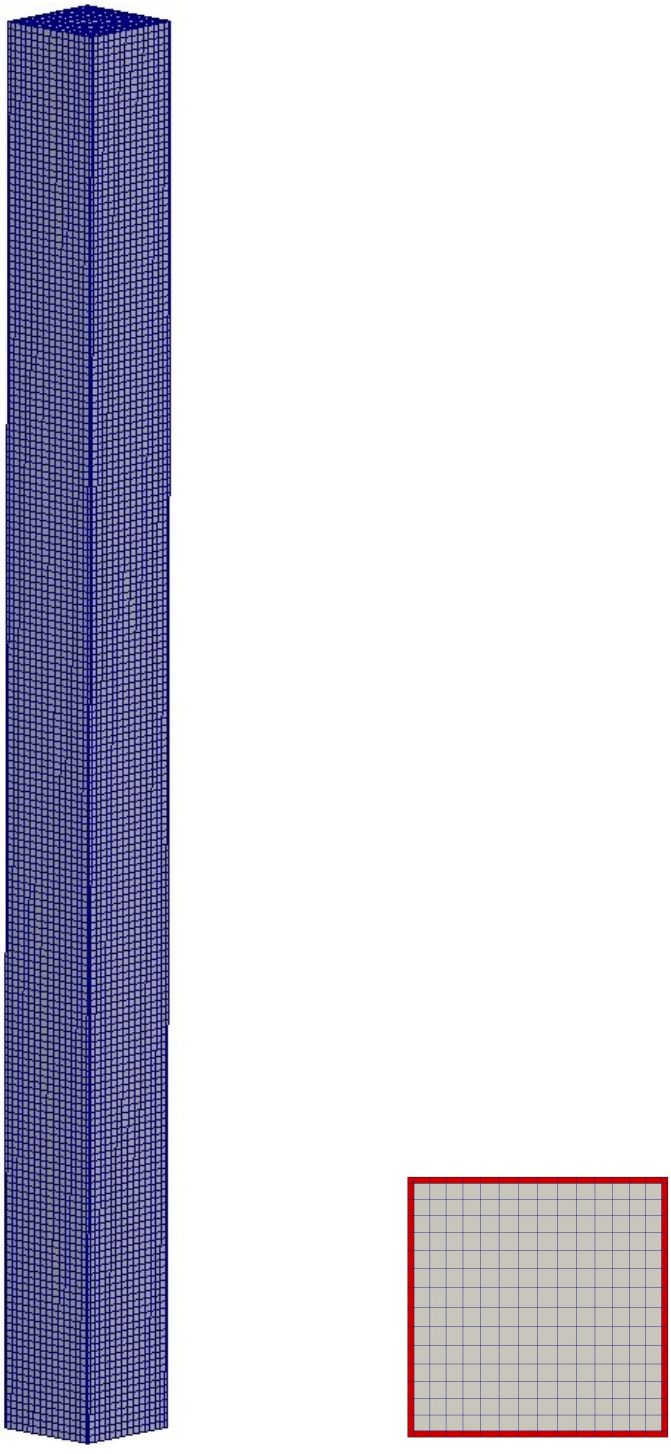

(a) (b)

Figure 8.1: Computational mesh used for LES simulation of Kouzbour set-up: (a) side view (the height is cut to 2.5 m), (b) bottom view. The red area is not included in the sparger.

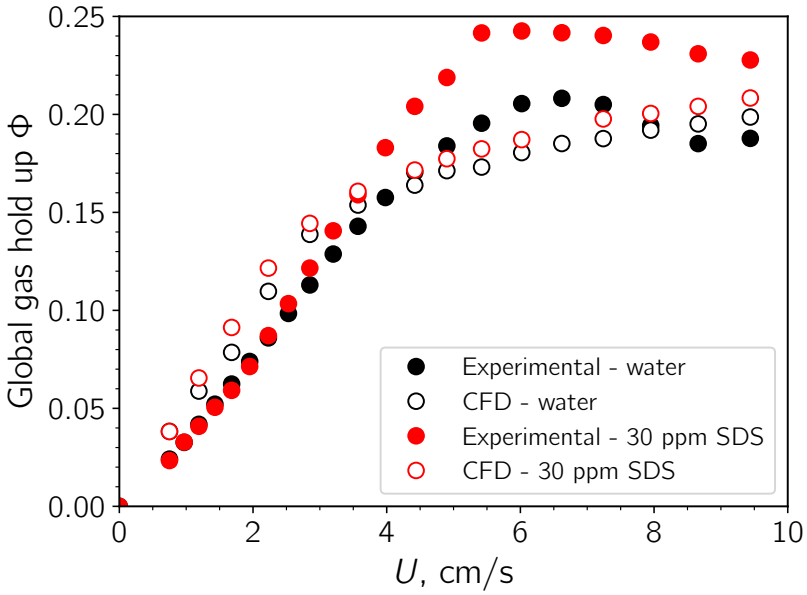

Figure 8.2: Global gas hold-up Φ obtained through LES-PBM simulation comparison with experimental measurements for air-water and air-SDS solution systems.

8.3 Results and discussion

Firstly, in order to assess the general validity of the CFD model, the global hold-up obtained adopting the LES Smagorinsky-Zhang model coupled with PBM equations was calculated for both systems (air-water and air-SDS solution) in a wide range of gas velocity. Fig. 8.2 reports the computational values of Φ as function of the superficial gas velocity U and compares them with the corresponding experimental measurements. It should be noted that the simulations performed using fixed diameter (i.e. without PBM equations) provided broadly similar values, and therefore they were not reported in this work.
A noteworthy difference between computational and experimental data may be detected in the early transition regime, while an overall good agreement is reached in the homogeneous regime and in the second part of the transition regime, which approaches the heterogeneous regime. Furthermore, the gas hold-up predicted for the contaminated system is larger than the corresponding value for air-water, in line with the experimental trends. Hence, these results confirm the suitability of the LES description to describe the flow in bubble columns with square section. This feature, further highlighted by the comparison of local profiles of α_g and u_l^z reported in Fig. 8.5, appears to be in contrast with the criticality reported in Chapter 6, arisen from the application of the RANS framework to the Ojima square bubble column. In that case, lift and wall lubrication forces had been necessarily accounted

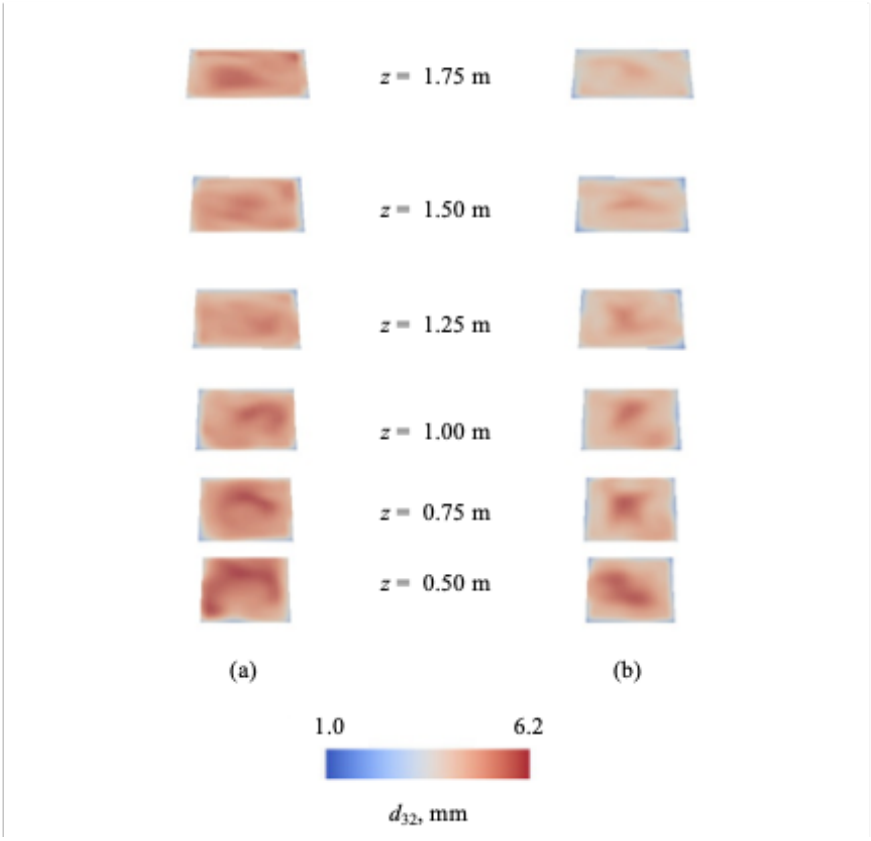

Figure 8.3: Instantaneous contour plots of Sauter mean diameter at $U = 7.95\,\mathrm{cm\,s^{-1}}$ for (a) tap water and (b) contaminated water with 30 ppm of SDS.

for, in addition to the drag force, to retain numerical stability and correctly estimate the flow. Therefore, the LES description here seems to overcome these issues, correctly modeling the flows with the same choice of interfacial forces (drag only with the swarm correction) used for the cylindrical systems.
Fig. 8.3 depicts the instantaneous field of the Sauter mean diameter d_{32} along the axial coordinate, calculated using the LES-PBM model, whether the liquid phase is water or a 30 ppm solution of SDS. What emerges is that the addition of the contaminant leads to a smaller average size of bubbles, which is in line with the experimental findings. In fact, SDS molecules are adsorbed preferentially at the bubble-liquid interface, reducing the interface mobility and hence hindering coalescence. In the computational model, this effect is taken into account by using the effective surface tension γ correlated to the mixture air-SDS solution used.
The impact of SDS is also detectable calculating the time averaged horizontal profiles of the volume gas fraction and liquid axial velocity and comparing them to results obtained using water as the continuous phase (Fig. 8.4). It can be noted that the presence of the contaminant has an effect on the liquid velocity field as

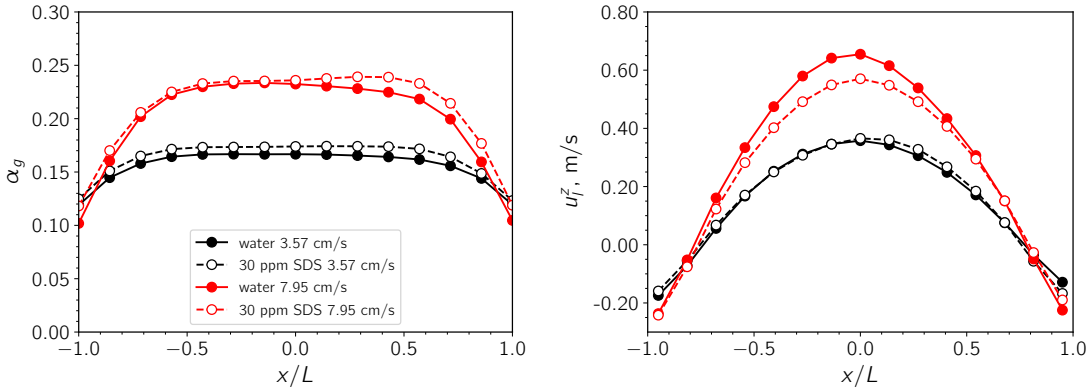

(a) (b)

Figure 8.4: Impact of contamination. Time averaged gas fraction (a) and liquid axial velocity (b) horizontal profiles obtained with CFD-PBM simulations at U = 3.57 and 7.95 cm s^{-1} and z = 1 m for tap water and contaminated water with 30 ppm of SDS.

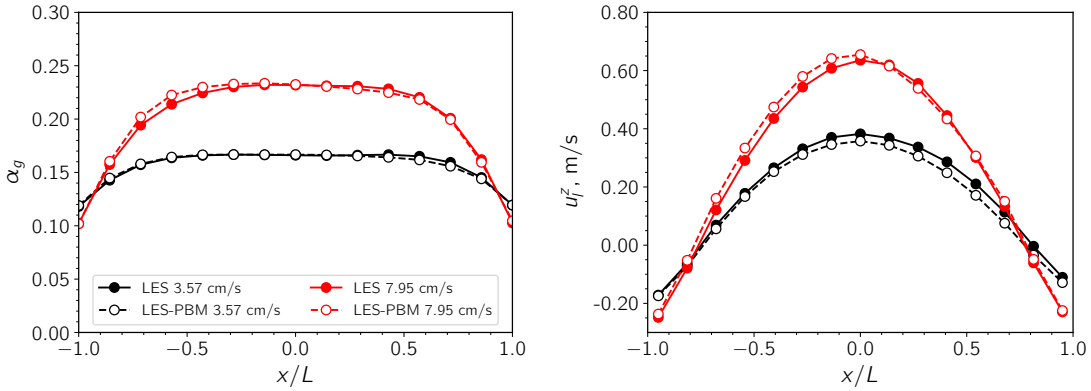

(a) (b)

Figure 8.5: Impact of population balance modeling. Time averaged gas fraction (a) and liquid axial velocity (b) horizontal profiles obtained with CFD simulations for the configuration with tap water at Ug = 3.57 and 7.95 cm s^{-1} and z = 1 m with and without population balance modeling.

well, especially at high gas velocity. This could be related to the aforementioned increase of gas hold-up which, in turn, is due to the presence of smaller bubbles. The resulting bubble crowding is then heavier, reducing the axial component of the liquid velocity: this is particularly evident at the center of the column.
However, focusing on the local field of the gas fraction and liquid axial velocity, the addition of the PBM model has a negligible impact on their prediction, as showed

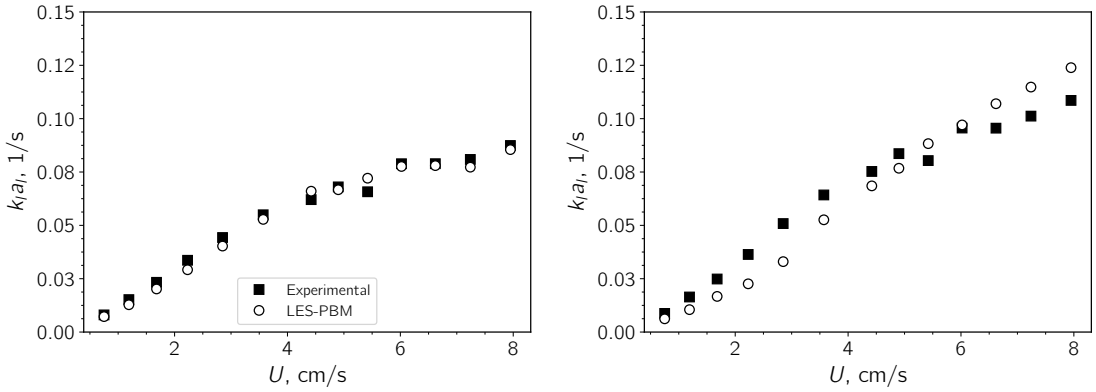

Figure 8.6: Estimation of the mass transfer coefficient through CFD-PBM simulations and comparison with experimental measurements for tap water at the bottom (a) and top (b) probe.

in Fig. 8.5, if the mean bubble diameter experimentally observed is used in each single case as fixed value.

8.3.1 $k_l a_l$ estimation

The local estimation of the mean bubble size, provided by the PBM equations, is crucial when the computation of the liquid side mass transfer coefficient $k_l a_l$ is pursued. In this perspective, the calculation of a_l is particularly straightforward, being related to the moment of the NDF of order two through Eq. (3.6), which is directly calculated by the QMOM algorithm.
Figs. 8.6 and 8.7 report the simulated and experimental mass transfer coefficient, respectively for the water-air and SDS solution - air systems, as functions of the gas superficial velocity. The sampling is computationally performed at the actual positions of the two oximeters, namely the bottom and top probe: therefore the $k_l a_l$ calculated with LES-PBM simulations is an average in the region of the domain corresponding to the experimental measurements.
It immediately stands out the growing trend of $k_l a_l$ with the gas superficial velocity. This is unquestionably related to the higher degree of agitation of the system, which is directly proportional to the velocity of the gas bubbles. This results in an increased surface renewal mobility and, therefore, in an enhancement of the mass transfer mechanisms.
Another aspect that emerges is that the mass transfer coefficient measured or calculated at the top probe is generally higher than the one detected by the bottom probe. This fact is due to the establishment of the flow patterns, which occurs along the axial direction. The distance between the sparger and the bottom probe

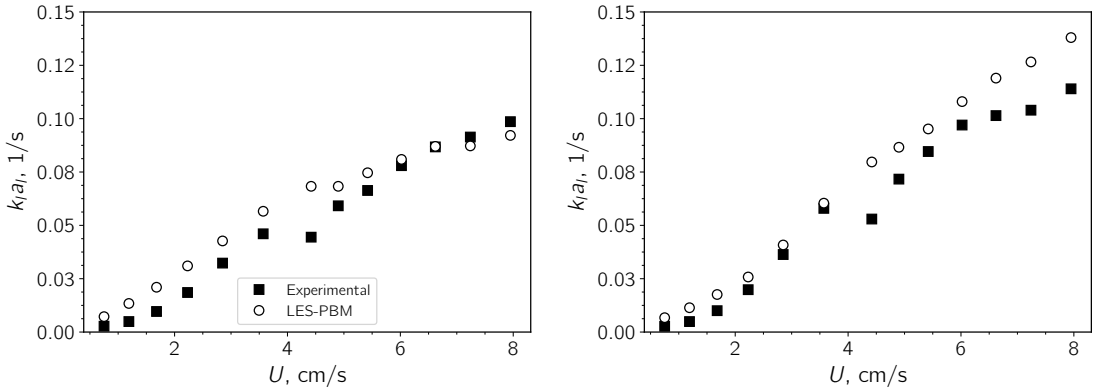

Figure 8.7: Estimation of the mass transfer coefficient through CFD-PBM simulations and comparison with experimental measurements for water contaminated with 30 ppm SDS at the bottom (a) and top (b) probe.

is only 0.11 m, lower than the the hydraulic diameter. The consequence is that this probe samples in a portion of space where the flow and the resulting agitation have not fully developed yet, inevitably resulting in lower values of $k_l a_l$. On the other hand, the top probe fetches data from a well developed region of the flow and therefore the relative mass transfer coefficients are higher.
Moreover, among the two opposite effects on $k_l a_l$ caused by the addition of SDS to the liquid phase mentioned in Section 8.1, i.e. the decrease of k_l due to the lower oxygen diffusivity and the increase of a_l due to the smaller average bubble size, the latter appears predominant from LES-PBM simulations, in line, again, with experimental measurements.
To conclude, it should be stressed the excellent potentiality of the computational model that computed $k_l a_l$ with marginal errors, regardless of the location of the probe or the composition of the liquid phase. This is further highlighted by Fig. 8.8, which compares in a parity plot experimental and computational values of the mass transfer coefficient.

8.4 Conclusions

The LES-PBM model discussed in Chapter 7 was successfully applied to a square bubble column to simulate the flow characteristics. Either water or a SDS solution is used as liquid phase, which is accounted for in the value of the gas-liquid surface tension.
In particular, since the model was applied without any additional adjustment or modification on the interfacial forces, the excellent results may suggest that it could

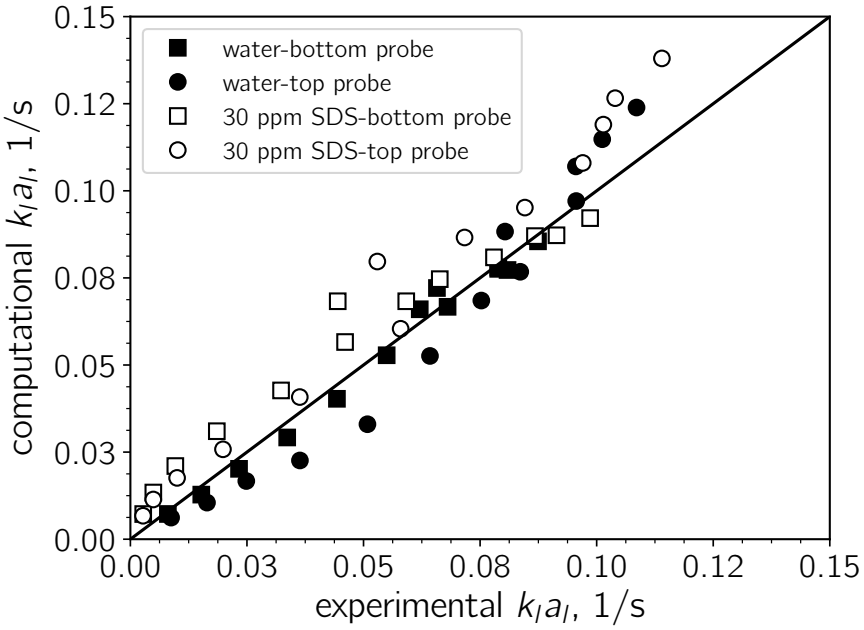

Figure 8.8: Parity plot of $k_l a_l$. Comparison of experimental measurements and computational estimations.

be used for slurry bubble columns as well, possibly solving the issues deriving from the application of a RANS turbulence description pointed out in Chapter 6.
The simulations confirmed the observed experimental trend consisting in a increasing gas hold-up with the addition of the contaminant due to the inhibition of bubbles coalescence and the resulting reduction of their average diameter.
The implementation of a PBM model allowed to assess the bubble size distribution and well contributed to the prediction of the flows. However, the most relevant contribution of this implementation is the correct estimation of the bubbles interface area and therefore, of $k_l a_l$. In fact, the proposed model showed its considerable capacity of quantifying the oxygen mass transfer mechanism with particularly high precision, as suggested by the comparison with experimental data.

Chapter 9

Final remarks

This work attempted to shred some lights on several aspects of the modeling of bubble columns, following the spirit of the latest trends in the scientific research, whose ambitious aim is to reach a single model valid for the widest range of geometries and operating conditions. In this perspective, multiple operating conditions and experimental set-ups were chosen for data comparison and model validation to maximize the validity of the latter.
It was showed that a proper modeling of phase interactions and phase inversion is crucial to achieve stability in the numerical simulations. In particular, a fine modeling of the phase blending, capable to distinguish locally the continuous and dispersed phases, was discussed and a detailed tuning of its parameters was performed. This blending modeling equaled the performances of other models relying on fitting parameters based on a particular test case, and, at the same time, reported an additional speed up of the simulation time up to 50%. The blending model, first analyzed in a framework of a RANS description of the turbulence, was then successfully applied to LES simulation as well.
Afterwards, a three phase square bubble column was investigated adopting the RANS turbulence description. Given the small size of the solid particles, the solid-liquid mixture was described in accordance with the pseudo-homogeneous model. The particular geometry of the column required the activation of secondary interfacial forces such as the lift and the wall lubrication force. Nevertheless, the final prediction of the local gas fraction, tested up to a solid loading equal to 20%, was undoubtedly satisfactory. Secondarily, it was also tested the efficacy of a PBM implementation, accounting for the impact of solid particles on the bubbles interactions. However, this did not lead to a significant improvement of the quality of the results.
Moreover, the aforementioned LES turbulence approach was used to describe the flow in cylindrical bubble columns at high gas superficial velocity and with different conditions of gas injection. Results showed that the Smagorinsky model for the calculations of the subgrid-scale turbulent viscosity, coupled with the inclusion of

a BIT viscosity as well, provided an excellent estimation of the flows in all the studied operating conditions, especially if compared to the RANS approach. This outcome is particularly noticeable in the operating conditions where the gas is fed only trough one half of the sparger.
In both RANS and LES simulations the impact of the activation of the lift force was assessed. When the gas is fed uniformly, there is no significant improvement of the quality in the prediction of the flow. On the other hand, in the asymmetrical feed conditions, the inclusion of this force led to serious miscalculations of the flow variables, regardless of the value of the lift coefficient.
The Smagorinsky-Zhang model was then coupled to a PBM implementation to evaluate the local distribution of the mean bubble diameter as well, in both homogeneous and heterogeneous regimes. In particular, while both bubbles breakage and collision frequencies were assumed to be mainly related to turbulent fluctuations, the coalescence efficiency adopted in the PBM kernels is based on the drainage time of the liquid film trapped the colliding bubbles for the homogeneous regime, and on the relative velocity of the colliding bubbles for the heterogeneous regime. These assumptions led to an optimal estimation of the Sauter diameter compared to experimental data.
Additionally, the LES-PBM model was used to evaluate the fluid dynamics and the mass transfer coefficient in a square bubble column, with and without small concentration of SDS. The model successfully reproduced the observed experimental behavior and, in particular, the impact of the SDS on the mass transfer coefficient, which was increased by the addition of the contaminant because the latter hinders coalescence and leads to smaller bubbles, eventually corresponding to a larger specific interfacial area. In particular, the PBM-LES description was able to predict $k_l a_l$ with a remarkably small error percentage.
Considering the outcome of this work, a future development could be the application of the LES-PBM model to the description of slurry bubble columns. It was shown in Chapter 6 that the adoption of the RANS framework to describe turbulence in square bubble columns generated nonphysical results and numerical issues at the four corners of the section. The inclusion of secondary interfacial forces, the lift force and, especially, the wall lubrication force, was then crucial to address, at least partially, these points. On the other side, the simulations performed within the LES description of the square column analyzed in Chapter 8 did not present any numerical issues at the corners of the section. This outcome suggests that the computational instabilities detected in Chapter 6 were probably generated by the RANS models of the turbulence, regardless of the presence of the solid particles in the liquid phase. Therefore, it would be valuable to evaluate if the LES approach could solve these issues when the presence of solid particles is included as well.
Moreover, the results arisen from the inclusion of the lift force and bubble induced turbulence effect suggest that the future research should focus more on their actual relevance, with the aim of thoroughly assess the respective role and importance in

both numerical and physical terms. In this perspective, the achievement of a final and conclusive evaluation of these phenomena is advisable and, in this light, this doctoral dissertation provided new insights for the forthcoming studies in this field.

Nomenclature

Latin symbols

$\boldsymbol{S}$	strain of rate tensor	s^{-1}
$\boldsymbol{g}$	gravitational acceleration	$\mathrm{m\,s}^{-2}$
$\boldsymbol{u}$	velocity	$\mathrm{m\,s}^{-1}$
C_D	drag coefficient	-
C_L	lift coefficient	-
C_s	volumetric solid loading	-
D	column diameter	m
D_{in}	sparger diameter	m
D_H	hydraulic diameter	m
E_in	power input due to gas injection	W
E_t	volume integral of turbulence dissipation rate	W
H_t	column height	m
H_0	liquid static height	m
I	identity matrix	-
R	column radius	m
U	gas superficial velocity	$\mathrm{m\,s}^{-1}$
a_l	air-liquid interface area per volume	m^{-1}
d_{32}	Sauter bubble diameter	m
d_b	bubble diameter	m
d_s	particle diameter	m
h	swarm factor	-
k	turbulent kinetic energy	$\mathrm{m}^2\,\mathrm{s}^{-2}$
k_l	liquid side mass transfer coefficient	$\mathrm{m\,s}^{-1}$
p	pressure	Pa
r	radial coordinate	m
z	axial coordinate (distance from the sparger)	m

Greek symbols

Δ	LES filter length	m
Φ	Global gas hold-up	-
$\boldsymbol{\sigma}$	stress tensor	Pa
$\boldsymbol{\omega}$	vorticity	s^{-1}
α	volume fraction	-
γ	surface tension	$N\,m^{-1}$
ϵ	turbulence dissipation rate	$m^2\,s^{-3}$
μ	dynamic viscosity	$Pa\,s$
ν	kinematic viscosity	$Pa\,s$
ρ	density	$kg\,m^{-3}$

Subscripts

FD	fully dispersed
PD	partially dispersed
TD	turbulent dispersion
VM	virtual mass
WL	wall lubrication
eff	effective
lam	laminar
g	gas
l	liquid
res	resolved scale
t	turbulent

Acronyms

BIT	bubble induced turbulence
CFD	computational fluid dynamics
DSD	daughter size distribution
LES	large eddy simulation
PBM	population balance modeling
RANS	Reynolds averaged Navier-Stokes
SDS	sodium dodecyl solfate
SGS	sub-grid scale

Dimensionless numbers

Re_b	bubble Reynolds number	$u_l d_b \rho_l / \mu_l$
Eo_b	bubble Eötvös number	$(\rho_l - \rho_g) g d_b^2 / \gamma$

Bibliography

[1] P. Rollbusch, M. Bothe, M. Becker, M. Ludwig, M. Grünewald, M. Schlüter, and R. Franke, "Bubble columns operated under industrially relevant conditions–current understanding of design parameters," *Chemical Engineering Science*, vol. 126, pp. 660–678, 2015.

[2] V. N. Lima, C. S. Rodrigues, R. A. Borges, and L. M. Madeira, "Gaseous and liquid effluents treatment in bubble column reactors by advanced oxidation processes: A review," *Critical Reviews in Environmental Science and Technology*, vol. 48, no. 16-18, pp. 949–996, 2018.

[3] K. O. U. Nigar Kantarci, Fahir Borak, "Bubble column reactors," *Process Biochemistry*, vol. 40, no. 7, pp. 2263–2283, 2015.

[4] O. M. Basha, L. Sehabiague, A. Abdel-Wahab, and B. I. Morsi, "Fischer-Tropsch synthesis in slurry bubble column reactors: experimental investigation and modeling - a review," *International Journal of Chemical Reactor Engineering*, vol. 15, no. 3, pp. 201–288, 2015.

[5] A. Cybulski, "Liquid-phase methanol synthesis: catalysts, mechanism, kinetics, chemical equilibria, vapor-liquid equilibria, and modeling—a review," *Catalysis Reviews—Science and Engineering*, vol. 36, no. 4, pp. 557–615, 1994.

[6] L. Gemello, C. Plais, F. Augier, A. Cloupet, and D. L. Marchisio, "Hydrodynamics and bubble size in bubble columns: Effects of contaminants and spargers," *Chemical Engineering Science*, vol. 184, pp. 93–102, 2018.

[7] W.-D. Deckwer, Y. Louisi, A. Zaidi, and M. Ralek, "Hydrodynamic properties of the Fischer-Tropsch slurry process," *Industrial & Engineering Chemistry Process Design and Development*, vol. 19, no. 4, pp. 699–708, 1980.

[8] G. Besagni, F. Inzoli, T. Ziegenhein, and D. Lucas, "Computational Fluid-Dynamic modeling of the pseudo-homogeneous flow regime in large-scale bubble columns," *Chemical Engineering Science*, vol. 160, pp. 144–160, 2017.

[9] S. Mahmoudi and M. W. Hlawitschka, "Effect of solid particles on the slurry bubble columns behavior – a review," *ChemBioEng Reviews*, vol. 9, no. 1, pp. 63–92, 2022.

[10] M. V. Tabib, S. A. Roy, and J. B. Joshi, "CFD simulation of bubble column-an analysis of interphase forces and turbulence models," *Chemical Engineering*

Journal, vol. 139, pp. 589–614, 2008.

[11] M. Pourtousi, J. N. Sahu, and P. Ganesan, "Effect of interfacial forces and turbulence models on predicting flow pattern inside the bubble column," *Chemical Engineering and Processing: Process Intensification*, vol. 75, pp. 38–47, 2014.

[12] D. Pfleger and S. Becker, "Modelling and simulation of the dynamic flow behaviour in a bubble column," *Chemical Engineering Science*, vol. 56, no. 4, pp. 1737–1747, 2001. 16th International Conference on Chemical Reactor Engineering.

[13] P. Chen, M. P. Duduković, and J. Sanyal, "Three-dimensional simulation of bubble column flows with bubble coalescence and breakup," *AIChE Journal*, vol. 51, no. 3, pp. 696–712, 2005.

[14] J. Sanyal, D. L. Marchisio, R. O. Fox, and K. Dhanasekharan, "On the comparison between population balance models for CFD simulation of bubble columns," *Industrial & Engineering Chemistry Research*, vol. 44, no. 14, pp. 5063–5072, 2005.

[15] C. Laborde-Boutet, F. Larachi, N. Dromard, O. Delsart, and D. Schweich, "CFD simulation of bubble column flows: Investigations on turbulence models in RANS approach," *Chemical Engineering Science*, vol. 64, pp. 4399–4413, 2009.

[16] L. Gemello, V. Cappello, F. Augier, D. Marchisio, and C. Plais, "CFD-based scale-up of hydrodynamics and mixing in bubble columns," *Chemical Engineering Research and Design*, vol. 136, pp. 846–858, 2018.

[17] N. G. Deen, T. Solberg, and B. H. Hjertager, "Large eddy simulation of the gas-liquid flow in a square cross-sectioned bubble column," *Chemical Engineering Science*, vol. 56, pp. 6341–6349, 2001.

[18] M. T. Dhotre, N. G. Deen, B. Niceno, Z. Khan, and J. B. Joshi, "Large eddy simulation for dispersed bubbly flows: A review," *International Journal of Chemical Engineering*, vol. 2013, 2013.

[19] M. H. Mohammadi, F. Sotiropoulos, and J. R. Brinkerhoff, "Eulerian-eulerian large eddy simulation of two-phase dilute bubbly flows," *Chemical Engineering Science*, vol. 208, p. 115156, 2019.

[20] M. Bhole, J. Joshi, and D. Ramkrishna, "CFD simulation of bubble columns incorporating population balance modeling," *Chemical Engineering Science*, vol. 63, 4 2008.

[21] V. V. Buwa and V. V. Ranade, "Dynamics of gas–liquid flow in a rectangular bubble column: experiments and single/multi-group CFD simulations," *Chemical Engineering Science*, vol. 57, pp. 4715–4736, 11 2002.

[22] D. Lakehal, B. L. Smith, and M. Milelli, "Large-eddy simulation of bubbly turbulent shear flows," *Journal of Turbulence*, vol. 3, 2002.

[23] D. Zhang, N. Deen, and J. Kuipers, "Numerical simulation of the dynamic flow behavior in a bubble column: A study of closures for turbulence and

interface forces," *Chemical Engineering Science*, vol. 61, 12 2006.

[24] M. E. Díaz, A. Iranzo, D. Cuadra, R. Barbero, F. J. Montes, and M. A. Galán, "Numerical simulation of the gas-liquid flow in a laboratory scale bubble column. Influence of bubble size distribution and non-drag forces," *Chemical Engineering Journal*, vol. 139, pp. 363–379, 6 2008.

[25] A. A. Kulkarni, "Lift force on bubbles in a bubble column reactor: experimental analysis," *Chemical Engineering Science*, vol. 63, no. 6, pp. 1710–1723, 2008.

[26] B. Selma, R. Bannari, and P. Proulx, "Simulation of bubbly flows: Comparison between direct quadrature method of moments (DQMOM) and method of classes (CM)," *Chemical Engineering Science*, vol. 65, no. 6, pp. 1925–1941, 2010.

[27] M. K. Silva, M. A. D'Ávila, and M. Mori, "Study of the interfacial forces and turbulence models in a bubble column," *Computers and Chemical Engineering*, vol. 44, pp. 34–44, 9 2012.

[28] M. V. Tabib and P. Schwarz, "Quantifying sub-grid scale (SGS) turbulent dispersion force and its effect using one-equation SGS large eddy simulation (LES) model in a gas–liquid and a liquid–liquid system," *Chemical Engineering Science*, vol. 66, pp. 3071–3086, 7 2011.

[29] D. D. McClure, H. Norris, J. M. Kavanagh, D. F. Fletcher, and G. W. Barton, "Validation of a computationally efficient computational fluid dynamics (CFD) model for industrial bubble column bioreactors," *Industrial & Engineering Chemistry Research*, vol. 53, no. 37, pp. 14526–14543, 2014.

[30] M. G. Fard, Y. Stiriba, B. Gourich, C. Vial, and F. X. Grau, "Euler-Euler large eddy simulations of the gas–liquid flow in a cylindrical bubble column," *Nuclear Engineering and Design*, vol. 369, p. 110823, 2020.

[31] R. Hansen, *Computational and experimental study of bubble size in bubble columns*. Esbjerg Institute of Technology, Aalborg University, 2009.

[32] A. Gupta and S. Roy, "Euler–Euler simulation of bubbly flow in a rectangular bubble column: Experimental validation with radioactive particle tracking," *Chemical Engineering Journal*, vol. 225, pp. 818–836, 2013.

[33] G. Li, X. Yang, and G. Dai, "CFD simulation of effects of the configuration of gas distributors on gas–liquid flow and mixing in a bubble column," *Chemical Engineering Science*, vol. 64, no. 24, pp. 5104–5116, 2009.

[34] X. Guo and C. Chen, "Simulating the impacts of internals on gas–liquid hydrodynamics of bubble column," *Chemical Engineering Science*, vol. 174, pp. 311–325, 2017.

[35] E. Olmos, C. Gentric, and N. Midoux, "Numerical description of flow regime transitions in bubble column reactors by a multiple gas phase model," *Chemical Engineering Science*, vol. 58, no. 10, pp. 2113–2121, 2003.

[36] M. Simonnet, C. Gentric, E. Olmos, and N. Midoux, "Cfd simulation of the

flow field in a bubble column reactor: Importance of the drag force formulation to describe regime transitions," *Chemical Engineering and Processing: Process Intensification*, vol. 47, no. 9-10, pp. 1726–1737, 2008.

[37] D. D. McClure, H. Norris, J. M. Kavanagh, D. F. Fletcher, and G. W. Barton, "Towards a cfd model of bubble columns containing significant surfactant levels," *Chemical Engineering Science*, vol. 127, pp. 189–201, 2015.

[38] K. Ekambara and M. T. Dhotre, "CFD simulation of bubble column," *Nuclear Engineering and Design*, vol. 240, pp. 963–969, 2010.

[39] A. Buffo, D. L. Marchisio, M. Vanni, and P. Renze, "Simulation of polydisperse multiphase systems using population balances and example application to bubbly flows," *Chemical Engineering Research and Design*, vol. 91, pp. 1859–1875, 2013.

[40] A. Buffo, M. Vanni, P. Renze, and D. L. Marchisio, "Empirical drag closure for polydisperse gas–liquid systems in bubbly flow regime: Bubble swarm and micro-scale turbulence," *Chemical Engineering Research and Design*, vol. 113, pp. 284–303, 2016.

[41] L. Gemello, C. Plais, F. Augier, and D. L. Marchisio, "Population balance modelling of bubble columns under the heterogeneous flow regime," *Chemical Engineering Journal*, vol. 372, pp. 590–604, 2019.

[42] S. Long, J. Yang, X. Huang, G. Li, W. Shi, M. Sommerfeld, and X. Yang, "Large-eddy simulation of gas–liquid two-phase flow in a bubble column reactor using a modified sub-grid scale model with the consideration of bubble-eddy interaction," *International Journal of Heat and Mass Transfer*, vol. 161, p. 120240, 2020.

[43] R. Rzehak and E. Krepper, "CFD modeling of bubble-induced turbulence," *International Journal of Multiphase Flow*, vol. 55, pp. 138–155, 10 2013.

[44] A. Vaidheeswaran and T. Hibiki, "Bubble-induced turbulence modeling for vertical bubbly flows," *International Journal of Heat and Mass Transfer*, vol. 115, pp. 741–752, 2017.

[45] F. Maniscalco, M. Shiea, A. Buffo, D. Marchisio, and M. Vanni, "Performance of the blending factor approach for modeling the interfacial forces in bubble columns operating at high gas hold up," in *Proceedings from the 14th International Conference on CFD in Oil & Gas, Metallurgical and Process Industries* (S. A. Press, ed.), pp. 64–71, 2020.

[46] M. Shiea, A. Buffo, M. Vanni, and D. Marchisio, "Numerical methods for the solution of population balance equations coupled with computational fluid dynamics," *Annual Review of Chemical and Biomolecular Engineering*, vol. 11, pp. 339–366, 6 2020.

[47] T. Wang, "Simulation of bubble column reactors using CFD coupled with a population balance model," *Frontiers of Chemical Science and Engineering*, vol. 5, no. 2, pp. 162–172, 2011.

[48] M. Sattar, J. Naser, and G. Brooks, "Numerical simulation of two-phase flow

with bubble break-up and coalescence coupled with population balance modeling," *Chemical Engineering and Processing: Process Intensification*, vol. 70, pp. 66–76, 2013.

[49] Y. Liu and O. Hinrichsen, "Study on CFD–PBM turbulence closures based on k–ϵ and reynolds stress models for heterogeneous bubble column flows," *Computers & Fluids*, vol. 105, pp. 91–100, 2014.

[50] X.-F. Liang, H. Pan, Y.-H. Su, and Z.-H. Luo, "CFD-PBM approach with modified drag model for the gas–liquid flow in a bubble column," *Chemical Engineering Research and Design*, vol. 112, pp. 88–102, 2016.

[51] N. Yang and Q. Xiao, "A mesoscale approach for population balance modeling of bubble size distribution in bubble column reactors," *Chemical Engineering Science*, vol. 170, pp. 241–250, 2017.

[52] B. Zhang, L. Kong, H. Jin, G. He, S. Yang, and X. Guo, "CFD simulation of gas–liquid flow in a high-pressure bubble column with a modified population balance model," *Chinese journal of chemical engineering*, vol. 26, no. 6, pp. 1350–1358, 2018.

[53] A. Aiyer, D. Yang, M. Chamecki, and C. Meneveau, "A population balance model for large eddy simulation of polydisperse droplet evolution," *Journal of Fluid Mechanics*, vol. 878, pp. 700–739, 2019.

[54] A. Aiyer and C. Meneveau, "Coupled population balance and large eddy simulation model for polydisperse droplet evolution in a turbulent round jet," *Physical Review Fluids*, vol. 5, no. 11, p. 114305, 2020.

[55] S. S. Rabha and V. V. Buwa, "Volume-of-fluid (VOF) simulations of rise of single/multiple bubbles in sheared liquids," *Chemical Engineering Science*, vol. 65, pp. 527–537, 1 2010.

[56] S. Ojima, K. Hayashi, and A. Tomiyama, "Effects of hydrophilic particles on bubbly flow in slurry bubble column," *International Journal of Multiphase Flow*, vol. 58, pp. 154–167, 2014.

[57] A. R. Sarhan, J. Naser, and G. Brooks, "Effects of particle size and concentration on bubble coalescence and froth formation in a slurry bubble column," *Particuology*, vol. 36, pp. 82–95, 2018.

[58] L.-S. Fan, O. Hemminger, Z. Yu, and F. Wang, "Bubbles in nanofluids," *Industrial & Engineering Chemistry Research*, vol. 46, no. 12, pp. 4341–4346, 2007.

[59] A. H. Syed, M. Boulet, T. Melchiori, and J. M. Lavoie, "CFD simulation of a slurry bubble column: Effect of population balance kernels," *Computers & Fluids*, vol. 175, pp. 167–179, 2018.

[60] W. Su, X. Shi, Y. Wu, J. Gao, and X. Lan, "Population balance model simulation of the particle effect on flow hydrodynamics in slurry beds," *Chemical Engineering & Technology*, vol. 42, no. 4, pp. 761–768, 2019.

[61] H. A. Jakobsen, H. Lindborg, and C. A. Dorao, "Modeling of bubble column

reactors: Progress and limitations," *Industrial & Engineering Chemistry Research*, vol. 44, no. 14, pp. 5107–5151, 2005.

[62] V. V. Buwa, D. S. Deo, and V. V. Ranade, "Eulerian–Lagrangian simulations of unsteady gas–liquid flows in bubble columns," *International Journal of Multiphase Flow*, vol. 32, pp. 864–885, 7 2006.

[63] E. Delnoij, F. Lammers, J. Kuipers, and W. van Swaaij, "Dynamic simulation of dispersed gas-liquid two-phase flow using a discrete bubble model," *Chemical Engineering Science*, vol. 52, pp. 1429–1458, 5 1997.

[64] S. Laín, D. Bröder, M. Sommerfeld, and M. Göz, "Modelling hydrodynamics and turbulence in a bubble column using the euler–lagrange procedure," *International Journal of Multiphase Flow*, vol. 28, pp. 1381–1407, 8 2002.

[65] M. A. Taborda, M. Sommerfeld, and M. Muniz, "LES-Euler/Lagrange modelling of bubble columns considering mass transfer, chemical reactions and effects of bubble dynamics," *Chemical Engineering Science*, vol. 229, p. 116121, 1 2021.

[66] M. Ishii, "Thermo-fluid dynamic theory of two-phase flow," *NASA STI/Recon Technical Report A*, vol. 75, p. 29657, Jan. 1975.

[67] D. D. McClure, C. Wang, J. M. Kavanagh, D. F. Fletcher, and G. W. Barton, "Experimental investigation into the impact of sparger design on bubble columns at high superficial velocities," *Chemical Engineering Research and Design*, vol. 106, pp. 205–213, 2016.

[68] M. Manninen, V. Taivassalo, and S. Kallio, "On the mixture model for multiphase flow," 1996.

[69] J. Sanyal, S. Vásquez, S. Roy, and M. Dudukovic, "Numerical simulation of gas–liquid dynamics in cylindrical bubble column reactors," *Chemical Engineering Science*, vol. 54, pp. 5071–5083, 11 1999.

[70] G. Tronci, A. Buffo, M. Vanni, and D. Marchisio, "Validation of the diffusion mixture model for the simulation of bubbly flows and implementation in OpenFOAM," *Computers & Fluids*, vol. 227, p. 105026, 9 2021.

[71] C. Hirt and B. Nichols, "Volume of fluid (VOF) method for the dynamics of free boundaries," *Journal of Computational Physics*, vol. 39, pp. 201–225, 1 1981.

[72] A. Tomiyama, I. Zun, A. Sou, and T. Sakaguchi, "Numerical analysis of bubble motion with the VOF method," *Nuclear Engineering and Design*, vol. 141, pp. 69–82, 6 1993.

[73] Z. Yujie, L. Mingyan, X. Yonggui, and T. Can, "Three-dimensional volume of fluid simulations on bubble formation and dynamics in bubble columns," *Chemical Engineering Science*, vol. 73, pp. 55–78, 5 2012.

[74] M. Muniz and M. Sommerfeld, "On the force competition in bubble columns: A numerical study," *International Journal of Multiphase Flow*, vol. 128, 7 2020.

[75] R. B. Bird, W. E. Stewart, and E. N. Lightfoot, *Transport Phenomena*. John Wiley & Sons, 2006.

[76] L. Schiller and A. Naumann, "Über die grundlegenden berechnungen bei der schwerkraftaufbereitung," *Zeitung des Vereins Deutscher Ingenieure*, vol. 77, pp. 318–321, 1933.

[77] J. Grace, N. Th, *et al.*, "Shapes and velocities of single drops and bubbles moving freely through immiscible liquids.," 1976.

[78] R. Clift, J. R. Grace, and M. E. Weber, "Bubbles, drops, and particles," 2005.

[79] M. Ishii and N. Zuber, "Drag coefficient and relative velocity in bubbly, droplet or particulate flows," *AIChE Journal*, vol. 25, pp. 843–855, 9 1979.

[80] A. Tomiyama, "Struggle with computational bubble dynamics," *Multiphase Science and Technology*, vol. 10, 1998.

[81] D. A. Lote, V. Vinod, and A. W. Patwardhan, "Comparison of models for drag and non-drag forces for gas-liquid two-phase bubbly flow," *Multiphase Science and Technology*, vol. 30, pp. 31–76, 2018.

[82] R. Krishna, M. I. Urseanu, J. M. V. Baten, and J. Ellenberger, "Rise velocity of a swarm of large gas bubbles in liquids," *Chemical Engineering Science*, vol. 54, pp. 171–183, 1999.

[83] A. G. Bridge, L. Lapidus, and J. C. Elgin, "The mechanics of vertical gas-liquid fluidized system I: Countercurrent flow," *AIChE Journal*, vol. 10, pp. 819–826, 11 1964.

[84] G. B. Wallis, *One-dimensional two-phase flow*. Courier Dover Publications, 1968.

[85] M. Simonnet, C. Gentric, E. Olmos, and N. Midoux, "Experimental determination of the drag coefficient in a swarm of bubbles," *Chemical Engineering Science*, vol. 62, pp. 858–866, 2007.

[86] I. Roghair, Y. Lau, N. Deen, H. Slagter, M. Baltussen, M. V. S. Annaland, and J. Kuipers, "On the drag force of bubbles in bubble swarms at intermediate and high reynolds numbers," *Chemical Engineering Science*, vol. 66, pp. 3204–3211, 7 2011.

[87] D. D. McClure, J. M. Kavanagh, D. F. Fletcher, and G. W. Barton, "Experimental investigation into the drag volume fraction correction term for gas-liquid bubbly flows," *Chemical Engineering Science*, vol. 170, pp. 91–97, 10 2017.

[88] D. D. Mcclure, J. M. Kavanagh, D. F. Fletcher, and G. W. Barton, "Development of a CFD model of bubble column bioreactors: Part two - comparison of experimental data and CFD predictions," *Chemical Engineering and Technology*, vol. 37, pp. 131–140, 2014.

[89] S. Bove, T. Solberg, and B. H. Hjertager, "Numerical aspects of bubble column simulations," *International Journal of Chemical Reactor Engineering*, vol. 2, 1 2004.

[90] A. Tomiyama, H. Tamai, I. Zun, and S. Hosokawa, "Transverse migration of single bubbles in simple shear flows," *Chemical Engineering Science*, vol. 57, 6 2002.

[91] R. M. Wellek, A. K. Agrawal, and A. H. P. Skelland, "Shape of liquid drops moving in liquid media," *AIChE Journal*, vol. 12, pp. 854–862, 9 1966.

[92] F. Moraga, F. Bonetto, and R. Lahey, "Lateral forces on spheres in turbulent uniform shear flow," *International Journal of Multiphase Flow*, vol. 25, pp. 1321–1372, 9 1999.

[93] D. Legendre and J. Magnaudet, "The lift force on a spherical bubble in a viscous linear shear flow," *Journal of Fluid Mechanics*, vol. 368, pp. 81–126, 8 1998.

[94] B. Ničeno, M. Boucker, and B. L. Smith, "Euler-Euler large eddy simulation of a square cross-sectional bubble column using the neptune CFD code," *Science and Technology of Nuclear Installations*, vol. 2009, pp. 1–8, 2009.

[95] S. Aoyama, K. Hayashi, S. Hosokawa, D. Lucas, and A. Tomiyama, "Lift force acting on single bubbles in linear shear flows," *International Journal of Multiphase Flow*, vol. 96, pp. 113–122, 11 2017.

[96] T. Ziegenhein, A. Tomiyama, and D. Lucas, "A new measuring concept to determine the lift force for distorted bubbles in low morton number system: Results for air/water," *International Journal of Multiphase Flow*, vol. 108, pp. 11–24, 11 2018.

[97] F. Maniscalco, A. Buffo, D. Marchisio, and M. Vanni, "Numerical simulation of bubble columns: LES turbulence model and interphase forces blending approach," *Chemical Engineering Research and Design*, vol. 173, pp. 1–14, 2021.

[98] M. A. Lopez de Bertodano, *Turbulent bubbly two-phase flow in a triangular duct*. PhD thesis, 1992.

[99] M. Dhotre, B. Niceno, and B. Smith, "Large eddy simulation of a bubble column using dynamic sub-grid scale model," *Chemical Engineering Journal*, vol. 136, pp. 337–348, 3 2008.

[100] A. D. Burns, T. Frank, I. Hamill, J.-M. Shi, *et al.*, "The Favre averaged drag model for turbulent dispersion in Eulerian multi-phase flows," in *5th international conference on multiphase flow, ICMF*, vol. 4, pp. 1–17, ICMF, 2004.

[101] S. Antal, R. Lahey, and J. Flaherty, "Analysis of phase distribution in fully developed laminar bubbly two-phase flow," *International Journal of Multiphase Flow*, vol. 17, pp. 635–652, 9 1991.

[102] T. Frank, P. Zwart, E. Krepper, H.-M. Prasser, and D. Lucas, "Validation of CFD models for mono- and polydisperse air–water two-phase flows in pipes," *Nuclear Engineering and Design*, vol. 238, pp. 647–659, 3 2008.

[103] S. Hosokawa, A. Tomiyama, S. Misaki, and T. Hamada, "Lateral migration of single bubbles due to the presence of wall," pp. 855–860, ASMEDC, 1 2002.

[104] F. Maniscalco, A. Raponi, M. Vanni, and A. Buffo, "Computational modeling of the impact of solid particles on the gas hold-up in slurry bubble columns," *Chemical Engineering Transactions*, vol. 86, pp. 1141–1146, 2021.

[105] R. F. Mudde and O. Simonin, "Two- and three-dimensional simulations of a bubble plume using a two-fluid model," *Chemical Engineering Science*, vol. 54, 11 1999.

[106] ANSYS, Inc, Canonsburg, PA, *ANSYS Fluent Theory Guide 2019R3*, 2019.

[107] T. Hibiki and M. Ishii, "Two-group interfacial area transport equations at bubbly-to-slug flow transition," *Nuclear Engineering and Design*, vol. 202, pp. 39–76, 11 2000.

[108] S. B. Pope and S. B. Pope, *Turbulent flows*. Cambridge university press, 2000.

[109] A. N. Kolmogorov, "The local structure of turbulence in incompressible viscous fluid for very large Reynolds numbers," *Cr Acad. Sci. URSS*, vol. 30, pp. 301–305, 1941.

[110] C. Santarelli and J. Fröhlich, "Direct numerical simulations of spherical bubbles in vertical turbulent channel flow. influence of bubble size and bidispersity," *International Journal of Multiphase Flow*, vol. 81, pp. 27–45, 5 2016.

[111] T. Ma, C. Santarelli, T. Ziegenhein, D. Lucas, and J. Fröhlich, "Direct numerical simulation–based reynolds-averaged closure for bubble-induced turbulence," *Physical Review Fluids*, vol. 2, 3 2017.

[112] S. Erdogan, T. Schulenberg, O. Deutschmann, and M. Wörner, "Evaluation of models for bubble-induced turbulence by DNS and utilization in two-fluid model computations of an industrial pilot-scale bubble column," *Chemical Engineering Research and Design*, vol. 175, pp. 283–295, 11 2021.

[113] A. Buffo and D. L. Marchisio, "Modeling and simulation of turbulent polydisperse gas-liquid systems via the generalized population balance equation," *Reviews in Chemical Engineering*, vol. 30, 1 2014.

[114] Z. Khan, V. H. Bhusare, and J. B. Joshi, "Comparison of turbulence models for bubble column reactors," *Chemical Engineering Science*, vol. 164, pp. 34–52, 2017.

[115] B. E. Launder, D. B. Spalding, *et al.*, "Lectures in mathematical models of turbulence," 1972.

[116] V. Yakhot and S. A. Orszag, "Renormalization group analysis of turbulence. I. Basic theory," *Journal of scientific computing*, vol. 1, no. 1, pp. 3–51, 1986.

[117] T.-H. Shih, W. W. Liou, A. Shabbir, Z. Yang, and J. Zhu, "A new k-ϵ eddy viscosity model for high reynolds number turbulent flows," *Computers & Fluids*, vol. 24, pp. 227–238, 3 1995.

[118] D. Pfleger, S. Gomes, N. Gilbert, and H.-G. Wagner, "Hydrodynamic simulations of laboratory scale bubble columns fundamental studies of the Eulerian–Eulerian modelling approach," *Chemical Engineering Science*, vol. 54, pp. 5091–5099, 11 1999.

[119] K. Ekambara, M. T. Dhotre, and J. B. Joshi, "CFD simulations of bubble column reactors: 1D, 2D and 3D approach," *Chemical Engineering Science*, vol. 60, pp. 6733–6746, 2005.

[120] D. C. Wilcox *et al.*, *Turbulence modeling for CFD*, vol. 3. DCW industries La Canada, CA, 2006.

[121] F. Menter, "Zonal two equation k-ω turbulence models for aerodynamic flows," in *23rd Fluid Dynamics, Plasmadynamics, and Lasers Conference*, American Institute of Aeronautics and Astronautics, 7 1993.

[122] K. Bech, "Dynamic simulation of a 2D bubble column," *Chemical Engineering Science*, vol. 60, pp. 5294–5304, 9 2005.

[123] P. Sagaut, *Large eddy simulation for incompressible flows: an introduction*. Springer Science & Business Media, 2006.

[124] R. A. Clark, J. H. Ferziger, and W. C. Reynolds, "Evaluation of subgrid-scale models using an accurately simulated turbulent flow," *Journal of fluid mechanics*, vol. 91, no. 1, pp. 1–16, 1979.

[125] A. Leonard, "Energy cascade in large-eddy simulations of turbulent fluid flows," in *Advances in geophysics*, vol. 18, pp. 237–248, Elsevier, 1975.

[126] N. Mansour, P. Moin, W. Reynolds, and J. Ferziger, "Improved methods for large eddy simulations of turbulence," in *Turbulent shear flows I*, pp. 386–401, Springer, 1979.

[127] M. Klein, S. Ketterl, and J. Hasslberger, "Large eddy simulation of multiphase flows using the volume of fluid method: Part 1—governing equations and a priori analysis," *Experimental and Computational Multiphase Flow*, vol. 1, no. 2, pp. 130–144, 2019.

[128] S. Liu, C. Meneveau, and J. Katz, "On the properties of similarity subgrid-scale models as deduced from measurements in a turbulent jet," *Journal of Fluid Mechanics*, vol. 275, pp. 83–119, 1994.

[129] J. Smagorinsky, "General circulation experiments with the primitive equations: I. the basic experiment," *Monthly weather review*, vol. 91, no. 3, pp. 99–164, 1963.

[130] J. Deardorff, "On the magnitude of the subgrid scale eddy coefficient," *Journal of Computational Physics*, vol. 7, no. 1, pp. 120–133, 1971.

[131] M. Tutar and A. Holdø, "Computational modelling of flow around a circular cylinder in sub-critical flow regime with various turbulence models," *International journal for numerical methods in fluids*, vol. 35, no. 7, pp. 763–784, 2001.

[132] S. Rodriguez, *Applied computational fluid dynamics and turbulence modeling*. Springer, 2019.

[133] M. Germano, U. Piomelli, P. Moin, and W. H. Cabot, "A dynamic subgrid-scale eddy viscosity model," *Physics of Fluids A: Fluid Dynamics*, vol. 3, no. 7, pp. 1760–1765, 1991.

[134] Y. Sato and K. Sekoguchi, "Liquid velocity distribution in two-phase bubble flow," *International Journal of Multiphase Flow*, vol. 2, pp. 79–95, 6 1975.

[135] B. Ničeno, M. Dhotre, and N. Deen, "One-equation sub-grid scale (SGS) modelling for euler–euler large eddy simulation (EELES) of dispersed bubbly flow," *Chemical Engineering Science*, vol. 63, pp. 3923–3931, 8 2008.

[136] S. Zhu, A. Ooi, R. Manasseh, and A. Skvortsov, "Prediction of gas holdup in partially aerated bubble columns using an EE-LES coupled model," *Chemical Engineering Science*, vol. 217, p. 115492, 2020.

[137] S. B. Pope, "Ten questions concerning the large-eddy simulation of turbulent flows," *New journal of Physics*, vol. 6, no. 1, p. 35, 2004.

[138] M. Milelli, B. Smith, and D. Lakehal, "Large-eddy simulation of turbulent shear flows laden with bubbles," in *Direct and Large-Eddy Simulation IV*, pp. 461–470, Springer, 2001.

[139] Y. Sato, M. Sadatomi, and K. Sekoguchi, "Momentum and heat transfer in two-phase bubble flow—I. Theory," *International Journal of Multiphase Flow*, vol. 7, no. 2, pp. 167–177, 1981.

[140] M. Lance and J. Bataille, "Turbulence in the liquid phase of a uniform bubbly air–water flow," *Journal of Fluid Mechanics*, vol. 222, p. 95–118, 1991.

[141] I. Kataoka and A. Serizawa, "Turbulence characteristics and their application to multi-dimensional analysis of two-phase flow," in *Eighth international topical meeting on nuclear reactor thermal-hydraulics*, 1997.

[142] R. Rzehak and E. Krepper, "Bubble-induced turbulence: Comparison of CFD models," *Nuclear Engineering and Design*, vol. 258, pp. 57–65, 5 2013.

[143] C. Morel, "Turbulence modelling and first numerical simulations in turbulent two-phase flows," in *Proc. 11th Symp. on Turbulent Shear Flows, Grenoble, France, 1997*, vol. 3, 1997.

[144] A. Troshko and Y. Hassan, "A two-equation turbulence model of turbulent bubbly flows," *International Journal of Multiphase Flow*, vol. 27, no. 11, pp. 1965–2000, 2001.

[145] M. Politano, P. Carrica, and J. Converti, "A model for turbulent polydisperse two-phase flow in vertical channels," *International Journal of Multiphase Flow*, vol. 29, no. 7, pp. 1153–1182, 2003.

[146] T. Wang and J. Wang, "Numerical simulations of gas–liquid mass transfer in bubble columns with a CFD–PBM coupled model," *Chemical Engineering Science*, vol. 62, pp. 7107–7118, 12 2007.

[147] D. L. Marchisio and R. O. Fox, *Computational models for polydisperse particulate and multiphase systems*. Cambridge University Press, 2013.

[148] M. Petitti, A. Nasuti, D. L. Marchisio, M. Vanni, G. Baldi, N. Mancini, and F. Podenzani, "Bubble size distribution modeling in stirred gas-liquid reactors with QMOM augmented by a new correction algorithm," *AIChE Journal*, vol. 56, pp. 36–53, 1 2010.

[149] Y. Liao and D. Lucas, "A literature review of theoretical models for drop and bubble breakup in turbulent dispersions," *Chemical Engineering Science*, vol. 64, pp. 3389–3406, 2009.

[150] S. Falzone, A. Buffo, M. Vanni, and D. L. Marchisio, "Chapter three - simulation of turbulent coalescence and breakage of bubbles and droplets in the presence of surfactants, salts, and contaminants," in *Bridging Scales in Modelling and Simulation of Non-Reacting and Reacting Flows. Part I* (A. Parente and J. De Wilde, eds.), vol. 52 of *Advances in Chemical Engineering*, pp. 125–188, Academic Press, 2018.

[151] C. Coulaloglou and L. Tavlarides, "Description of interaction processes in agitated liquid-liquid dispersions," *Chemical Engineering Science*, vol. 32, 1977.

[152] J. C. Lasheras, C. Eastwood, C. Martınez-Bazán, and J. Montanes, "A review of statistical models for the break-up of an immiscible fluid immersed into a fully developed turbulent flow," *International Journal of multiphase flow*, vol. 28, no. 2, pp. 247–278, 2002.

[153] G. Narsimhan, J. Gupta, and D. Ramkrishna, "A model for transitional breakage probability of droplets in agitated lean liquid-liquid dispersions," *Chemical Engineering Science*, vol. 34, no. 2, pp. 257–265, 1979.

[154] V. Alopaeus, J. Koskinen, K. I. Keskinen, and J. Majander, "Simulation of the population balances for liquid–liquid systems in a nonideal stirred tank. part 2—parameter fitting and the use of the multiblock model for dense dispersions," *Chemical Engineering Science*, vol. 57, no. 10, pp. 1815–1825, 2002.

[155] M. Laakkonen, V. Alopaeus, and J. Aittamaa, "Validation of bubble breakage, coalescence and mass transfer models for gas–liquid dispersion in agitated vessel," *Chemical Engineering Science*, vol. 61, 1 2006.

[156] M. J. Prince and H. W. Blanch, "Bubble coalescence and break-up in air-sparged bubble columns," *AIChE journal*, vol. 36, no. 10, pp. 1485–1499, 1990.

[157] H. Luo and H. F. Svendsen, "Theoretical model for drop and bubble breakup in turbulent dispersions," *AIChE Journal*, vol. 42, no. 5, pp. 1225–1233, 1996.

[158] F. Lehr, M. Millies, and D. Mewes, "Bubble-size distributions and flow fields in bubble columns," *AIChE Journal*, vol. 48, no. 11, pp. 2426–2443, 2002.

[159] C. Martínez-Bazán, J. Montanes, and J. C. Lasheras, "On the breakup of an air bubble injected into a fully developed turbulent flow. Part 2. Size pdf of the resulting daughter bubbles," *Journal of Fluid Mechanics*, vol. 401, pp. 183–207, 1999.

[160] C. Tsouris and L. Tavlarides, "Breakage and coalescence models for drops in turbulent dispersions," *AIChE Journal*, vol. 40, no. 3, pp. 395–406, 1994.

[161] M. Laakkonen, P. Moilanen, V. Alopaeus, and J. Aittamaa, "Modelling local bubble size distributions in agitated vessels," *Chemical Engineering Science*,

vol. 62, no. 3, pp. 721–740, 2007.

[162] Y. Liao and D. Lucas, "A literature review on mechanisms and models for the coalescence process of fluid particles," *Chemical Engineering Science*, vol. 65, pp. 2851–2864, 2010.

[163] Q. Wu, S. Kim, M. Ishii, and S. Beus, "One-group interfacial area transport in vertical bubbly flow," *International Journal of Heat and Mass Transfer*, vol. 41, no. 8-9, pp. 1103–1112, 1998.

[164] T. Wang, J. Wang, and Y. Jin, "Population balance model for gas-liquid flows: Influence of bubble coalescence and breakup models," *Industrial & Engineering Chemistry Research*, vol. 44, no. 19, pp. 7540–7549, 2005.

[165] T. Wang, J. Wang, and Y. Jin, "Theoretical prediction of flow regime transition in bubble columns by the population balance model," *Chemical Engineering Science*, vol. 60, no. 22, pp. 6199–6209, 2005.

[166] S. K. Friedlander, "Smoke, dust and haze: Fundamentals of aerosol behavior," *New York*, 1977.

[167] Y. Liao, R. Rzehak, D. Lucas, and E. Krepper, "Baseline closure model for dispersed bubbly flow: Bubble coalescence and breakup," *Chemical Engineering Science*, vol. 122, pp. 336–349, 2015.

[168] J. F. Walter and H. W. Blanch, "Liquid circulation patterns and their effect on gas hold-up and axial mixing in bubble columns," *Chemical Engineering Communications*, vol. 19, no. 4-6, pp. 243–262, 1983.

[169] H. Sovová, "Breakage and coalescence of drops in a batch stirred vessel—II comparison of model and experiments," *Chemical Engineering Science*, vol. 36, 1981.

[170] M. Vanni, "Approximate population balance equations for aggregation–breakage processes," *Journal of Colloid and Interface Science*, vol. 221, no. 2, pp. 143–160, 2000.

[171] E. Krepper, D. Lucas, T. Frank, H.-M. Prasser, and P. J. Zwart, "The inhomogeneous MUSIG model for the simulation of polydispersed flows," *Nuclear Engineering and Design*, vol. 238, no. 7, pp. 1690–1702, 2008.

[172] R. McGraw, "Description of aerosol dynamics by the quadrature method of moments," *Aerosol Science and Technology*, vol. 27, no. 2, pp. 255–265, 1997.

[173] D. L. Marchisio, R. D. Vigil, and R. O. Fox, "Implementation of the quadrature method of moments in CFD codes for aggregation–breakage problems," *Chemical Engineering Science*, vol. 58, 8 2003.

[174] J. Gimbun, C. D. Rielly, and Z. K. Nagy, "Modelling of mass transfer in gas-liquid stirred tanks agitated by Rushton turbine and CD-6 impeller: A scale-up study," *Chemical Engineering Research and Design*, vol. 87, pp. 437–451, 2009.

[175] C. B. Vik, J. Solsvik, M. Hillestad, and H. A. Jakobsen, "Interfacial mass transfer limitations of the Fischer-Tropsch synthesis operated in a slurry bubble column reactor at industrial conditions," *Chemical Engineering Science*,

vol. 192, pp. 1138–1156, 2018.

[176] W. K. Lewis and W. G. Whitman, "Principles of gas absorption.," *Industrial & Engineering Chemistry*, vol. 16, no. 12, pp. 1215–1220, 1924.

[177] R. Higbie, "The rate of absorption of a pure gas into a still liquid during short periods of exposure," *Trans. AIChE*, vol. 31, pp. 365–389, 1935.

[178] P. V. Danckwerts, "Significance of liquid-film coefficients in gas absorption," *Industrial & Engineering Chemistry*, vol. 43, 6 1951.

[179] J. C. Lamont and D. S. Scott, "An eddy cell model of mass transfer into the surface of a turbulent liquid," *AIChE Journal*, vol. 16, pp. 513–519, 1970.

[180] L.-S. Fan, A. Matsuura, and S.-H. Chern, "Hydrodynamic characteristics of a gas-liquid-solid fluidized bed containing a binary mixture of particles," *AIChE journal*, vol. 31, no. 11, pp. 1801–1810, 1985.

[181] J. Deswart and R. Krishna, "Influence of particles concentration on the hydrodynamics of bubble-column slurry reactors," *Chemical engineering research & design*, vol. 73, no. 3, pp. 308–313, 1995.

[182] R. Krishna, J. M. V. Baten, M. I. Urseanu, and J. Ellenberger, "Design and scale up of a bubble column slurry reactor for Fischer- Tropsch synthesis," *Chemical Engineering Science*, vol. 56, pp. 537–545, 2001.

[183] B. Gandhi, A. Prakash, and M. A. Bergougnou, "Hydrodynamic behavior of slurry bubble column at high solids concentrations," *Powder Technology*, 1999.

[184] S. Saxena, N. Rao, and P. Thimmapuram, "Gas phase holdup in slurry bubble columns for two- and three-phase systems," *The Chemical Engineering Journal*, vol. 49, pp. 151–159, 9 1992.

[185] D. B. Bukur, S. A. Patel, and J. G. Daly, "Gas holdup and solids dispersion in a three-phase slurry bubble column," *AIChE Journal*, vol. 36, no. 11, 1990.

[186] J. H. Kluytmans, B. G. van Wachem, B. F. Kuster, and J. C. Schouten, "Gas holdup in a slurry bubble column: influence of electrolyte and carbon particles," *Industrial & Engineering Chemistry Research*, vol. 40, no. 23, pp. 5326–5333, 2001.

[187] M. V. der Zon, P. J. Hammersma, E. K. Poels, and A. Bliek, "Coalescence of freely moving bubbles in water by the action of suspended hydrophobic particles," *Chemical Engineering Science*, 2002.

[188] S. Rabha, M. Schubert, M. Wagner, D. Lucas, and U. Hampel, "Bubble size and radial gas hold-up distributions in a slurry bubble column using ultrafast electron beam x-ray tomography," *AIChE journal*, vol. 59, no. 5, pp. 1709–1722, 2013.

[189] K. C. Ruthiya, B. F. Kuster, and J. C. Schouten, "Gas-liquid mass transfer enhancement in a surface aeration stirred slurry reactors," *The Canadian Journal of Chemical Engineering*, vol. 81, no. 3-4, pp. 632–639, 2003.

[190] E. Alper, B. Wichtendahl, and W.-D. Deckwer, "Gas absorption mechanism in catalytic slurry reactors," *Chemical Engineering Science*, vol. 35, no. 1-2,

pp. 217–222, 1980.

[191] S. Orvalho, M. Hashida, M. Zednikova, P. Stanovsky, M. C. Ruzicka, S. Sasaki, and A. Tomiyama, "Flow regimes in slurry bubble column: Effect of column height and particle concentration," *Chemical Engineering Journal*, vol. 351, pp. 799–815, 2018.

[192] A. Mühlbauer, M. W. Hlawitschka, and H. Bart, "Models for the numerical simulation of bubble columns: A review," *Chemie Ingenieur Technik*, vol. 91, pp. 1747–1765, 12 2019.

[193] A. A. Troshko and F. Zdravistch, "CFD modeling of slurry bubble column reactors for Fisher–Tropsch synthesis," *Chemical Engineering Science*, vol. 64, pp. 892–903, 3 2009.

[194] S. Rabha, M. Schubert, and U. Hampel, "Intrinsic flow behavior in a slurry bubble column: A study on the effect of particle size," *Chemical Engineering Science*, vol. 93, pp. 401–411, 2013.

[195] R. Zhou, N. Yang, and J. Li, "CFD simulation of gas-liquid-solid flow in slurry bubble columns with EMMS drag model," *Powder Technology*, vol. 314, pp. 466–479, 2017.

[196] K. Tsuchiya, A. Furumoto, L.-S. Fan, and J. Zhang, "Suspension viscosity and bubble rise velocity in liquid-solid fluidized beds," *Chemical Engineering Science*, vol. 52, pp. 3053–3066, 9 1997.

[197] V. Vand, "Viscosity of solutions and suspensions. I. Theory," *The Journal of Physical Chemistry*, vol. 52, no. 2, pp. 277–299, 1948.

[198] D. G. Thomas, "Transport characteristics of suspension: VIII. A note on the viscosity of newtonian suspensions of uniform spherical particles," *Journal of colloid science*, vol. 20, no. 3, pp. 267–277, 1965.

[199] S. Saxena and Z. Chen, "Hydrodynamics and heat transfer of baffled and unbaffled slurry bubble columns," *Reviews in Chemical Engineering*, vol. 10, no. 3-4, pp. 193–400, 1994.

[200] L. Xu, Z. Xia, X. Guo, and C. Chen, "Application of population balance model in the simulation of slurry bubble column," *Industrial and Engineering Chemistry Research*, vol. 53, pp. 4922–4930, 2014.

[201] K. D. Squires and J. K. Eaton, "Effect of selective modification of turbulence on two-equation models for particle-laden turbulent flows," *Journal of Fluids Engineering*, vol. 116, pp. 778–784, 12 1994.

[202] S. Kouzbour, B. Gourich, Y. Stiriba, C. Vial, F. Gros, and R. Sotudeh-Gharebagh, "Experimental analysis of the effects of liquid phase surface tension on the hydrodynamics and mass transfer in a square bubble column," *International Journal of Heat and Mass Transfer*, vol. 170, p. 121009, 2021.

[203] S. Kouzbour, F. Maniscalco, A. Buffo, M. V. F. X. Grau, G. Bouchaib, and Y. Stiriba, "Effects of sds surface-active agents on hydrodynamics and oxygen mass transfer in a square bubble column reactor: Experimental and CFD modeling study," *Chemical Engineering Science*, (to be submitted).

[204] P. M. Raimundo, *Analysis and modelization of local hydrodynamics in bubble columns*. Phd thesis, Université Grenoble Alpes, Oct. 2015.

[205] B. van Leer, "Towards the ultimate conservative difference scheme. II. monotonicity and conservation combined in a second-order scheme," *Journal of Computational Physics*, vol. 14, no. 4, pp. 361–370, 1974.

[206] J. Crank and P. Nicolson, "A practical method for numerical evaluation of solutions of partial differential equations of the heat-conduction type," *Mathematical Proceedings of the Cambridge Philosophical Society*, vol. 43, no. 1, p. 50–67, 1947.

[207] L. Gemello, *Modelling of the hydrodynamics of bubble columns using a two-fluid model coupled with a population balance approach*. PhD thesis, Politecnico di Torino, Nov. 2018.

[208] G. Hu and I. Celik, "Eulerian–Lagrangian based large-eddy simulation of a partially aerated flat bubble column," *Chemical Engineering Science*, vol. 63, no. 1, pp. 253–271, 2008.

[209] D. Darmana, N. Deen, J. Kuipers, W. Harteveld, and R. Mudde, "Numerical study of homogeneous bubbly flow: Influence of the inlet conditions to the hydrodynamic behavior," *International Journal of Multiphase Flow*, vol. 35, no. 12, pp. 1077–1099, 2009.

[210] T. Ma, T. Ziegenhein, D. Lucas, E. Krepper, and J. Fröhlich, "Euler–Euler large eddy simulations for dispersed turbulent bubbly flows," *International Journal of Heat and Fluid Flow*, vol. 56, pp. 51–59, 2015.

[211] D. B. Spalding, "A novel finite difference formulation for differential expressions involving both first and second derivatives," *International Journal for Numerical Methods in Engineering*, vol. 4, no. 4, pp. 551–559, 1972.

[212] B. Magolan, N. Lubchenko, and E. Baglietto, "A quantitative and generalized assessment of bubble-induced turbulence models for gas-liquid systems," *Chemical Engineering Science: X*, vol. 2, p. 100009, 2019.

[213] G. Montoya, D. Lucas, E. Baglietto, and Y. Liao, "A review on mechanisms and models for the churn-turbulent flow regime," *Chemical Engineering Science*, vol. 141, pp. 86–103, 2016.

[214] I. G. Reilly, D. S. Scott, T. De Bruijn, A. Jain, and J. Piskorz, "A correlation for gas holdup in turbulent coalescing bubble columns," *The Canadian Journal of Chemical Engineering*, vol. 64, no. 5, pp. 705–717, 1986.

[215] E. Askari, P. Proulx, and A. Passalacqua, "Modelling of bubbly flow using CFD-PBM solver in OpenFOAM: Study of local population balance models and extended quadrature method of moments applications," *ChemEngineering*, vol. 2, no. 1, 2018.

[216] G. Hebrard, J. Zeng, and K. Loubiere, "Effect of surfactants on liquid side mass transfer coefficients: a new insight," *Chemical Engineering Journal*, vol. 148, no. 1, pp. 132–138, 2009.

This Ph.D. thesis has been typeset by means of the TEX-system facilities. The typesetting engine was pdfLATEX. The document class was `toptesi`, by Claudio Beccari, with option `tipotesi=scudo`. This class is available in every up-to-date and complete TEX-system installation.